Mass Selected Metal and Metal Oxide Clusters as Catalysts

by

Xin Tang

A dissertation submitted to Johns Hopkins University in conformity with the requirements
for the degree of Doctor of Philosophy

Baltimore, Maryland

November, 2016

Abstract

Transition metal and metal oxide nanoparticles/clusters are widely used as catalysts in heterogeneous catalysis. However, the structure sensitivity of the catalysts is still unclear due to the structural complexities of the nano-catalysts. The studies presented in this thesis have used soft-landed mass-selected clusters as model systems for heterogeneous catalysis, which aims to achieve a microscopic level of understanding of the catalytic processes. Therefore, the surface structures of size selected metal oxide, sulfide and oxynitride clusters were studied by scanning tunneling microscope and atomic force microscope. Based on their size, chemical compositions, cluster flux intensity and the substrate temperature, the deposited clusters exhibited various surface morphologies as a result of different cluster-cluster and cluster-surface interactions. In addition, the catalytic properties of mass selected metal oxides were studied by temperature programmed desorption and x-ray photoelectron spectroscopy. It is found that the cluster size, the supporting substrates and the chemical compositions of the clusters played an important role in determining the catalytic activities of the metal oxide clusters.

Acknowledgments

This thesis would not have been possible without the help from so many people over the last six years. It has been a great journey for me to be in the Bowen group and together to explore the emerging field at the interface between cluster science and surface science.

I would like to express my deepest gratitude to my Ph.D. advisor, Prof. Kit H. Bowen, who is not only an admirable scientist, but also a great mentor providing consistent support for his students. His enthusiasm for science and his encouragement have always been my driving force during my Ph.D..

I am very grateful to the help from Prof. Howard Fairbrother, Prof. Kai Wu and Prof. Ueli Heiz. As an expert in surface science, Prof. Fairbrother has taught me many “secret recipes” in surface science, all of which have been tremendously helpful. My undergraduate advisor, Prof. Wu brought me to the field of surface science. Prof. Heiz, as an expert in cluster science, has generously helped us to build our cluster catalysis instrument.

I also would like to convey my gratitude to my colleagues inside the Bowen Group. Shawn Li, along with Kevin, first introduced me to the cluster lab when I was wondering around the stairway. Their friendship, advice and support have really been a great help for me. As senior students, Jing, Colin, Allyson and Jacob are always a great source of help in almost every aspect. My thanks also go to Evan, Zach, Sara, Linjie and all the visiting students from Germany for their support during my six years in the Bowen Lab.

Last but not the least, I want to express my sincere appreciation to my parents for their continuous support and consistent encouragement.

TABLE OF CONTENTS

List of Tables

List of Figures

1. Introduction

The demand for improving the selectivity and activity of industrial heterogeneous catalysis requires identifying the active sites of the desired pathways in the catalytic processes and maximizing the population of specific active sites.[2] Nanoparticles, widely used in industrial heterogeneous catalysis, are free standing or supported clusters, which are ensembles of a few tens to several thousand atoms. Although the size of nanoparticles can vary between the order of a few nanometers to several tens or hundreds of nanometers, the most active ones in heterogeneous catalysis are only up to a few nanometers in diameter, indicating that the active sites in catalysts are highly populated. [3]

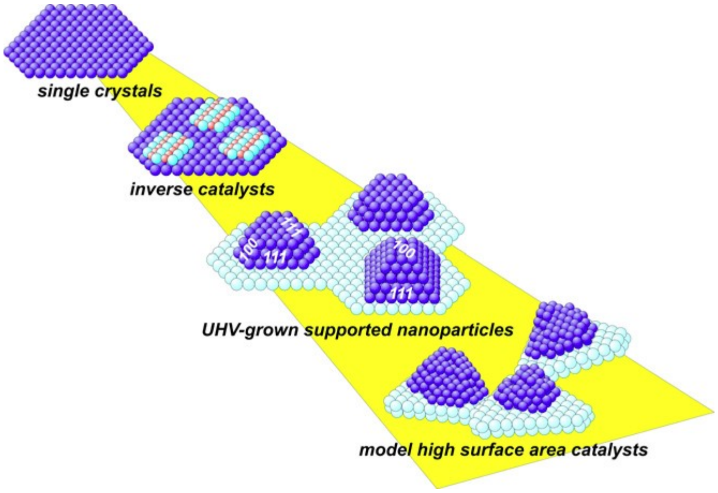

Figure 1.1 Model systems for catalysis[1]

Supported soft-landed size-selected clusters are natural model systems for heterogeneous catalysis. Compared to the nanoparticles synthesized by the solution or sol-gel method, supported soft-landed size-selected clusters are free of stabilizers such as ligands and surfactants that could possibly complicate or even block the active sites. Size-selected clusters have a remarkable size dependent structural diversity and properties; their preparation protocol enables the precise control of size, structure and chemical constitution. Additionally, the relatively small scale of atoms in size-selected clusters also allows high-level quantum calculations to be applied to elucidate their structure with the presence of the underlying supports. Along with this, determining the critical reactive sites/steps and the simultaneous electronic properties will also be possible. [4]

The preparation of size-selected clusters on surfaces has greatly benefited from the development of cluster science over the last few decades. With new designs of high intensity ion sources as well as high ion transmission systems, size-selected clusters can be deposited on the surface with relatively high intensity to meet the requirements for catalytic studies. Depending on the kinetic energy of the clusters as they interact with the surface, the deposition can be either energetically pinning or soft landing. The latter one is more intriguing to catalytic studies because it enables the clusters to maintain their gas phase essentials, while pinning will cause the deformation or the fragmentation of the nascent gas phase clusters.

The catalytic properties of soft-landed size-selected clusters, in particular precious metal clusters, have been studied by many groups (Table 1.1). Among all the catalytic reactions, CO oxidation reactions have been studied extensively due to their importance as a model system in heterogeneous catalysis. For instance, Ueli Heiz's group has studied the CO oxidation on size-selected Au_n cluster supported on magnesia.[5] The reactivity has been found to be strongly dependent on the size of the clusters: $Au_{2\sim7}$ are relatively inactive, while Au_8 starts to show a dramatic increase of catalytic activity (see Figure 1.2). In addition to the size dependent effect, an unexpected support dependency is also observed. The Au_8 clusters on defect-rich MgO(001) substrate are much more catalytically active than the same clusters on defect-poor substrates, which is attributed to the charging effect of Au_8 clusters on F-center defects of magnesia[6](see Figure 1.3). The importance of the support for clusters has also been stressed in another study by Wolfgang Harbich's group, where the strong-metal-support-interaction (SMSI) and oxygen spillover to the substrate play important roles[7]. In addition to CO oxidation reactions, there are various studies reported on other catalytic systems for size-selected clusters, including the acetylene cyclotrimerization reaction into benzene[8], the reaction $CO + NO \rightarrow CO_2 + ½N_2$[9], the oxidative dehydrogenation of propane to propylene[10], and the dehydrogenation of cyclohexene[11].

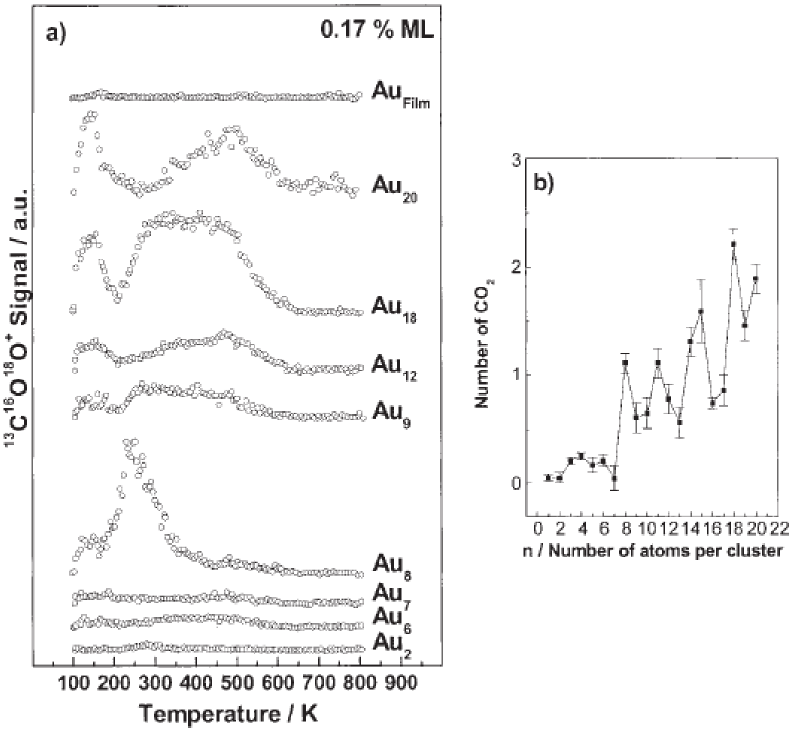

Figure 1.2 Size Dependent Catalytic Activity for CO oxidation reaction on Au_n/MgO[5]

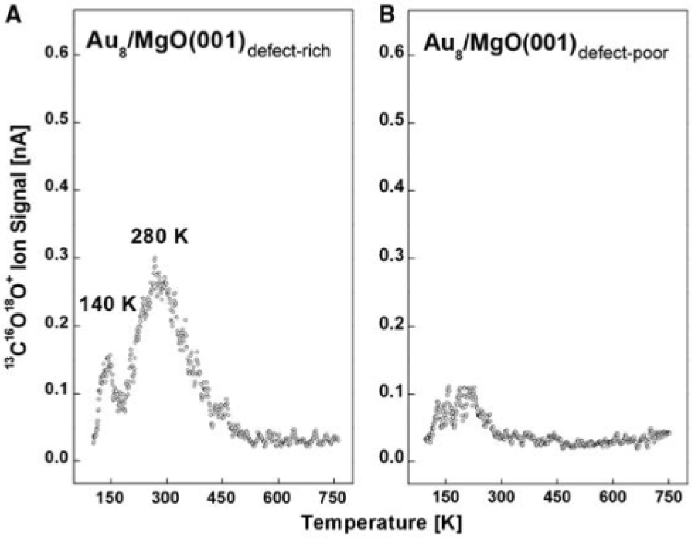

Figure 1.3 CO Oxidation Activity of Au_8 clusters on (A)defect-rich (B)defect-poor MgO(001)[6]

Table 1.1 Known Mass Selected Cluster Catalysts

PI	Catalyst	Chemical Reaction	Size regime
Anderson	Pd_n/Al_2O_3[12,13]	CO oxidation	$n \leq 30$
	$Pd_n/Al_2O_3/Re(0001)$[14]	CO oxidation	n=20
	Pt_n on GCE[15]	Oxygen reduction reaction	$n \leq 11$
	$Pt_n/Al_2O_3/Re(0001)$[16]	Oxygen activation and CO oxidation	n=1, 2, 4, 7, 10, 14, 18
	Pt_n/indium tin oxide[14]	Ethanol electro-oxidation	n=1-14
	Pt_n/indium tin oxide[17]	Oxygen reduction reaction	n>10
	$Pd_n/TiO_2(110)$[18,19]	CO oxidation	n = 4, 7, 10, 20

	$Au_n/TiO_2(110)$[20]	CO oxidation	$n = 1\text{-}7$
	$Ir_n/SiO_2/Si(100)$[21]	CO oxidation	$n = 1, 2, 10$
	$Ir_n/Al_2O_3/NiAl(110)$[22]	Hydrazine decomposition	$n < 15$
Vajda	Au_n[10]	Propene epoxidation	$n = 6\text{-}10$
	Co_n on Al_2O_3, ZnO and TiO_2 and MgO[11]	Oxidative dehydrogenation of cyclohexene	$n = 27 \pm 4$
	Co_n/Al_2O_3[23]	Fischer-Tropsch synthesis	$n=4, 27$
	Pd_n on amorphous alumina[24]	Oxidative decomposition of methanol	$n = 8\text{-}12, 15\text{-}18$
	Pd_n[25]	Water oxidation electrocatalysis	$n=4, 6, 17$
	Pd_n/graphite[26]	Cyclohexene oxidation	$n=10\text{-}120$
	Ag_n^{+}[27]	Direct propylene epoxidation	$n = 2 - 4$
	Pt_n[28]	Oxidative dehydrogenation of propane	$n = 8\text{-}10$

	Cu_n/Al_2O_3[29]	Carbon dioxide conversion to methanol	n=4
Heiz	Pd_n/MgO[30]	Cyclotrimerization of acetylene to benzene	n = 1-30
	Pt_n[31]	CO oxidation	n = 8 - 20
	Pt_{46}[32]	O_2 reduction	n=46
	Pt_n/CdS nanorods[33]	Photocatalytic Hydrogen Evolution Reaction	n=8, 22, 46, 68
	Pt_n/MgO[34]	Ethylene hydrogenation	n=8-15
	Au_n, Pt_n, Pd_n, Rh_n supported on MgO(100) films[35]	CO oxidation	n = 1-20
	Au_n/TiO_2[36]	CO oxidation	n=6, 7
	Pd_n/MgO(100)[9]	$CO+NO\rightarrow CO_2+ \frac{1}{2} N_2$	$n \leq 30$
	$Pd_{13}O_x/MgO$[37]	CO oxidation	n=13
	Pd_{30}/MgO[38]	CO oxidation	n=30

	Mo_n, Ni_n, Cu_n, Rh_n, Pd_n, Ag_n, Pt_n,or Au_n on MgO(100)[39]	Acetylene polymerization	$n < 50$
Harbich	Pt_n/TiO_2[7]	CO oxidation	$n = 1$
	Pt_n/TiO_2[40]		$n = 7$
	Pt_n/TiO_2[41]		$n=3, 7, 10$
Buratto	Au_n/TiO_2[42]	No CO oxidation data	
	VO_x/ TiO_2	Oxidation of Methanol to Formaldehyde[43]	$x=0, 1, 2$
	Ag_n/TiO_2[44]	No CO oxidation data	
Palmer	Pd_n/Graphite[45]	Hydrogenation of 1-pentyne	$n=55,120,200,300,400$
	Au_n/amorphous carbon support[46]	CO oxidation	$n=561, 932, 2057$
Other	Pt_n/TiO_2[47,48]	CO oxidation	$n = 4, 7\text{-}10, 15$
White	Niobium oxide/Cu(111)[49]	Water dissociation	Nb_3O_5, Nb_3O_7, Nb_4O_7, and Nb_4O_{10}

In contrast to the extensive studies on precious metal clusters, our knowledge of the size-selected metal oxides, sulfides, nitrides, carbides and alloys is extremely limited despite their importance in catalysis and material science. For example, almost one quarter of the production of the top 20 chemicals depends on selective oxidation catalyzed by metal oxides[50]. Metal oxides have been widely used as redox, acid and base catalysts for many reactions as summarized in Table 1.2.

Table 1.2 Properties of Metal Oxides[51]

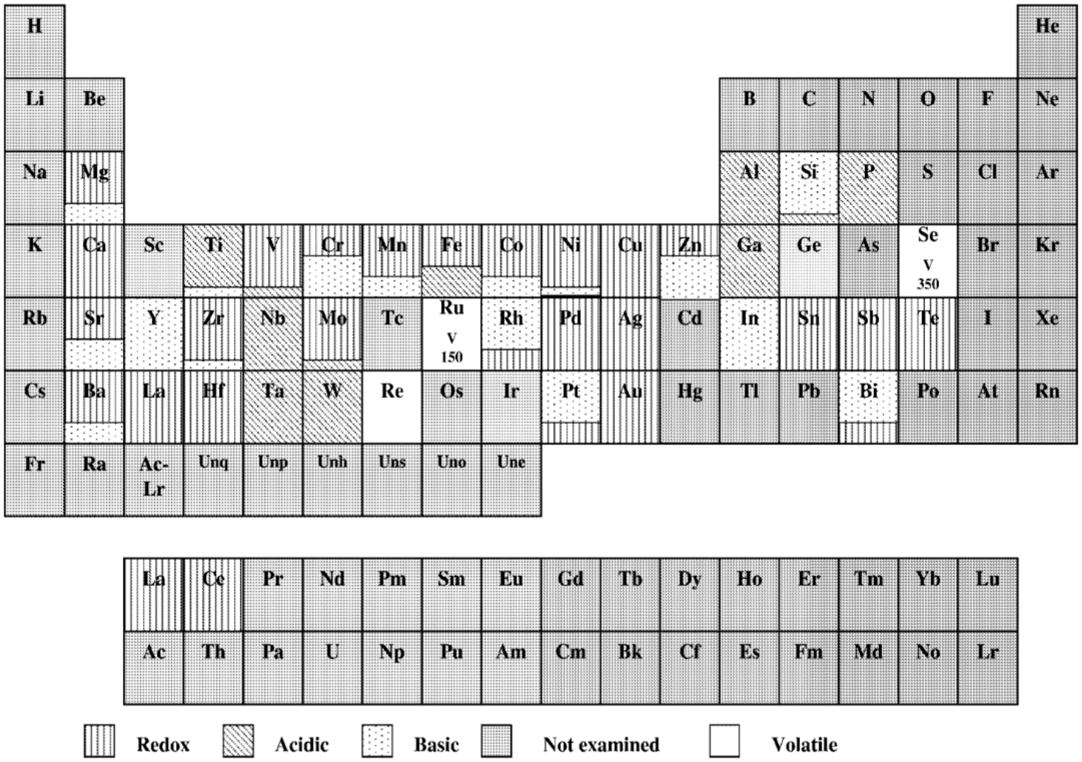

As shown in Table 1.2, the catalytic activity of metal oxides is heavily dependent on the metal ions and their bonding environment within the oxides.

Firstly, the oxidation state of metal ion plays a key role since the valence electrons are highly correlated with the acidity and redox behavior of the metal centers.

Secondly, the bonding characteristics between metal and oxygen atoms are also relevant here. Many experimental and theoretical studies indicate, that different metal-oxygen bonds exhibited different catalytic activity. For example, vanadium tri-oxo group has been identified as active sites for methanol partial oxidation reactions.[43] For $(MO_3)_n$

oxide (M=Mo, W), di-oxo groups are found to have a higher Lewis acidity than mono-oxo and bridge oxygen sites.[52] In some other circumstances, the metal-oxygen bond strength has to do with the reducibility of the metal center, which is critical to redox reactions.[53]

Other factors which may also contribute the catalytic activity of metal oxides, are surface and bulk defects, i.e. oxygen vacancy and surface hydroxyl group. It has been shown by Friend that the reductive coupling of benzaldehyde depends on the bulk oxygen defect density.[54] For surface hydroxyl groups, it not only changes the surface acidity as shown in zeolites, but also affects the adsorption behaviors of reactants.

Lastly, it is also worth mentioning that for many catalytic reactions, mixed metal oxides are used as catalysts instead of a single oxide. In this case, the synergistic effect between two oxide species can come into play.[55] It is suggested that for some mixed oxide surface, there is an active oxide monolayer formed on the their surface. Therefore, the catalytic activity of this system could be coverage dependent.

All of the factors mentioned above underline the complexities and issues of the metal oxide catalytic systems. An obvious way to resolve all the problems is to develop a suitable model system, which carries essential elements of the catalytic process and meanwhile is still available for many surface and catalytic characterization techniques.

Using metal oxide single crystal as a model system is hindered by its over-simplicity and difficulties toward many electron-based surface technique, despite of the tremendous success in TiO_2 crystal and ZnO single crystal surface.[56] For example, TiO_2 surface is well resolved by STM.(Figure 1.4 [57]) An alternative model system is called inverse catalysts, which is essentially metal oxide thin films or clusters supported by metal substrate. The as-prepared model system is subjected to most surface science characterizations, which has been used for metal single crystal surface. Thus, many successful attempts have been made to understand this system. For example, for $CeO_2(111)$ supported on Ru(0001) substrate, a STM study has directly identified the color center of Ce^{3+} sites[58]. For the same system, the dissociation of water was studied as well.[59] In addition to the inverse catalyst system, metal oxide monolayer/multilayer supported on metal oxide is also used as a model system. Compared to the inverse catalyst system, this system may be of more importance to industrial process, because the common zeolite and molecular sieve are essentially high surface area metal oxide supports. To study this model system, Raman, X-ray absorption spectroscopy, IR, NMR and UV-vis have been

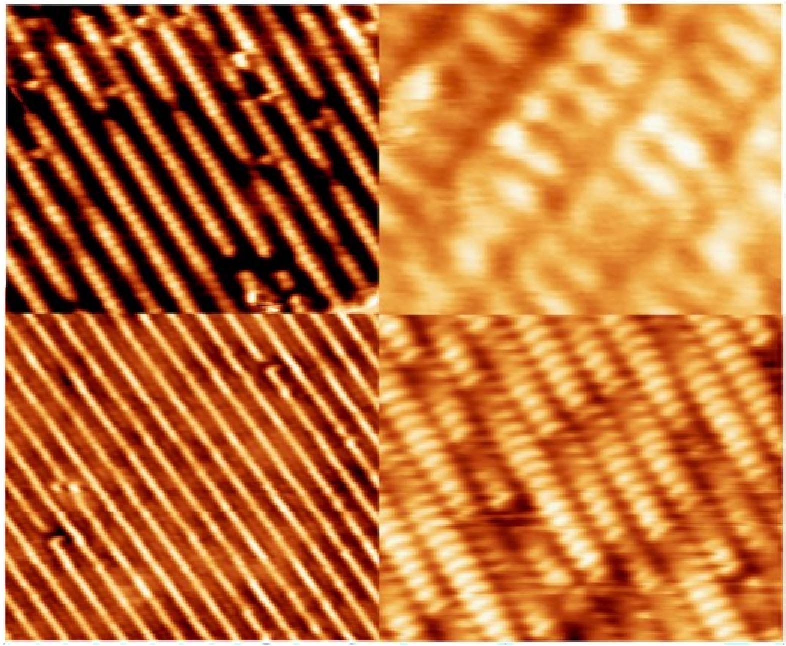

Figure 1.4 Atomic-resolved STM images on $TiO_2(110)$-(1×1) surface[57]

extensively used. Recently, more *operando* techniques are employed, such as ambient pressure XPS, which aims to provide more realistic picture of the reaction process. Studies based on this model system underscored the importance of the structure sensitivity of metal oxide systems. For example, the isometric tungsten oxide and polymeric tungsten oxide species on surface exhibit different acidity toward many catalytic reactions.[60] Similar behaviors have been observed for many other oxide systems, most of which are identified through IR and Raman spectroscopic studies. It is important to note the structures are not well controlled due to the limitation of the synthetic routes in many of these studies. *It became clear to us that the support mass selected metal oxide clusters can fill the gap between the importance of structure to catalysis and the lack of control in structure(size).* We envision that this model system can greatly benefit the understanding of the structure sensitivity of metal oxide catalysts. There have been scarce efforts on building this model system, most of which is about the tungsten oxide trimmer clusters.[53] The key reason for this is that $(WO_3)_3$ is the most abundant sublimation product of tungsten oxide powder so no mass selection is needed. Many reactions have been studied for $(WO_3)_3$ clusters, such as dehydration, dehydrogenation, condensation reaction of alcohols. The interactions between $(WO_3)_3$ clusters with various supports have been studied both theoretically and

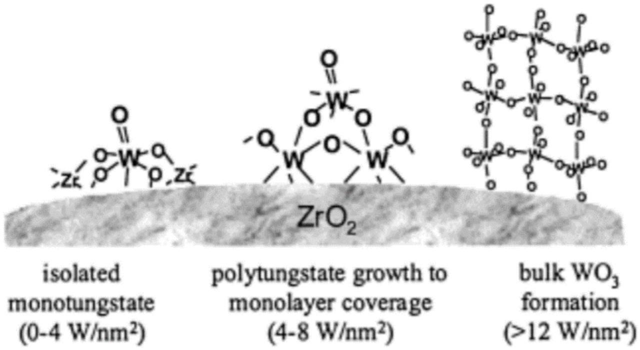

Figure 1.5 Isometric tungsten oxide and polymeric tungsten oxide[60]

experimentally. On $(TiO_2)_2$, $(WO_3)_3$ clusters exhibited six-member ring structures as shown by STM.[61] On Cu(110) surface, two dimensional $CuWO_4$ is formed.[62] On Pt(111) surface, a compact layers of $(WO_3)_3$ clusters were formed under thermal treatment.[53] On FeO(111)/Pt(111) surface, two dimensional tungstate structures were observed via STM.[63] $(WO_3)_3$ nanoclusters on the MgO(001) were also studied theoretically by density functional theory.[64] In addition to $(WO_3)_3$ clusters, VO_x clusters supported on TiO_2 were also studied via STM as well as TPD. Supported vananium oxide have been studied extensively previously and inconclusive results have been derived from various experiments.[65] Therefore, true size selected VO_x was deposited

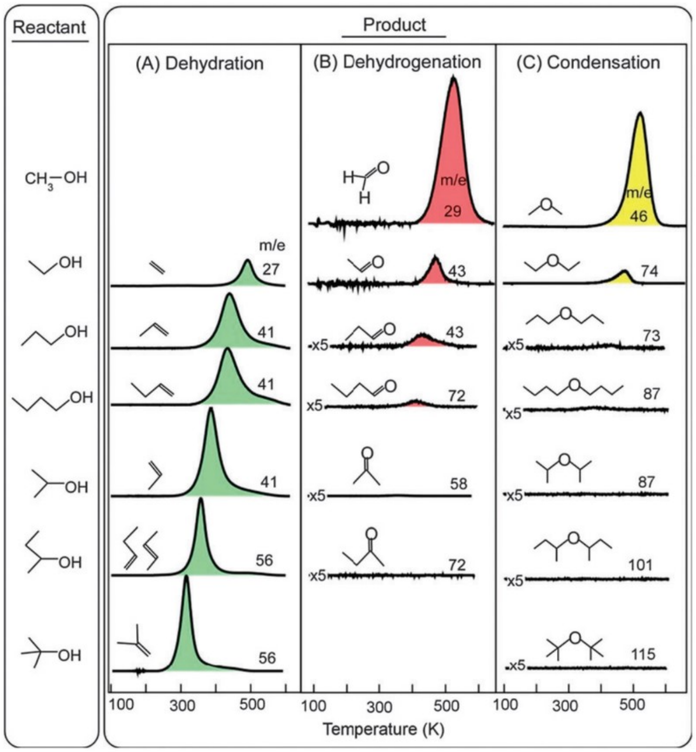

Figure 1.6 Reactions of alcohols on $(WO_3)_3$[53]

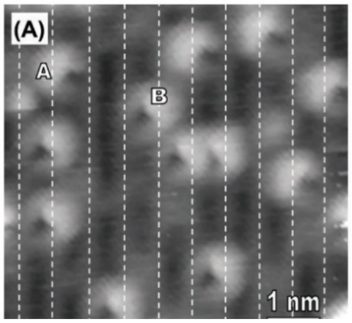

Figure 1.7 STM of $(WO_3)_3$ on TiO_2[61]

onto $TiO_2(110)$ support to study the partial oxidation reaction of methanol.[43] Additionally, supported Nb_xO_y clusters and their reactivity toward water dissociation were studied. The study concluded Nb═O oxo groups act as Lewis acid sites for water binding and subsequent dissociation.[49] All the studies for size selected metal oxide clusters strongly suggested the importance of the structure of oxide clusters specially the bonding between metal-oxide bonds.

References

(1) Günther, R.; Christian, W. Journal of Physics: Condensed Matter 2008, 20, 184019.

(2) Kolasinski, K. W. Surface science : foundations of catalysis and nanoscience; 3rd ed.; Wiley: Chichester, West Sussex ; Hoboken, N.J., 2012.

(3) Astruc, D.; Lu, F.; Aranzaes, J. R. Angew Chem Int Ed Engl 2005, 44, 7852.

(4) Harding, C.; Habibpour, V.; Kunz, S.; Farnbacher, A. N.; Heiz, U.; Yoon, B.; Landman, U. J Am Chem Soc 2009, 131, 538.

(5) Landman, U.; Yoon, B.; Zhang, C.; Heiz, U.; Arenz, M. Top Catal 2007, 44, 145.

(6) Yoon, B.; Hakkinen, H.; Landman, U.; Worz, A. S.; Antonietti, J. M.; Abbet, S.; Judai, K.; Heiz, U. Science 2005, 307, 403.

(7) Bonanni, S.; Ait-Mansour, K.; Brune, H.; Harbich, W. Acs Catal 2011, 1, 385.

(8) Abbet, S.; Sanchez, A.; Heiz, U.; Schneider, W. D.; Ferrari, A. M.; Pacchioni, G.; Rösch, N. Surface Science 2000, 454–456, 984.

(9) Worz, A. S.; Judai, K.; Abbet, S.; Heiz, U. Journal of the American Chemical Society 2003, 125, 7964.

(10) Lee, S.; Molina, L. M.; Lopez, M. J.; Alonso, J. A.; Hammer, B.; Lee, B.; Seifert, S.; Winans, R. E.; Elam, J. W.; Pellin, M. J.; Vajda, S. Angew Chem Int Edit 2009, 48, 1467.

(11) Lee, S.; Di Vece, M.; Lee, B.; Seifert, S.; Winans, R. E.; Vajda, S. Phys Chem Chem Phys 2012, 14, 9336.

(12) Kane, M. D.; Roberts, F. S.; Anderson, S. L. Faraday Discuss 2013.

(13) Kane, M. D.; Roberts, F. S.; Anderson, S. L. Int J Mass Spectrom 2014, 370, 1.

(14) von Weber, A.; Baxter, E. T.; Proch, S.; Kane, M. D.; Rosenfelder, M.; White, H. S.; Anderson, S. L. Phys Chem Chem Phys 2015, 17, 17601.

(15) Proch, S.; Wirth, M.; White, H. S.; Anderson, S. L. Journal of the American Chemical Society 2013, 135, 3073.

(16) Roberts, F. S.; Kane, M. D.; Baxter, E. T.; Anderson, S. L. Phys Chem Chem Phys 2014, 16, 26443.

(17) von Weber, A.; Baxter, E. T.; White, H. S.; Anderson, S. L. J Phys Chem C 2015, 119, 11160.

(18) Kaden, W. E.; Wu, T. P.; Kunkel, W. A.; Anderson, S. L. Science 2009, 326, 826.

(19) Kaden, W. E.; Kunkel, W. A.; Roberts, F. S.; Kane, M.; Anderson, S. L. Surf Sci 2014, 621, 40.

(20) Lee, S. S.; Fan, C. Y.; Wu, T. P.; Anderson, S. L. Journal of the American Chemical Society 2004, 126, 5682.

(21) Lee, S.; Fan, C. Y.; Wu, T. P.; Anderson, S. L. Journal of Chemical Physics 2005, 123.

(22) Fan, C. Y.; Wu, T. P.; Kaden, W. E.; Anderson, S. L. Surface Science 2006, 600, 461.

(23) Lee, S.; Lee, B.; Seifert, S.; Winans, R. E.; Vajda, S. J Phys Chem C 2015, 119, 11210.

(24) Lee, S.; Lee, B.; Mehmood, F.; Seifert, S.; Libera, J. A.; Elam, J. W.; Greeley, J.; Zapol, P.; Curtiss, L. A.; Pellin, M. J.; Stair, P. C.; Winans, R. E.; Vajda, S. Journal of Physical Chemistry C 2010, 114, 10342.

(25) Kwon, G.; Ferguson, G. A.; Heard, C. J.; Tyo, E. C.; Yin, C. R.; DeBartolo, J.; Seifert, S.; Winans, R. E.; Kropf, A. J.; Greeley, J.; Johnston, R. L.; Curtiss, L. A.; Pellin, M. J.; Vajda, S. Acs Nano 2013, 7, 5808.

(26) Habibpour, V.; Yin, C. R.; Kwon, G.; Vajda, S.; Palmer, R. E. J Exp Nanosci 2013, 8, 993.

(27) Lei, Y.; Mehmood, F.; Lee, S.; Greeley, J.; Lee, B.; Seifert, S.; Winans, R. E.; Elam, J. W.; Meyer, R. J.; Redfern, P. C.; Teschner, D.; Schlogl, R.; Pellin, M. J.; Curtiss, L. A.; Vajda, S. Science 2010, 328, 224.

(28) Vajda, S.; Pellin, M. J.; Greeley, J. P.; Marshall, C. L.; Curtiss, L. A.; Ballentine, G. A.; Elam, J. W.; Catillon-Mucherie, S.; Redfern, P. C.; Mehmood, F.; Zapol, P. Nat Mater 2009, 8, 213.

(29) Liu, C.; Yang, B.; Tyo, E.; Seifert, S.; DeBartolo, J.; von Issendorff, B.; Zapol, P.; Vajda, S.; Curtiss, L. A. J Am Chem Soc 2015, 137, 8676.

(30) Abbet, S.; Heiz, U.; Ferrari, A. M.; Giordano, L.; Di Valentin, C.; Pacchioni, G. Thin Solid Films 2001, 400, 37.

(31) Heiz, U.; Sanchez, A.; Abbet, S.; Schneider, W. D. Journal of the American Chemical Society 1999, 121, 3214.

(32) Nesselberger, M.; Roefzaad, M.; Hamou, R. F.; Biedermann, P. U.; Schweinberger, F. F.; Kunz, S.; Schloegl, K.; Wiberg, G. K.; Ashton, S.; Heiz, U.; Mayrhofer, K. J.; Arenz, M. Nature materials 2013, 12, 919.

(33) Schweinberger, F. F.; Berr, M. J.; Doblinger, M.; Wolff, C.; Sanwald, K. E.; Crampton, A. S.; Ridge, C. J.; Jackel, F.; Feldmann, J.; Tschurl, M.; Heiz, U. J Am Chem Soc 2013, 135, 13262.

(34) Crampton, A. S.; Rotzer, M. D.; Ridge, C. J.; Schweinberger, F. F.; Heiz, U.; Yoon, B.; Landman, U. Nat Commun 2016, 7.

(35) Heiz, U.; Sanchez, A.; Abbet, S.; Schneider, W. D. Chem Phys 2000, 262, 189.

(36) Tang, X.; Schneider, J.; Dollinger, A.; Luo, Y.; Worz, A. S.; Judai, K.; Abbet, S.; Kim, Y. D.; Gantefor, G. F.; Fairbrother, D. H.; Heiz, U.; Bowen, K. H.; Proch, S. Phys Chem Chem Phys 2014, 16, 6735.

(37) Moseler, M.; Walter, M.; Yoon, B.; Landman, U.; Habibpour, V.; Harding, C.; Kunz, S.; Heiz, U. J Am Chem Soc 2012, 134, 7690.

(38) Yoon, B.; Landman, U.; Habibpour, V.; Harding, C.; Kunz, S.; Heiz, U.; Moseler, M.; Walter, M. J Phys Chem C 2012, 116, 9594.

(39) Judai, K.; Abbet, S.; Worz, A. S.; Ferrari, A. M.; Giordano, L.; Pacchioni, G.; Heiz, U. Journal of Molecular Catalysis a-Chemical 2003, 199, 103.

(40) Bonanni, S.; Ait-Mansour, K.; Harbich, W.; Brune, H. Journal of the American Chemical Society 2012, 134, 3445.

(41) Bonanni, S.; Ait-Mansour, K.; Harbich, W.; Brune, H. J Am Chem Soc 2014, 136, 8702.

(42) Tong, X.; Benz, L.; Kemper, P.; Metiu, H.; Bowers, M. T.; Buratto, S. K. Journal of the American Chemical Society 2005, 127, 13516.

(43) Price, S. P.; Tong, X.; Ridge, C.; Neilson, H. L.; Buffon, J. W.; Robins, J.; Metiu, H.; Bowers, M. T.; Buratto, S. K. The Journal of Physical Chemistry A 2014, 118, 8309.

(44) Tong, X.; Benz, L.; Chretien, S.; Kemper, P.; Kolmakov, A.; Metiu, H.; Bowers, M. T.; Buratto, S. K. Journal of Chemical Physics 2005, 123.

(45) Habibpour, V.; Song, M. Y.; Wang, Z. W.; Cookson, J.; Brown, C. M.; Bishop, P. T.; Palmer, R. E. Journal of Physical Chemistry C 2012, 116, 26295.

(46) Hu, K. J.; Plant, S. R.; Ellis, P. R.; Brown, C. M.; Bishop, P. T.; Palmer, R. E. J Am Chem Soc 2015, 137, 15161.

(47) Isomura, N.; Wu, X. Y.; Watanabe, Y. Journal of Chemical Physics 2009, 131.

(48) Watanabe, Y.; Wu, X. Y.; Hirata, H.; Isomura, N. Catal Sci Technol 2011, 1, 1490.

(49) Nakayama, M.; Xue, M.; An, W.; Liu, P.; White, M. G. The Journal of Physical Chemistry C 2015, 119, 14756.

(50) Campbell, I. M. Catalysis at surfaces; Chapman and Hall: London ; New York, 1988.

(51) Badlani, M.; Wachs, I. E. Catalysis Letters 2001, 75, 137.

(52) Li, Z.; Smid, B.; Kim, Y. K.; Matolin, V.; Kay, B. D.; Rousseau, R.; Dohnalek, Z. J Phys Chem Lett 2012, 3, 2168.

(53) Rousseau, R.; Dixon, D. A.; Kay, B. D.; Dohnalek, Z. Chem Soc Rev 2014, 43, 7664.

(54) Clawin, P. M.; Friend, C. M.; Al-Shamery, K. Chemistry 2014, 20, 7665.

(55) Feng, Z.; Lu, J.; Feng, H.; Stair, P. C.; Elam, J. W.; Bedzyk, M. J. J Phys Chem Lett 2013, 4, 285.

(56) Beck, T. J.; Klust, A.; Batzill, M.; Diebold, U.; Di Valentin, C.; Selloni, A. Phys Rev Lett 2004, 93, 036104.

(57) Sánchez-Sánchez, C.; González, C.; Jelinek, P.; Méndez, J.; Andres, P. L. d.; Martín-Gago, J. A.; López, M. F. Nanotechnology 2010, 21, 405702.

(58) Shao, X.; Jerratsch, J. F.; Nilius, N.; Freund, H. J. Phys Chem Chem Phys 2011, 13, 12646.

(59) Mullins, D. R.; Albrecht, P. M.; Chen, T.-L.; Calaza, F. C.; Biegalski, M. D.; Christen, H. M.; Overbury, S. H. The Journal of Physical Chemistry C 2012, 116, 19419.

(60) Baertsch, C. D.; Soled, S. L.; Iglesia, E. J Phys Chem B 2001, 105, 1320.

(61) Bondarchuk, O.; Huang, X.; Kim, J.; Kay, B. D.; Wang, L.-S.; White, J. M.; Dohnálek, Z. Angewandte Chemie International Edition 2006, 45, 4786.

(62) Denk, M.; Kuhness, D.; Wagner, M.; Surnev, S.; Negreiros, F. R.; Sementa, L.; Barcaro, G.; Vobornik, I.; Fortunelli, A.; Netzer, F. P. Acs Nano 2014, 8, 3947.

(63) Pomp, S.; Kuhness, D.; Barcaro, G.; Sementa, L.; Mankad, V.; Fortunelli, A.; Sterrer, M.; Netzer, F. P.; Surnev, S. J Phys Chem C Nanomater Interfaces 2016, 120, 7629.

(64) Zhu, J.; Lin, S.; Wen, X.; Fang, Z.; Li, Y.; Zhang, Y.; Huang, X.; Ning, L.; Ding, K.; Chen, W. The Journal of Chemical Physics 2013, 138, 034711.

(65) Wu, Z.; Kim, H. S.; Stair, P. C.; Rugmini, S.; Jackson, S. D. J Phys Chem B 2005, 109, 2793.

2. Experimental Methods

2.1 Vacuum Systems

Various vacuum systems have been used in our experiments, as requirements for ion transport/ selection and subsequent surface science experiments. It is known that compared to the ambient condition in vacuum conditions both neutral/charge particles have a longer mean free path.[1] In our experiment, cluster ions are created and transported over a few meters until they are finally landed, therefore, it becomes critically important for maintaining a good vacuum along the ion trajectory. On the other hand, for the electron-based surface analysis techniques, the degree of vacuum will define the mean free path of electrons, which will essentially affect the feasibility of electron spectroscopies. Lastly, for surface studies, vacuum is also needed to ensure the cleanness of the surface.

Various pumping systems have been adopted in our apparatus to achieve high vacuum or ultrahigh vacuum. Diffusion pump, turbomolecular pump and ion pumps are used to create HV/UHV environments for the experiments.

2.2 Magnetron Sputtering Source

A magnetron sputtering source is used to produce clusters ions of different materials. In general, there are several requirements that a cluster source should fulfill. Firstly, a cluster source should be able to produce cluster ions of relative strong intensity. Generally, mass selection has to work with charged particles, and the selection process results in the large loss of the cluster intensity. Secondly, a cluster sources should be able to produce clusters with wide size ranges. The type of cluster ion source used in our experiment is a magnetron sputter source, which was originally built by the group of H. Haberland. [2] The design of the magnetron sputter source is consisted of a sputtering head with a magnet in its back, a cooling system, a metal cap, and a power supply source. The function of a magnetron sputtering source is described as follows: the sputtering head is biased to -500 V, while a mixture of helium and argon is introduced to the surface of a sputtering target. The argon gas is firstly ignited by electric field and the resulting self-contained electron plasma stabilized by the magnetic field continuously ionizes the argon gas and the resulting argon ions bombard the metal surface to create metal atoms. The metal atoms are cooled down to form clusters and being transported by the helium gas. The clusters anions are formed by the collisions between electrons and neutral clusters. The design of the magnetron sputter source provides the possibility to modify the size of the produced clusters during the deposition process. To tune the cluster size, there are many parameters which can be adjusted, such as the condensation length, the amount of argon and helium gas, the voltage and the current of DC power supply, and the voltage on the iris. Additionally, it is possible to introduce reactive gases like oxygen and hydrogen sulfides into the sputtering regions resulting in production of metal compound clusters.

2.3 Magnetic Sector

Mass-selection of the clusters anions is realized via a magnetic sector. The magnetic sector works according to the Lorentz Force Law. If a charge particle moves in a magnetic field *B* and an electric filed *E* with a velocity as *v,* the Lorentz Force is given by:

$$F = q(E + v \times B)$$

The Lorentz Force is essentially providing the centripetal force when the ions move along the curved trajectory with a radius *r* inside the magnetic sector, therefore the Lorentz Force is equal to the centripetal force:

$$F = m\frac{v^2}{r}\ .$$

Meanwhile the kinetic energy of cluster ions is given by the potential energy of cluster ions, so

$$Uq = 1/2mv^2$$

where U is the leading voltage of the clusters ions.

Rearranging the above equations will ultimately give the following equations:

$$\frac{m}{q} = \frac{B^2 r^2}{2U}$$

This equation shows, one can select cluster ions with different mass/charge ratio by varying the magnetic field *B* or the leading voltage *U*. Usually, in the magnetron sputtering, only the singly charged ions are produced since the second electron attachment will have to overcome the coulomb repulsion.

2.4 X-ray Photoelectron Spectroscopy

X-ray photoelectron spectroscopy is a surface sensitive quantitative analytic technique which are widely used to study the chemical compositions of the materials. The photoelectric effect, which is first discovered by Heinrich Rudolf Hertz and later explained by Einstein, is accountable for the basic physics of XPS. A typical XPS instrument consists of an x-ray source, an electron collection lens, an electron energy analyzer, and electron detectors. The x-ray source commonly used includes Mg Kα (1253.6 eV), Al Kα (1486.6), and monochromatic Al Kα x-rays. Synchrotron radiation have also been used as x-ray sources to provide high resolution XPS analysis recently. The x-rays created an electron-hole pair. The electrons escaping from the surface are collected by the electron static lens, and their energies are analyzed by a hemispherical energy analyzer and their intensity is counted by the electron detector, usually an electron multiplier. According to the photoelectric effect, the kinetic energy of electrons is governed by the following relationship:[3]

$$E_k = hv - E_B\text{-}\phi$$

where hv is the energy of the x-ray photon being used, E_B is the binding energy of the photoelectrons that are ejected, and ϕ is the work function of the spectrometer.

X-ray photoelectron spectrum is typically plotted as the intensity of electrons (counts per second, CPS) collected versus their binding energy (E_B/ev). Each element has its own binding energy corresponding to a specific transition depending their atomic orbital configurations. This binding energy is unique to the element so it can be used as a signature for the detection of this specific element. Other than pure elemental analysis, the relative shift of binding energy for a specific element in a given chemical state is also characteristic, and known as "chemical shift". This chemical shift is often used to determine to the chemical state of the element within different materials. Similar to STM, there is also a quantum mechanical aspect of the X-ray photoelectron process. In this picture, XPS is actually used to measure the transition probabilities of electron from the initial state (binding states) to the final state (hole-electron separated pair)[3]. Regarding the initial states, electrons can be viewed as bound electrons staying within specific energy levels. For the final states, electrons are more "free", although the hole left on the surface still has a certain effect on the ejected electrons. For the cluster-based material, this is more problematic, since the screen effect has to be taken into consideration.[4] For example, a different cluster size can have a different screening on the hole (point charge). Various scale laws have been developed to rationalize this effect. It has to be mentioned that in some x-ray spectrum, some satellite peaks can also be observed due to plasmatic excitations, and special treatments will be needed in analyzing these spectra. Overall, x-ray photoelectric process is basically a linear process, following Fermi's golden rule, which gives a constant transition probability for two fixed transition states. For a known transition of a specific element, the cross-section is known and remains constant within different chemical environments. In XPS, specifically, the cross-section is known as relative sensitive factor (R.S.F.). Basically the intensity of the peak for a specific transition of a specific element is proportional to the amounts of elements within the detection volume.

Lastly, x-ray photoelectron spectroscopy achieved its surface sensitivity due to the inelastic mean free path of electrons escaped from the surface.[3] As mentioned earlier, XPS only detected the electrons ejected from the surface into the vacuum. The photo-emitted electrons are known to suffer many processes, i.e. traps, recombination, Auger process, plasmatic excitations, all of which can cause attenuations of the electron intensity. The electrons that matters in XPS are the "surviving" electrons ejected into the vacuum. The inelastic mean free path of electrons is heavily dependent on the kinetic energy of the electrons, given by the following plot.[5] Therefore, only a certain depth of electrons (0~ 10 nanometers) can be collected, which defines the surface sensitive nature of XPS.

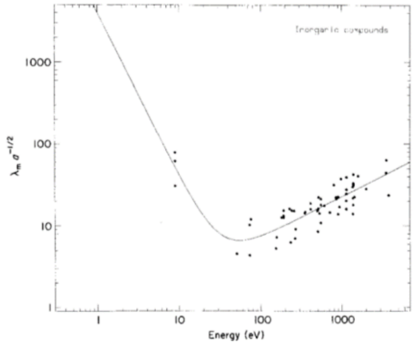

Figure 2.1 Universal Curve[5]

2.5 Temperature Programmed Desorption

Temperature programmed desorption(TPD) is a technique that measures the amount of gas desorbed from the surface when the temperature of the surface is elevated. For TPD in UHV environment, the general sequence of this process usually starts with a clean surface in UHV, a calibrated amount of gases adsorbed onto the surface at a set temperature, which then gets cool or heat to a specific temperature. The next step is to raise the temperature of surface in a well-controlled way, usually a linear ramp. Meanwhile, the evolution of adsorbates from the surface is monitored by a quadruple mass-spectrometer.

For the analysis of these desorption spectra, Redhead analysis is often used to quantitatively understand the desorption process.[6]

The desorption rate is usually described by Polanyi-Wigner equation following a power law relationship:

$$r_{des} = -\frac{d\Theta}{dt} = v_n(\Theta) e^{\left(-E_{des}/RT\right)} \Theta^n$$

Here, r_{des} is the desorption rate, and Θ is the coverage of the adsorbates, t is time, n is the order of the desorption reaction, v is the pre-exponential factor of the rate constant for desorption, E_{des} is the desorption energy, R is the gas constant, and T is the temperature of the surface. In the case of TPD in UHV, this relationship holds only when there is sufficient pumping available to prevent re-adsorption of gaseous species.

In a typical TPD experiment with a linear temperature ramp of heating rate β, we have

$$dT / dt = \beta$$

For the maximum desorption rate at $T = T_{max}$

$$\frac{d^2\Theta}{dt^2} = 0 \, .$$

Then we have

$$\frac{E_{des}}{RT_{\max}^{2}} = \frac{\mathrm{n}}{\beta} v_n \Theta^{n-1} e^{-E_{des}/RT_{\max}}$$

By assuming a first order desorption and the desorption parameter is independent of the coverage, Redhead derived a simple equation to calculate the desorption energy as shown below

$$E_{des} = RT_{\max}[\ln \frac{v_1 T_{\max}}{\beta} - \frac{E_{des}}{RT_{\max}}]$$

The second part inside the bracket is usually small enough compared to the first part, and is routinely estimated as 3.64. However, to calculate the desorption energy, the pre-exponential factor is still needed. A common chosen value for v is 10^{13} s^{-1}. To get the exact value for v, a better way is to fit the value via rate-dependent experiment.

2.6 Scanning Tunneling Microscope

The scanning tunneling microscope is one of the major techniques used to study the surface morphologies of the deposited clusters in this thesis. This technique was invented by Binnig and Heinrich Rohrer in early 1980s and later became one of the most powerful techniques in the field of surface science[7]. The mechanism of STM is based on quantum tunneling of electrons. The electron tunneling process occurs between the states of tip and sample. The barrier in-between the states of tip and the sample is the vacuum level. A mathematical expression shown below gives a more explicit description of this process. The tunneling current is given as[8]

$$I = \frac{2\pi e}{\hbar} \sum_{\mu,\nu} [f(E_\mu) - f(E_\nu)] \left|M_{\mu\nu}\right|^2 \delta(E_\nu + V - E_\mu)$$

where $f(E)$ is the Fermi function, V is the applied voltage, $M_{\mu\nu}$ is the tunneling matrix element between density of states of the respective electrodes, and E_μ is the energy of the corresponding states. Therefore, STM is essentially resolving the local density of states of the surface electronic structures. During the early development stage, STM was broadly used as an imaging tool, providing the atomic resolution images of the surface. One of the well-known example is the reconstructed Si (111)-(7x7) which was firstly resolved in real space by STM[9]. Later, STM was also used as a tool to manipulate atoms on surface to construct different surface patterns. Ho and others further developed STM into a spectroscopic tool to investigate the phonon modes of surface molecules based on inelastic electron tunneling process. All these analyzing capabilities highlight the versatility of STM as an effective local surface probe. [10]

2.7 Atomic Force Microscopy

Atomic force microcopy is used to get high resolution images of surface structures where the surface is nonconductive. Similar to STM, AFM is also a local probe. The set-up of AFM consists of a cantilever usually made of silicon or silicon nitride, laser, and arrays of photodiodes. The tip is located at the end of the cantilever. AFM works according to Hooke's Law: when the AFM tip is brought very close to the surface, the interaction/force between the tip and the surface cause the deflection of cantilever; which is measured by the position change of a reflected laser spot. When the tip is moving across the surface, the deflection is recorded accordingly to generate the topographical images of the scanning surface.

References

(1) Reich, G. *Vacuum* 1990, *41*, 2041.

(2) Haberland, H.; Karrais, M.; Mall, M. *Zeitschrift für Physik D Atoms, Molecules and Clusters* 1991, *20*, 413.

(3) Hüfner, S. *Photoelectron spectroscopy : principles and applications*; 2nd ed.; Springer: Berlin ; New York, 1996.

(4) Kaden, W. E.; Wu, T. P.; Kunkel, W. A.; Anderson, S. L. *Science* 2009, *326*, 826.

(5) Seah, M. P.; Dench, W. A. *Surface and Interface Analysis* 1979, *1*, 2.

(6) Redhead, P. A. *Vacuum* 1962, *12*, 203.

(7) Binnig, G.; Garcia, N.; Rohrer, H. *Phys Rev B Condens Matter* 1985, *32*, 1336.

(8) Bonnell, D. A. *Scanning probe microscopy and spectroscopy : theory, techniques, and applications*; 2nd ed.; Wiley-VCH: New York, 2001.

(9) Hamers, R. J.; Tromp, R. M.; Demuth, J. E. *Phys Rev Lett* 1986, *56*, 1972.

(10) Stipe, B. C.; Rezaei, M. A.; Ho, W. *Science* 1998, *280*, 1732.

3. Surface Morphologies of Size Selected Metal, Metal Oxides, Metal Sulfides Clusters on HOPG Surface

Xin Tang, Shawn Li, Yi Wang, K. Wepasnick, D. H. Fairbrother, Kit H. Bowen,

Departments of Chemistry and Materials Science, Johns Hopkins University,

T. Mangler, S. Noessner, C. Wolke, M. Grossmann, A. Koop, Gerd Gantefoer

Department of Physics, University of Konstanz, Konstanz, Germany

Abstract

Size selected metal oxide, sulfide and oxynitride clusters, soft-landed onto highly ordered pyrolytic graphite (HOPG) at room temperature, have been studied in this work. Based on their size and chemical compositions, the deposited clusters have exhibited various surface structures as illustrated by *in situ* Scanning Tunnelling Microscope (STM) and *ex situ* Atomic Force Microscope (AFM). In contrast to pure metal clusters, size selected metal compound clusters have shown different surface behaviours due to their different cluster-surface interactions.

3.1 Introduction

Clusters contain an ensemble of bound atoms whose size is intermediate between an individual molecule and a bulk solid. As such, clusters are a unique class of material which continues to attract intense scientific interest due to the fact that they often exhibit extraordinary electronic, optical, catalytic properties, etc. [1-3] Many of these properties are strongly size-dependent, e.g. gold clusters in the size regime of 2-4 nm catalyze CO oxidization at low temperatures, whereas bulk gold is catalytically inert [4]. Metal oxides have also been shown to exhibit size-dependent reactivity. For example, in a study by Castleman *et al.* [5], the reactivity of group V transition metal oxide cluster cations with *n*-butane has been shown to be strongly dependent on the number of metal atoms in the cluster. This underscores the need for means that allow one to control the size of deposited clusters as a way of tailoring the properties and functions of these nanostructures. Amongst the various methods of cluster deposition, which include conventional molecular beam [6] and wet-chemistry [7] techniques, the soft-landing of size selected gas phase clusters onto supported surfaces is a promising approach due to its ability to utilize gas phase clusters that occur in a wide range of sizes and chemical compositions. However, controlling the ultimate size, structure, and therefore functionality of deposited clusters created by this means relies on understanding the relationships between the size of the incident gas phase clusters and the nature of the deposited clusters, determined by cluster-cluster and cluster-surface interactions [8,9].

Our knowledge of the structures that gas phase clusters adopt on solid surfaces comes predominantly from studies on metal clusters deposited by soft-landing, or, in a few cases, low energy ion beam deposition on atomically smooth surfaces such as highly ordered pyrolytic graphite (HOPG) and mica [10-17]. In general, the surface structures formed have been found to depend on the size of the incident gas phase clusters. For example, antimony clusters deposited on graphite surface coalesce into larger clusters when the incident cluster size is small (Sb_4). In contrast, cluster-cluster interactions become less favorable when larger incident antimony clusters (Sb_{350}, Sb_{2200}) are deposited [11]. These size-dependent effects are ascribed to the lower surface mobility of larger clusters, coupled with their greater thermodynamic stability due to the lower fraction of surface atoms. The observations are, in turn, consistent with experiments on gold clusters. In a series of experiments, small gold clusters (Au_1, Au_3, Au_7) were observed to be mobile on HOPG before coalescing into larger clusters with a much larger diameter [18], while large gold clusters (Au_{250}) were less mobile and only partially coalesced into fractal structures [19]. However, in experiments performed using size selected silver clusters, it was observed that silver clusters containing 50 to 250 atoms deposited onto HOPG diffuse and coalesce into larger nanoparticles with a diameter of about 14 nm, irrespective of the incident gas phase cluster size [13]. In contrast, our knowledge of the size-dependent surface behavior of metal compound clusters (e.g, metal oxides[20-22], sulfides[23], nitrides), is extremely limited despite their importance in catalysis and material science [24].

From these discussions, understanding how the size of incident metal compound clusters affects their surface structures and properties is clearly important. In this proceeding, we have focused on three different types of clusters: molybdenum oxides, lead sulfides, and titanium oxynitrides. Results obtained by local probe microscopes reveal that these metal compounds sometimes result in significantly different surface structures from their pure metal clusters. We attribute these differences to their different cluster-cluster and cluster-surface interactions.

3.2 Apparatus

Cluster anions were produced by the cluster deposition apparatus shown in Figure 3.1. Briefly, a metal target was placed in a cylindrical magnetic field and biased to -500 V. A mixture of argon and helium was then introduced into the source. Argon ions created within the source sputtered the metal target, producing metal clusters. To produce different types of clusters, different reactive gases were introduced to react with the metal cluster vapors: Oxygen (O_2) was used to produce oxide clusters; metal sulfides were prepared by reacting metal ions with hydrogen sulfide (H_2S); finally, for titanium oxynitride clusters, nitrogen was provided by ammonium gas (NH_3), and oxygen came from residual gases such as water (H_2O). The added helium served to cool and transport the ions downstream.

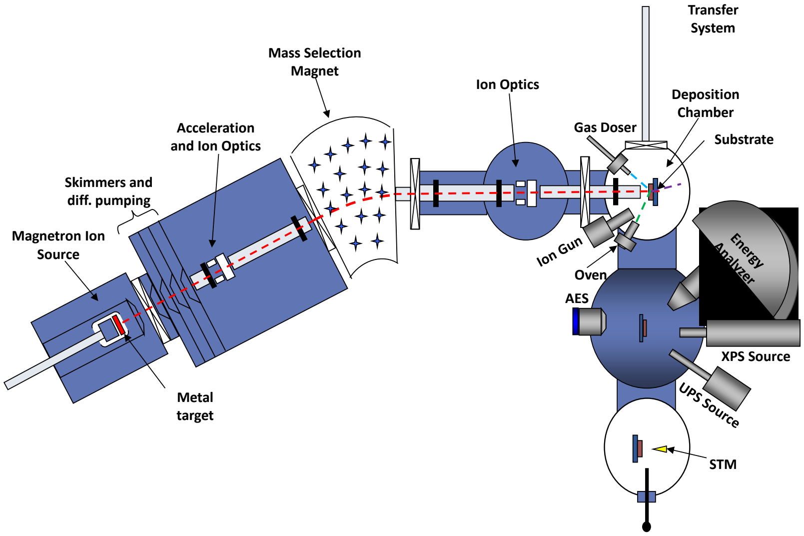

Figure 3.1 Schematic of our apparatus, showing the cluster deposition, beam-line, and the surface analytical instrumentation.

After the clusters anions were produced, they were accelerated before entering a magnetic sector mass spectrometer (25◦ sector magnet with resolution of $m/\Delta m= 20$). By tuning the magnetic field strength and/or the ion energy, clusters of various sizes were mass-selected and then passed through a series of ion optics before entering a Ultra-High Vacuum (UHV) deposition chamber where they were soft-landed (kinetic energy < 0.1eV/atom) onto a 1 cm^2 piece of freshly peeled HOPG.

Once clusters had been deposited onto the HOPG substrate, samples could be internally transferred to the adjunct UHV chamber, where they could be characterized by *in situ* Auger electron spectroscopy (AES), X-ray Photoelectron Spectroscopy (XPS), and

Scanning Tunneling Microscopy (STM). *Ex situ* Atomic force microscopy (AFM) was also employed to characterize the structures of deposited clusters.

3.3 Structures of Size Selected of Clusters on Surfaces

3.3.1 Metal /Metal Oxide Clusters on HOPG

The mobility and aggregation behaviors of metal versus metal oxide clusters on HOPG surfaces have been examined as a function of their coverage. To accomplish this, mass-selected, cluster anion beams of Mo_{100}^- and $(MoO_3)_{67}^-$ were produced in a magnetron sputter source and soft-landed onto HOPG under UHV conditions. These two clusters were chosen because they possess essentially the same masses and consequently could be soft-landed with the same low kinetic energies, resulting in deposition energies of ~0.1 eV/ atom. The *in situ* AES confirmed the chemical composition of molybdenum metal and metal oxide clusters, respectively. Their surface morphologies were then characterized as a function of cluster coverage by using *in situ* STM and *ex situ* AFM. Both STM and AFM results indicated high mobility for the metal atom clusters on HOPG at room temperature as shown Figure 3.2(a) and Figure 3.3.

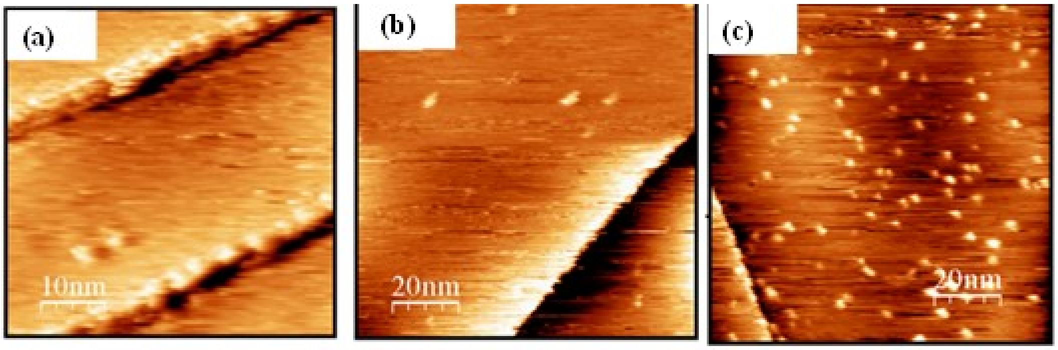

Figure 3.2 Deposited (a) Mo_{100} clusters and (b)(c) $(MoO_3)_{67}$ clusters on HOPG imaged by *in situ* STM .

At low coverages, Mo_{100} clusters migrated over the surface and nucleated preferentially at step edges as shown in Figure 3.2(a) and Figure 3.3(a), but at higher coverages they aggregated on the terraces until a fully saturated over-layer was eventually created, as shown in Figure 3.3(b). This behavior by metal clusters on HOPG surfaces was in accordance with prior studies on other metal cluster systems due to the high mobility of metal clusters on HOPG substrates.[10] With the same low kinetic energies and the same masses, one might have expected the metal oxide clusters to disperse over HOPG in the same way. In contrast with Mo_{100} metal clusters, the $(MoO_3)_{67}$ oxide clusters, instead of showing high mobility, produced a random array of adsorbed clusters at all coverages as shown in Figure 3.2(b)(c) . Consequently, on the same type of surface and with the same energy per atom, these metal oxide clusters were comparatively immobile relative to metal clusters, and differences in the mobility and aggregation behaviors of Mo_{100} and $(MoO_3)_{67}$ clusters at room temperature were attributed to differences in the interactions of metal and metal oxide clusters with carbonaceous surfaces.

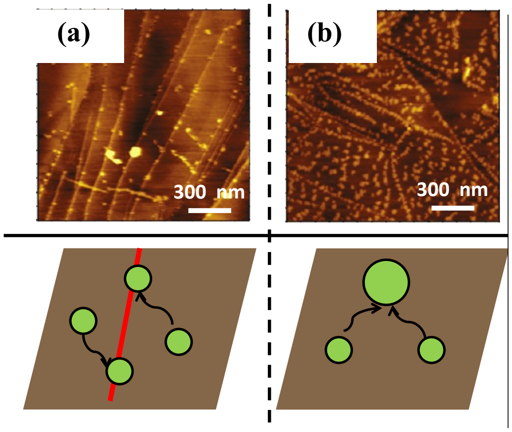

Figure 3.3 Deposited Mo_{100} clusters on HOPG imaged by *ex situ* AFM: (a) low coverage (b) high coverage

3.3.2 Lead Sulfide: Its Clusters and its Embryonic Crystal

It has been a goal of cluster science to connect the microscopic, molecular level world to the macroscopic, bulk level world. [1]In particular, at what size do clusters (aggregates) first take on properties which are characteristic of the bulk? Here, we are interested in identifying the smallest, viable crystalline unit of the lead sulfide rock salt crystal, i.e., its “baby crystal."[23]

To set the stage for the STM studies of “baby crystals," our previous work combined both experiments and theory to explore the geometric structures and electron affinities of small, gas-phase, lead sulfide clusters, $(PbS)_n$, ranging in size from n = 2-15. [25]

First, photoelectron spectroscopy was conducted on size-selected cluster anions to acquire both ground and excited state electronic structure information as well as the electron affinity values of the cluster anions’ neutral counterparts. Figure 3.4 and Figure 3.5 display the calculated geometric structures of neutral and anionic $(PbS)_n$ clusters with n=1-10, respectively. Further comparison of the calculated electron affinities and vertical detachment energies with measured photoelectron spectra has authenticated the calculated structures. Among these calculated structures, the $(PbS)_4$ cube was found to be the most stable of the lead sulfide clusters studied due to a large, calculated HOMO-LUMO gap (2.96 eV), and it was also suggested to be the preferred product of cluster fragmentation processes. These findings are consistent with the fact that the primitive cell in crystalline lead sulfide is made up of four lead sulfide molecules. Notably, a structural growth pattern for the lowest energy isomers in this cluster size range has been proposed here based on a two-dimensional stacking of face-sharing (side-by-side) lead sulfide cubical units. For example, the face sharing of $(PbS)_4$ cube would lead to the lowest energy isomer of $(PbS)_8$.

However, over the studied size range, the lead and sulfur atoms in these structures possessed a maximum of five-fold coordination, rather than the six-fold coordination found in bulk, lead sulfide crystals. As a general conclusion for these calculated structures, lead sulfide clusters in this size range form slightly distorted, fused cuboids.

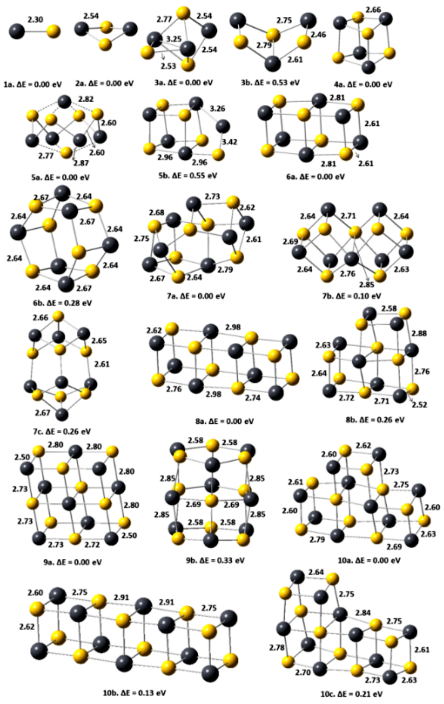

Figure 3.4 The lowest energy and higher energy isomers of neutral $(PbS)_n$ (n = 1–10) clusters.

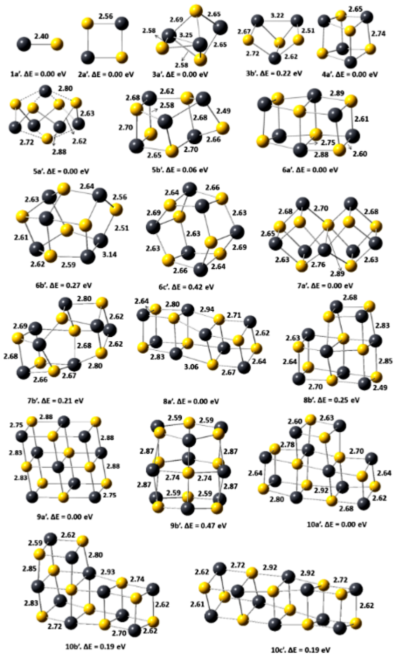

Figure 3.5 The lowest energy and higher energy isomers of anionic $(PbS)_n$ (n = 1–10) clusters.

Since lead sulfide clusters in this size range were too small to adopt bulk-like six-fold coordination, this left open the question: what is the smallest $(PbS)_n$ cluster size that can do so and that can also be replicated to form the bulk crystalline material? The successive dimerization processes from the $(PbS)_4$ cluster were used to search for this minimum cluster size, as illustrated in Figure 3.6. The dimerization leads to the formation of $(PbS)_n$ clusters from n=4 to 8, 16, and further on until 32, where the inner $(PbS)_4$ core of $(PbS)_{32}$ enjoys bulk-like six-fold coordination. On other hand, the calculated structures of $(PbS)_n$ cluster with n=12, 20, 24 did not have six-fold coordination in their bulk. According to the calculations, the lowest energy isomer of $(PbS)_{28}$ did have bulk-like six-fold coordination. However, the replication of $(PbS)_{28}$ failed to lead to the bulk rock-salt structure while $(PbS)_{32}$ did. Thus, cubic $(PbS)_{32}$ is a "*baby crystal*," i.e., the smallest cluster exhibiting six-fold coordination that can be replicated to obtain the bulk crystal. Additionally, the calculated dimensions of the $(PbS)_{32}$ cluster further provide a rubric for understanding how the successive fusion of multiple $(PbS)_{32}$ building blocks results in the formation of square and rectangular, crystalline nano-blocks, e.g., $(PbS)_{64}$, $(PbS)_{128}$, and $(PbS)_{256}$, with specific dimensions as shown in Figure 3.7.

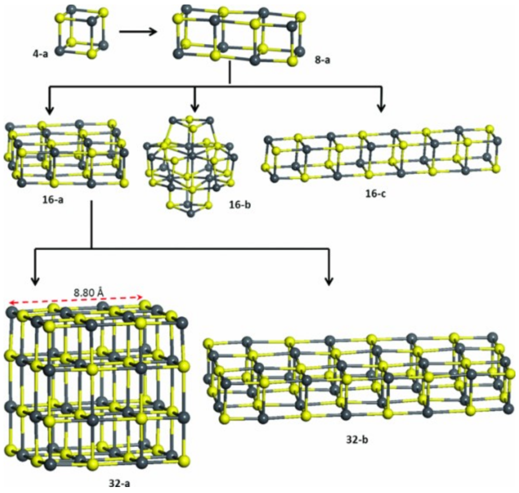

Figure 3.6 The growth pattern of lead sulfide cluster structures via dimerization of $(PbS)_{4n}$ units. For $(PbS)_{16}$ and $(PbS)_{32}$, both, the lowest, (a), and higher, ((b) and (c)), energy isomers are shown.

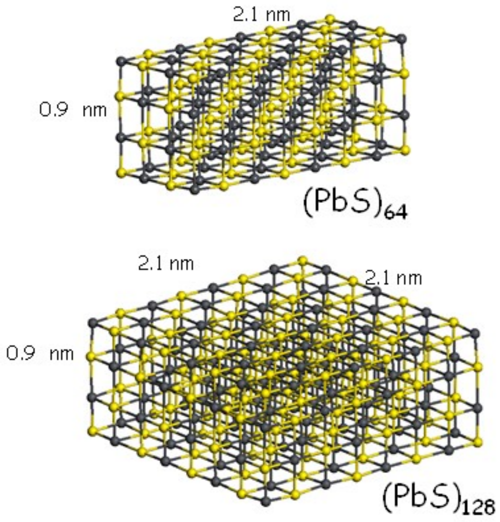

Figure 3.7 Calculated lowest energy structures for the $(PbS)_{64}$ and $(PbS)_{128}$ nano-blocks.

We then conducted cluster deposition to test the above theoretical predictions. Herein. mass-selected $(PbS)_{32}$ clusters were soft-landed onto HOPG surfaces and imaged by STM to gauge their dimensions. These dimensions were then compared with those of the fused $(PbS)_{32}$ nano-blocks predicted by theory.

The chemical compositions of lead sulfide clusters were confirmed by *in situ* XPS measurements. The XP spectra of Pb (4f) and S (2p) regions are presented in Figure 3.8. Both the peak transitions of Pb($4f_{7/2}$) centered at 137.4 eV and S(2p) centered at 160.6 eV indicated the unoxidized nature of the deposited lead sulfide clusters.[26] A further quantitative analysis of XPS results revealed that the ratio of Pb to S was found to be about 1:1, which doubly confirmed the deposition of PbS clusters.

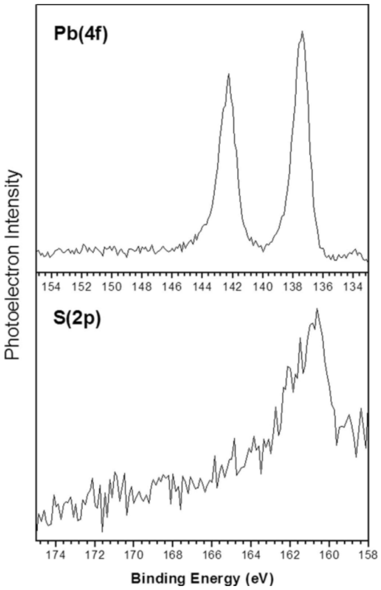

Figure 3.8 X-ray photoelectron spectra [Pb(4f) and S(2p) regions] of lead sulfide aggregates on HOPG.

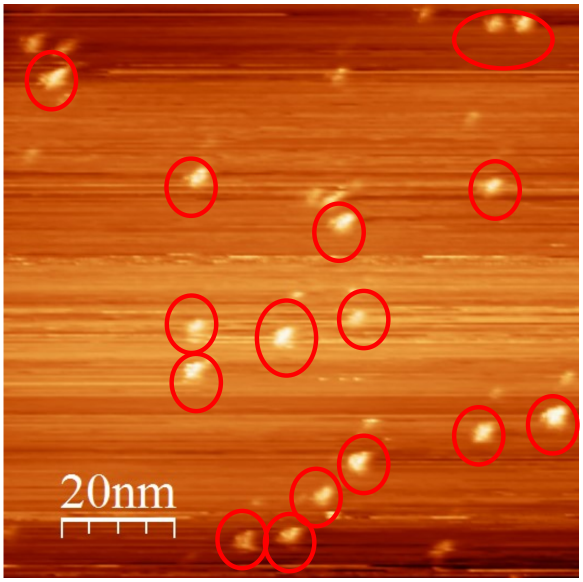

Figure 3.9 $(PbS)_{32}$ clusters deposited on HOPG by *in situ* STM

Given the presence of size-defined $(PbS)_{32}$ clusters on the surface as the starting point, we were assured that the observed STM images were the result of two-dimensional nucleation between $(PbS)_{32}$ clusters and/or between nano-blocks composed of multiple $(PbS)_{32}$ units. A typical STM image of the as deposited $(PbS)_{32}$ clusters at low coverage were displayed in Figure 3.9, in which many of these clusters exhibited non-spherical shapes, consistent with structures formed by the growth of cuboids. Two additional figures in Figure 3.10 were presented showing another two cluster that $(PbS)_{32}$ clusters have been deposited at low coverage. One of these figures shows an image of a square nano-block, while the other shows an image of a rectangular nano-block. Note that none of the clusters in the STM image have the dimensions of the originally deposited $(PbS)_{32}$ clusters; instead, they are significantly larger. This is because small $(PbS)_{32}$ clusters are mobile on HOPG; thus, they have aggregated into larger objects. Beyond qualitative assessments of shapes, STM imaging was also used to determine approximate lateral and vertical dimensions of the various aggregated clusters on the surface. We have observed STM images of these clusters, where the lateral dimensions are consistent with the predictions of theory. For example, the one labeled A has measured lateral dimensions, ~2 nm × ~2 nm corresponding to $(PbS)_{128}$. Likewise, the one labeled B has measured lateral dimensions,~4 nm × ~2 nm corresponding to $(PbS)_{256}$. Moreover, line-scans of adjacent nano-blocks, (e.g. $(PbS)_{128}$ and $(PbS)_{256}$) showed that both aggregates had heights in the range of 0.8 – 1 nm, consistent with the theoretical prediction of 0.88 nm for the heights of nano-blocks formed by the side-by-side aggregation of $(PbS)_{32}$ units. A further height analysis for a larger population of clusters was conducted to analyse the size distribution of the clusters. Consistent with the previous results, the height distribution of these clusters ranged from

0.8 to 1.2 nm, resulting from the two dimensional aggregation behaviours of $(PbS)_{32}$ clusters.

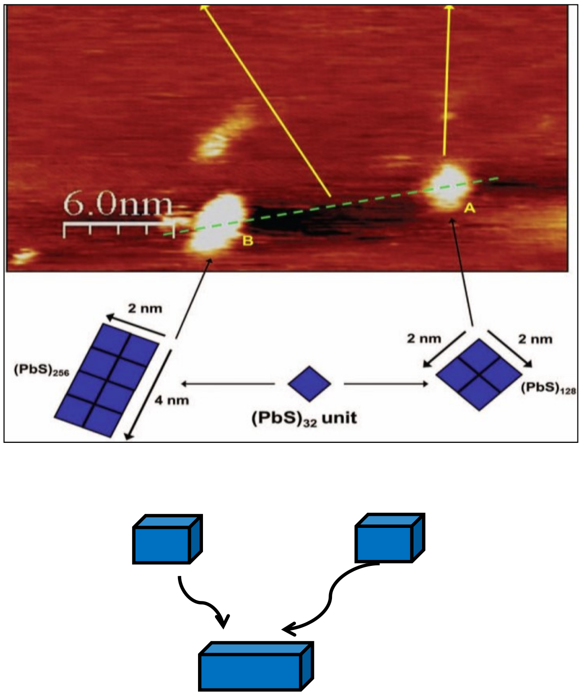

Figure 3.10 A STM image showing aggregates resulting from the soft-landing of mass-selected $(PbS)_{32}$ clusters onto a HOPG surface.

Therefore, our STM images show shapes and dimensions that are consistent with the predictions of the theoretical part of this study. Thus, this study has provided a pathway for better understanding the mechanisms involved in the formation of this class of solids.

3.3.4 Titanium Oxynitride Snowflakes (Fractals)

It is known that titanium nitride clusters, $(TiN)_n$, can be prepared by ablating or sputtering titanium metal in the presence of NH_3 or N_2 gas[27,28]. In our work, we magnetron sputtered titanium metal in the presence of ammonia and then size-selected and soft-landed

$(TiN)_{141}$ onto HOPG. While still at 10^{-9} Torr, *in situ* XPS spectra of the deposited clusters was recorded to verify the chemical compositions of the as-deposited clusters.

Figure 3.11(a) showed the presence of XPS peak features in both the Ti (2p) and N (1s) regions, with an addition peak feature in O (1s) region that suggested the presence of oxygen within the clusters. While this was unwelcome, titanium (an excellent getter) had incorporated any available oxygen into the putative titanium nitride clusters.

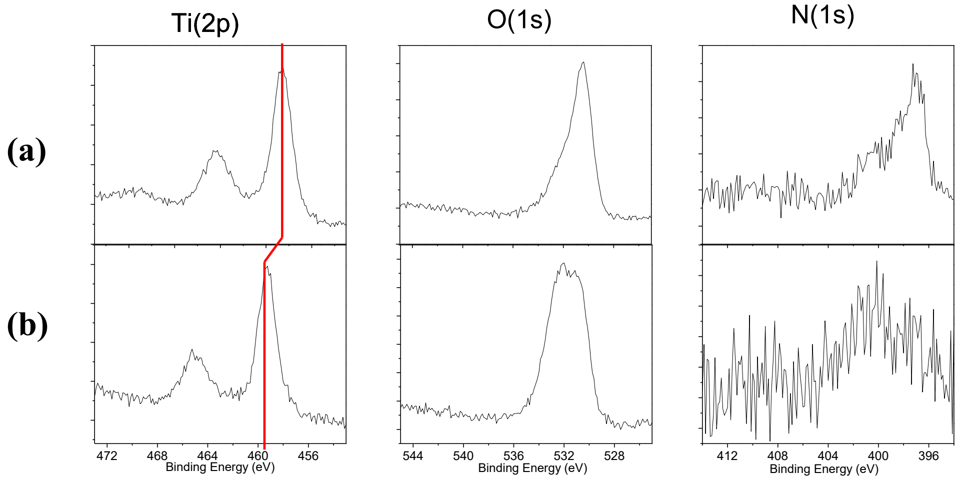

Figure 3.11 X-ray photoelectron spectra [Ti(2p), O(1s) and N(1s) regions] of (a) as-deposited and (b) air-exposed titanium oxynitride cluster aggregates on HOPG

While the sample was clearly contaminated by oxygen, thus making the as-deposited clusters essentially titanium oxynitride clusters instead of titanium nitride clusters, the clusters' surface structures were further characterized by *ex situ* AFM. This procedure necessitated exposing the sample to air. To our surprise, the resulting image in Figure 3.12 showed beautiful fractal (snowflake) patterns. The successive XPS characterization as shown Figure 3.11(b) showed the evidence for titanium and oxygen as expected, but much less nitrogen for the air-exposed clusters.

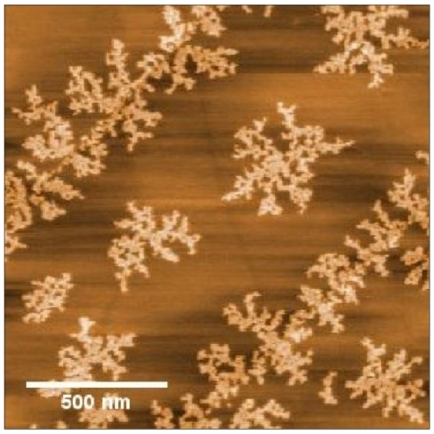

Figure 3.12 Fractal structures formed by deposited titanium oxynitride clusters

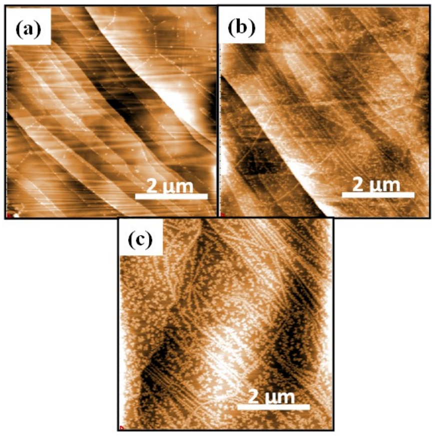

Figure 3.13 Deposited titanium oxide clusters by ex-situ AFM with coverage increasing from (a) to (c)

To study the effect of nitrogen on the structures, pure titanium oxide clusters with the same mass were produced by magnetron sputtering titanium metal with pure O_2 gas and with no NH_3 or N_2 gas. As expected, XPS confirmed that the cluster sample consisted only of titanium and oxygen. Then, the sample was exposed to air and recorded with *ex situ* AFM. No snowflakes had appeared for aggregated titanium dioxide clusters at low and medium coverages (Figure 3.13(a) and Figure 3.13(b), respectively). At much higher coverage, which corresponds to Figure 3.13(c), very small fractal structures begin to appear on the surface, indicating that, indeed, the presence of nitrogen had mattered.

The coverage of the titanium oxynitride clusters was varied systematically to investigate the formation of the fractal structures. The AFM images are shown in Figure 3.14, where coverage increases from (a) through (f). At the lowest coverage, nucleation along step edges is evident. As coverage increases, one observes randomly distributed aggregates on the terraces, which serve as feeds to further formation of fractal patterns. At the highest coverage, snowflakes are seen to form and to arrange themselves into intricate, elaborate patterns. Fractal patterns due to aggregation of atoms/molecules on surfaces have often been seen in the past, but only rarely due to mass-selected cluster deposition [10,29,30] and, to our knowledge, never under these circumstances. Usually, a diffusion-limited aggregation mechanism[31] is used to understand the growth behavior of the fractal structures. Within the growth model, the fractal formation is strongly correlated to the flux intensity of the incoming clusters from the gas phase. For low coverage, due to low flux intensity, there are not enough cluster-cluster interactions to immobilize the clusters on the terrace. Consequently, they diffuse on the terrace until they are trapped by the step edges. In contrast, as coverage increases, more cluster-cluster interactions are favored due to higher flux intensity. The abundance of cluster-cluster aggregations will then lead to the formation of nucleation seeds on the terrace as starting points for further fractal formations on the HOPG surface.

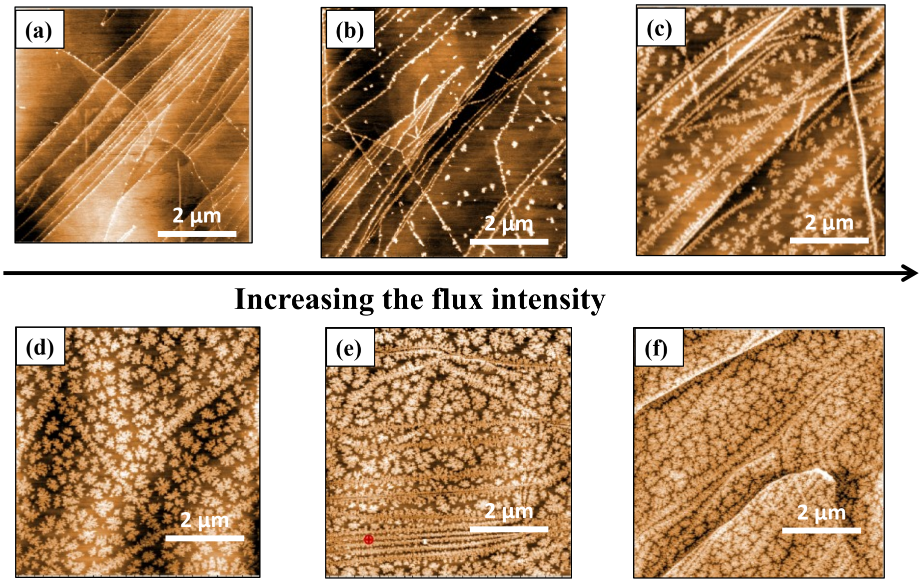

Figure 3.14 Deposited titanium oxynitride clusters by *ex situ* AFM with coverage increasing from (a) to (f)

A size-dependent study was also conducted by depositing the titanium oxynitride clusters with a different mass (3,700 amu) as presented in Figure 3.15(b). Compared to the same cluster with a higher mass (8,600 amu), the structures of clusters with lower mass showed much smaller and more compact fractal structures compared to Figure 3.15(a). The differences in structures of two clusters can be understood by an edge diffusion mechanism[32]; that is, clusters with a lower mass possess more active edge diffusion due to their higher mobility. Thus, once they are attached to the fractal island, they are more robust to diffuse along the edge in order to search for the adsorption sites corresponding to the global energy minimum. As a result, the deposition of smaller clusters will lead to more compact fractal patterns.

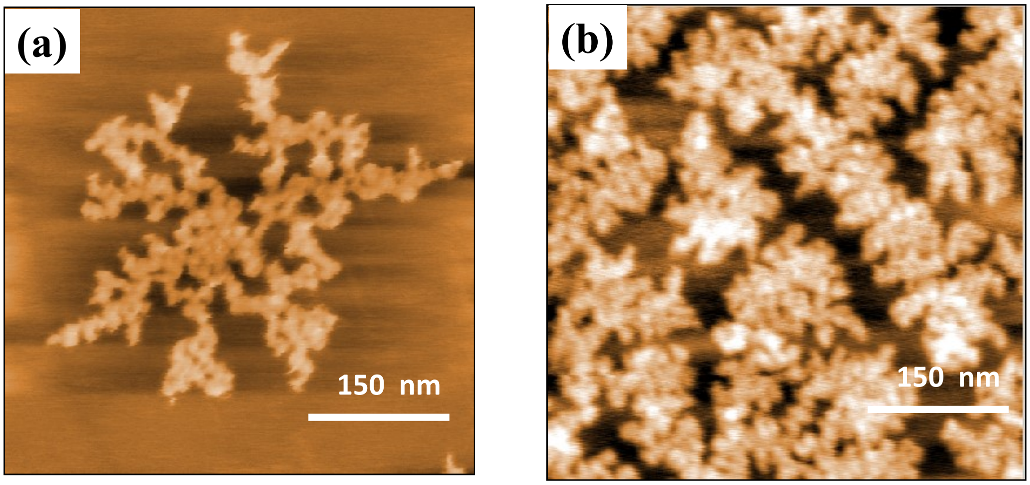

Figure 3.15 Deposited titanium oxynitride clusters by *ex situ* AFM with (a)Mass~8,600 amu and (b)Mass~3,700 amu

Herein, we have obtained fractal structures through the deposition of size-selected titanium oxynitride clusters on an HOPG surface. The nitrogen content was found to be responsible for the formation of fractal structures. Varying the flux intensity revealed the different stages of fractal growth. Furthermore, the fractal structures showed a strong size-dependent behavior, which provide possible pathways to regulating the fractal structure via size control.

3.3 Conclusion and Outlook

Three different types of systems of size-selected metal compound clusters were introduced in this proceeding. In all three systems, cluster behaviours significantly different from previously studied metal cluster systems were observed. Results from these studies illustrate how the surface morphologies of adsorbed clusters are influenced by their chemical composition, their size, and their coverage for metal compound clusters. The knowledge acquired here will benefit further applications of these metal compound clusters. For example, all three systems in this work have potential catalytic applications, i.e. molybdenum oxides are widely used in oxidative dehydrogenation, and lead sulfide is a good photocatalyst due its tunable band gap to adsorb solar light. *Thus, these supported size-selected metal compound clusters may offer a new pathway to study their catalytic properties correlated to their size, structures, and chemical compositions.*

Acknowledgments

This material is based upon work supported by the Division of Materials Science and Engineering, Basic Energy Sciences, U.S. Department of Energy, under Grant No. DE-FG02-09ER46558 (K.H.B).

References

(1) Castleman, A. W.; Bowen, K. H. *The Journal of Physical Chemistry* 1996, *100*, 12911.

(2) Morse, M. D.; Geusic, M. E.; Heath, J. R.; Smalley, R. E. *The Journal of Chemical Physics* 1985, *83*, 2293.

(3) de Heer, W. A. *Reviews of Modern Physics* 1993, *65*, 611.

(4) Hashmi, A. S. K.; Hutchings, G. J. *Angewandte Chemie International Edition* 2006, *45*, 7896.

(5) Zemski, K. A.; Justes, D. R.; Bell, R. C.; Castleman, A. W. *The Journal of Physical Chemistry A* 2001, *105*, 4410.

(6) Benten, W.; Nilius, N.; Ernst, N.; Freund, H. J. *Physical Review B* 2005, *72*, 045403.

(7) Vossmeyer, T.; Katsikas, L.; Giersig, M.; Popovic, I. G.; Diesner, K.; Chemseddine, A.; Eychmueller, A.; Weller, H. *The Journal of Physical Chemistry* 1994, *98*, 7665.

(8) Popok, V. N.; Barke, I.; Campbell, E. E. B.; Meiwes-Broer, K.-H. *Surface Science Reports* 2011, *66*, 347.

(9) Jensen, P. *Reviews of Modern Physics* 1999, *71*, 1695.

(10) Bardotti, L.; Jensen, P.; Hoareau, A.; Treilleux, M.; Cabaud, B.; Perez, A.; Aires, F. C. S. *Surface Science* 1996, *367*, 276.

(11) Bréchignac, C.; Cahuzac, P.; Carlier, M. d. F.; A. Masson, F.; Mory, C.; Colliex, C.; Yoon, B. *Physical Review B* 1998, *57*, R2084.

(12) Fuchs, G.; Melinon, P.; Santos Aires, F.; Treilleux, M.; Cabaud, B.; Hoareau, A. *Physical Review B* 1991, *44*, 3926.

(13) Goldby, I. M.; Kuipers, L.; von Issendorff, B.; Palmer, R. E. *Applied Physics Letters* 1996, *69*, 2819.

(14) Tong, X.; Benz, L.; Kemper, P.; Metiu, H.; Bowers, M. T.; Buratto, S. K. *Journal of the American Chemical Society* 2005, *127*, 13516.

(15) Tournus, F.; Bardotti, L.; Dupuis, V. *Journal of Applied Physics* 2011, *109*, 114309.

(16) Di Vece, M.; Young, N. P.; Li, Z.; Chen, Y.; Palmer, R. E. *Small* 2006, *2*, 1270.

(17) Vandamme, N.; Janssens, E.; Vanhoutte, F.; Lievens, P.; Haesendonck, C. V. *Journal of Physics: Condensed Matter* 2003, *15*, S2983.

(18) Saito, Y.; Murata, K.; Hamaguchi, K.; Fujita, H.; Kotake, S.; Suzuki, Y.; Senoo, M.; Hu, C. W.; Kasuya, A.; Nishina, Y. *Journal of Cluster Science* 1998, *9*, 123.

(19) Bardotti, L.; Prével, B.; Treilleux, M.; Mélinon, P.; Perez, A. *Applied Surface Science* 2000, *164*, 52.

(20) Wepasnick, K. A.; Li, X.; Mangler, T.; Noessner, S.; Wolke, C.; Grossmann, M.; Gantefoer, G.; Fairbrother, D. H.; Bowen, K. H. *J. Phys. Chem. C* 2011, *115*, 12299.

(21) Price, S. P.; Tong, X.; Ridge, C.; Shapovalov, V.; Hu, Z.; Kemper, P.; Metiu, H.; Bowers, M. T.; Buratto, S. K. *Surface Science* 2011, *605*, 972.

(22) White, J. M.; Bondarchuk, O.; Huang, X.; Kim, J.; Kay, B. D.; Wang, L. S.; Dohnalek, Z. *Angew. Chem.* 2006, *45*, 4786.

(23) Kiran, B.; Kandalam, A. K.; Rallabandi, R.; Koirala, P.; Li, X.; Tang, X.; Wang, Y.; Fairbrother, H.; Gantefoer, G.; Bowen, K. *The Journal of Chemical Physics* 2012, *136*, 024317.

(24) Rao, C. N. R.; Raveau, B. *Transition metal oxides : structure, properties, and synthesis of ceramic oxides*; 2nd ed.; Wiley-VCH: New York, 1998.

(25) Koirala, P.; Kiran, B.; Kandalam, A. K.; Fancher, C. A.; de Clercq, H. L.; Li, X.; Bowen, K. H. *The Journal of Chemical Physics* 2011, *135*, 134311.

(26) Osherov, A.; Matmor, M.; Froumin, N.; Ashkenasy, N.; Golan, Y. *The Journal of Physical Chemistry C* 2011, *115*, 16501.

(27) Chen, Z. Y.; Castleman, J. A. W. *The Journal of Chemical Physics* 1993, *98*, 231.

(28) Kraft, J.; Rattunde, O.; Rusu, O.; Häfele, A.; Haberland, H. *Surface and Coatings Technology* 2002, *158–159*, 131.

(29) Bréchignac, C.; Cahuzac, P.; Carlier, F.; Colliex, C.; Leroux, J.; Masson, A.; Yoon, B.; Landman, U. *Physical Review Letters* 2002, *88*, 196103.

(30) Bottcher, A.; Weis, P.; Jester, S.-S.; Loffler, D.; Bihlmeier, A.; Klopper, W.; Kappes, M. M. *Physical Chemistry Chemical Physics* 2005, *7*, 2816.

(31) Meakin, P. *Physical Review Letters* 1983, *51*, 1119.

(32) Röder, H.; Bromann, K.; Brune, H.; Kern, K. *Physical Review Letters* 1995, *74*, 3217.

4. Self-Assembly of $(WO_3)_3$ clusters on HOPG Surface and nanowire formation: a combined experimental and theoretical investigation

Xin Tang[1], Kit H. Bowen[1]

[1]Department of Chemistry, Johns Hopkins University, Baltimore, Maryland 21218, USA

Florent Calvo[2,3]

[2] Institut Lumière Matière, UMR5306 Université Lyon 1 – CNRS, Université de Lyon, 69622 Villeurbanne Cedex, France

[3]Laboratoire Interdisciplinaire de Physique, Rue de La Piscine, Campus Saint Martin d'Hères, 38000 Grenoble, France

Abstract

Tungsten oxide clusters anions $(WO_3)_3^-$ produced from a magnetron source were soft landed on highly oriented pyrolytic graphite surfaces at different temperatures, and the structures formed upon deposition were analyzed using ex-situ atomic force microscopy. Under nitrogen cooling conditions of 100 K, the clusters form small ramified nanostructures extending over a few nanometers with a height not exceeding 1 nm. At 600 K, nanowires of approximately 100 nm long and less than 10 nm diameter are observed. Dedicated atomistic modeling of the assembly process was carried out using a polarizable but nonreactive potential energy surface fitted to reproduce electronic structure calculations on small clusters, and accounting for the corrugated interaction with the

(perfect) HOPG surface. Molecular dynamics simulations reproduce the ramified nanostructures formed at low temperature fairly well, and confirm the loss of ramification at higher temperatures. However, no clear evidence is found under the much shorter length and time scales covered by the simulation for the long ordered nanowires found in the AFM pictures. Further x-ray photoelectron spectroscopy measurements additionally suggest that the nanowires nucleate along terraces through carbide defects, such chemical processes being not included in the modeling.

4.1 Introduction

Metal oxide clusters/nanoparticles are of great interest due to their applications in catalysis and material science[1] . In order to utilize metal oxide clusters, usually, they have to be dispersed into solutions or adsorbed onto an underlying support. For the latter case, the interaction between oxide clusters and supports becomes critically of importance, since it can modify both geometric and electronic structures of the metal oxide clusters. It has become well known that the surface defects[2], functional groups, electronic structures[2] of the support can alter the surface structures of the clusters. Thus understanding of the details of the interaction can have a significant impact on the application of metal oxide clusters.

Tungsten oxide trimer clusters, i.e. $(WO_3)_3$ have been well studied among many oxide clusters because they are a major sublimation product of tungsten oxides. In addition, both of the geometric and electronic structures of gas phase $(WO_3)_3^-$ clusters have been experimentally and theoretically characterized by Wang et.al., who proposed a six-member ring structure[3]. Indeed, a further STM study of $(WO_3)_3$ clusters on $TiO_2(110)$ surface[4] revealed and confirmed this six-member ring structure. Furthermore, by using

$(WO_3)_3/TiO_2(110)$ as a model system, Donalek et. al. have shown that $(WO_3)_3$ clusters on TiO_2 exhibit rich catalytic activity toward alcohol dehydration reaction[5], dehydrogenation[7] and aldehyde condensation reactions[6]. The interactions between $(WO_3)_3$ clusters with other supports have also been studied experimentally and theoretically, and many interesting structures have been found. For example, on FeO(111)/Pt(111) [7]and Cu(110) surface[10], two dimensional tungstate structures were observed via STM. On Pt(111) surface[8], a compact layer of $(WO_3)_3$ clusters was formed under thermal treatment. All these studies underlined that $(WO_3)_3$ can be used a versatile model cluster to study both the cluster-cluster interaction and cluster-surface interaction.

In the present investigation, the surface assembling behaviors of $(WO_3)_3$ clusters on HOPG were studied as a function of surface temperature and coverage by both AFM and computational modeling based on molecular dynamics (MD) simulations employing a polarizable but nonreactive potential. The simulations generally reproduce the trends observed in the measurements, except at high temperature where the nanowires observed experimentally are not so well ordered in our modeling due to too limited accessible length and time scales. While both experiment and modeling concur to show that the interaction between WO_3 and underlying graphite substrate plays an important role in determining the assembled structures of the clusters, additional x-ray photo electron spectroscopy measurements suggest that the nanowires nucleate along terraces through carbide formation, such chemical processes being not included in our modeling.

4.2 Experimental Methods

Tungsten oxide cluster anions were produced using a magnetron sputter source and mass selected via passing through a magnetic sector mass spectrometer before being soft-landed onto a HOPG surface. The apparatus for the cluster deposition has been described in detail elsewhere. [9]Tungsten oxide cluster anions were created in the magnetron ion source by reactive sputtering of a tungsten metal target in the presence of oxygen. Once produced, they were then accelerated to 1500 V before entering a magnetic sector mass spectrometer (25° sector magnet with resolution of $m/\Delta m = 20$) By adjusting the strength of magnetic field, we were able to mass-select $(WO3)_3^-$ cluster anions. After refocusing and being collimated by a series of ion optics, the size-selected $(WO_3)_3^-$ cluster anions were decelerated to kinetic energies of less than 0.1 eV per atom and soft landed onto a freshly cleaved HOPG substrate. The target can be cooled to liquid nitrogen temperature and heated by passing current through it. The pressure during cluster deposition was typically $\sim 10^{-9}$ mbar.

To characterize the surface structures of the deposited clusters, ex situ AFM was used. AFM images were acquired as a function of increasing cluster coverage. Images were acquired using a PicoSPM LE AFM (Agilent Technologies), which was operated in magnetic tapping mode using Co-Cr tips obtained from MikroMasch (NSC18). All image rendering and height measurements were performed with commercially available software from Agilent Technologies. The chemical composition of the deposited clusters were determined using in-situ XPS. This was accomplished with a PHI 5400 XPS system equipped with a Mg Kα X-ray source (1253.6 eV). XP spectra were processed with commercially available software (CasaXPS). Peak positions in the spectra were referenced to the C(1s) graphite peak (284.5 eV) of the HOPG substrate, and metal oxidation states were fit using mixed Gaussian(30%)/Lorentzian(70%) envelopes.

4.3 Computational modeling

4.3.1 Potential energy surface

Our computational approach follows the lines of our earlier work on magnesium oxide clusters [10] and relies on a polarizable many-body potential that takes into account the corrugation and dielectric nature of the graphite substrate. A fluctuating-charges model originally developed for magnesium oxide [10] was extended to treat tungsten oxide clusters. This model naturally incorporates the mixed ionic-covalent nature of the oxide bonds, and allows the partial charges carried by the ions to depend on their local coordination. With this method, the charges are not defined a priori but are obtained self-consistently to achieve electronegativity equalization for each atomic configuration. Briefly, the total interaction potential V depends on the instantaneous atomic configuration **R**= $\{r_{ij}\}$ of the ions i through a repulsive pairwise potential taken as a Born-Mayer form $V_{rep}(r_{ij})=D_{ij}\exp(-b_{ij}r_{ij})$, with r_{ij} the distance between ions i and j, D_{ij} and b_{ij} two parameters, together with an electrostatic contribution $V_Q(\mathbf{R})$ cast as

$$V_Q(R) = \sum_i [v_i q_i + \frac{1}{2} U^0_{ii} q_i{}^2 - \frac{1}{2} \alpha E_i^2] + \sum_{i<j} J_{ij}(r_{ij}) q_i q_j + \lambda(Q - \sum_i q_i)$$

In this equation q_i is the charge carried by ion i, ν_i denotes the electronegativity of element i, U^0_{ii} its hardness and α_i its isotropic atomic polarizability, and J_{ij} the Coulomb integral between ions i and j, which is approximated in the Ohno representation[11] as

$$J_{ij}(r) = \frac{1}{\left[r^2 + (U^0_{ii})^{-2} \exp\left(-\gamma_{ij} r^2\right)\right]^{1/2}}$$

which thus involves one additional damping parameter γ_{ij}. In Eq. (1) the electric field vector $\mathbf{E}_i$ on ion i is defined consistently with the Coulomb interaction J_{ij} as

$$E_i = \sum_{j \neq i} -q_j \frac{\partial J_{ij}}{\partial r_i}$$

Finally, the last term of Eq. (1) constrains the total charge of the system to equal the value Q with λ being a Lagrange multiplier.

Tungsten oxide clusters interact with the HOPG substrate on which they are deposited through two independent contributions, namely an additive repulsion-dispersion energy $V_{HOPG}(\mathbf{r})$ that accounts for the lateral corrugation of graphite via periodic functions in the corresponding dimensions[10], as well as a contribution of the substrate to the polarization energy. Following Steele [12] the first term $V_{HOPG}(\mathbf{r})$ is taken from the integration of the Lennard-Jones potential on the multilayer graphitic substrate, the successive terms of the Fourier expansion in the lateral directions x and y being denoted as $f_k(x,y)$:

$$V_{HOPG} = V_0(z_i) + V_1(z_i) f_1(x_{i,} y_i) + V_2(z_i) f_2(x_{i,} y_i)$$

in which the functions $V_k(z)$ are chosen similarly as in our previous paper [10]. In particular, instead of the cumbersome expressions for V_1 and V_2 involving Bessel functions of the second kind, more practical numerical forms were employed as

$$V_1(z_i) = \frac{1}{2} W_0 \left[\frac{A_6}{30} \left(\frac{2\pi}{\tilde{z}_i \sqrt{3}} \right)^5 K_5\left(4\pi \tilde{z}_i / \sqrt{3}\right) - 2 \left(\frac{2\pi}{\tilde{z}_i \sqrt{3}} \right)^2 K_2\left(4\pi \tilde{z}_i / \sqrt{3}\right) \right]$$

$$V_2(z_i) = \frac{1}{2} W_0 \left[\frac{A_6}{30} \left(\frac{2\pi}{\tilde{z}_i} \right)^5 K_5(4\pi \tilde{z}_i) - 2 \left(\frac{2\pi}{\tilde{z}_i} \right)^2 K_2(4\pi \tilde{z}_i) \right]$$

The HOPG substrate is also strongly polarizable and ions in contact interact with their image charges. The additional electrostatic and polarization energy originating from this interaction between the ions and the substrate was modeled as already achieved for MgO clusters, distinguishing the responses of the electric field in the parallel and perpendicular directions to the surface as [13]:

$$V_{\parallel}(R) = -\sum_i [\frac{{q_i}^2}{4z_i} - \frac{1}{2}\sum_{j\neq i}\frac{q_i q_j}{r'_{ij}}]$$

$$V_{\perp}(R) = -\sum_i [\frac{2\pi\alpha_{\perp}{q_i}^2}{8{z_i}^2} - \frac{1}{2}\sum_{j\neq i}\frac{2\pi\alpha_{\perp}q_i q_j(z_i+z_j)}{(r'_{ij})^3}]$$

In these equations z_i is the distance from ion i to the substrate and r'_{ij} the distance between ion i and the image charge of ion j on the other side of the HOPG surface, a_p=0.220 Å being the polarizability density of the graphite surface [13]. Given the linear dependence of the electric field $\mathbf{E}_i$, these additional term combine with VQ above to yield a quadratic expression as a function of q_i, which can be minimized exactly by linear algebra techniques, or in molecular dynamics using extended Lagrangian techniques[14].

The above potential was parametrized against recent quantum chemical calculations performed by Li and Dixon on isolated $(WO_3)_n$ clusters[15], for which equilibrium geometries, energy differences between isomers and even partial charges on ions were provided. The final values for the parameters are listed in Table 4.1 together with the parameters for the cluster-HOPG interaction.

Table 4.1 Parameters of the many-body potential, all expressed in atomic units.

Parameter	W	O	W-O
D	49.74	32.50	17.97
B	1.46	2.05	1.61
U	1.41	0.77	2.82
ν	-2.61	0	
α	0.073	1.56	
A_1	16436.6	319035.5	
A_2	1983271	1003294	
α_1	0.105	0.137	
α_2	$1.06\text{x}10^{-7}$	0.364	
b_1	2.983	2.966	
b_2	4.189	3.935	
σ	5.940	$1.091\text{x}10^{-4}$	
ε	6.304	$1.03\text{x}10^{-4}$	

4.3.2 Simulation protocol

The potential described in the previous section was used to simulate the growth and annealing of clusters of $(WO_3)_3$ units on the HOPG substrate. As previously used for MgO clusters on HOPG[10], a two-step procedure was employed to treat assemblies containing thousands of atoms, in which the assembly is grown sequentially by addition of a single building block on a fixed seed $[(WO_3)_3]_n$, both collision partners being treated as rigid during the approach before the product $[(WO_3)_3]_{n+1}$ is fully relaxed without the rigid constraints. For each iteration n, the relative orientations of the two partners were chosen randomly and an impact parameter b was drawn from the normalised distribution $p(b)=b/b_{max}$ where b_{max} equals the sum of the gyration radii of the two partners. The $(WO_3)_3$

projectile was thrown at the existing assembly with a fixed kinetic energy of 100 or 600 K depending on the growth conditions. Each MD trajectory assuming rigid collision partners was propagated until the distance between them came below 5 Å, at which stage a smooth fluid damping force was introduced to stop the projectile. A maximum duration of 100 ps was imposed in the (rare) situations where the projectile did not meet the target, in which cases the collision trajectory was restarted. In practice, the velocity was reduced by 0.01% every time step of 1 fs after the contact was established, as a way to mimic the dissipation of translational kinetic energy into the vibration modes of both partners and the substrate. Once the projectile had stopped, the partial charges of all atoms were calculated by minimizing the electrostatic contribution to the potential, and locally optimizing all atomic positions of the coalesced nanostructure but keeping fixed these partial charges fixed during the optimization.

4.4 Results and Discussions

4.4.1 AFM Images of $(WO_3)_3$ at 100 K

AFM images of $(WO_3)_3$ trimer clusters deposited at ~100 K were shown in Figure 4.1 with coverage increasing from (a) to (c). Upon deposited onto HOPG surface at 100 K, at low coverage $(WO_3)_3$ clusters aggregated into small fractal-like structures with an average height of 0.7 nm, indicative of the two-dimensional aggregations. By increasing the coverage, the HOPG surface are more populated with tungsten oxide aggregates until a full monolayer of tungsten oxide is achieved. After the surface was annealed to 673 K, the surface structures were also examined by AFM. The annealed oxide structures on HOPG were shown in Figure 4.1(d)-(f) with increasing coverage. Surprisingly no dramatic changes of surface structures of the clusters were observed for the AFM images of annealed oxide structures, suggesting a strong interaction between oxide clusters and the underlying graphite surface.

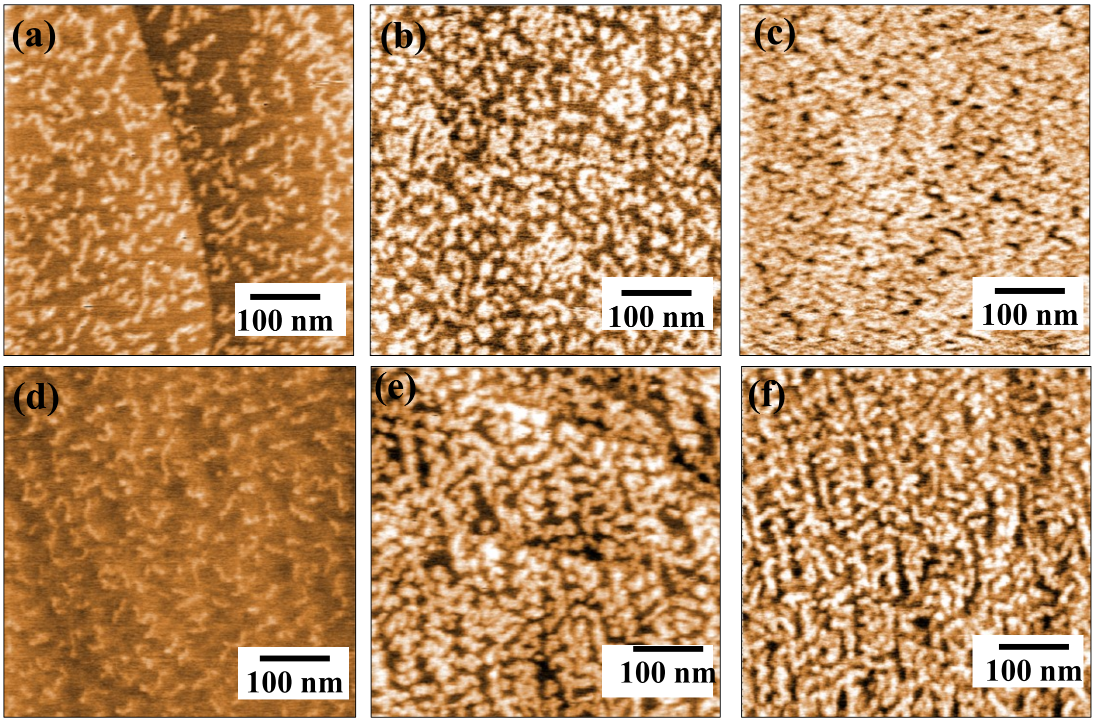

Figure 4.1. AFM Images of Deposited $(WO_3)_3$ clusters as deposited at 100K with coverage increasing from (a)-(c) and after annealing at 673 K with coverage increasing from (d)-(f)

4.4.2 AFM Images of $(WO_3)_3$ at 600 K

In contrast, while deposited at 600 K, $(WO_3)_3$ clusters on HOPG formed one-dimensional nanowire structures on terraces, approximately 100 nm long, as shown in Figure 4.2. Such nanowires have not been previously observed on HOPG. It should be mentioned that many of nanowires are oriented in a specific angle to each other, i.e. 60° or 120°, suggesting a strong interaction between $(WO_3)_3$ clusters and the underlying graphite substrate. In addition to the nanowire structures observed here, some small aggregates were also found on the terraces.

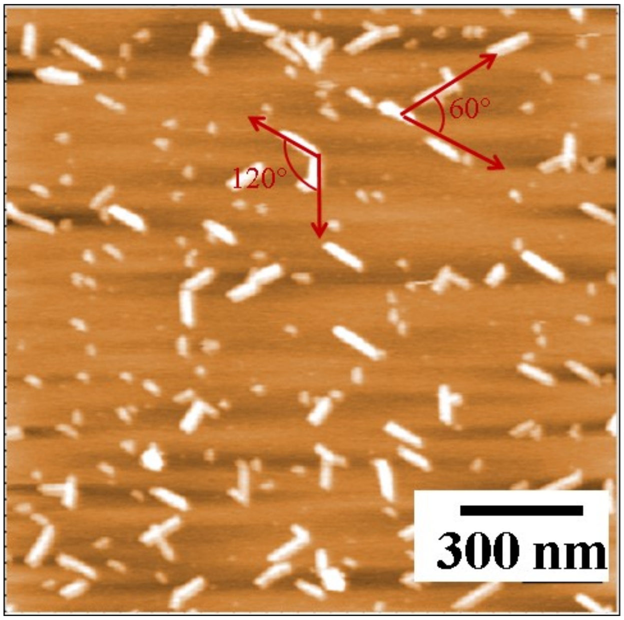

Figure 4.2 AFM Images of $(WO_3)_3$ clusters as deposited at 600 K

4.4.3 Simulation Results

A. Assessment of the many-body potential

In agreement with earlier studies, [15,16]the most stable structure of the $(WO_3)_3$ building block is the six-membered 'ring' isomer depicted in Figure 4.3(a), in which the tungsten ions are fourfold coordinated with single oxygen bridging them and two dangling oxygen atoms in tetrahedral arrangement. The partial charges on each ion predicted by the present potential and also indicated on this figure compare well with the reference quantum chemistry data, which indicates that our model is realistic. Bond distances are also within 2% of those in the DFT geometry. Upon deposition on the HOPG substrate, this structure slightly deforms (RMSD of 0.43 Å relative to the isolated configuration), as shown in Figure 4.3(b). Due to the conducting nature of the graphite substrates and its inclusion in our model, the charges vary by a few percent, especially in contact with the substrate where the variations reach about 10%.

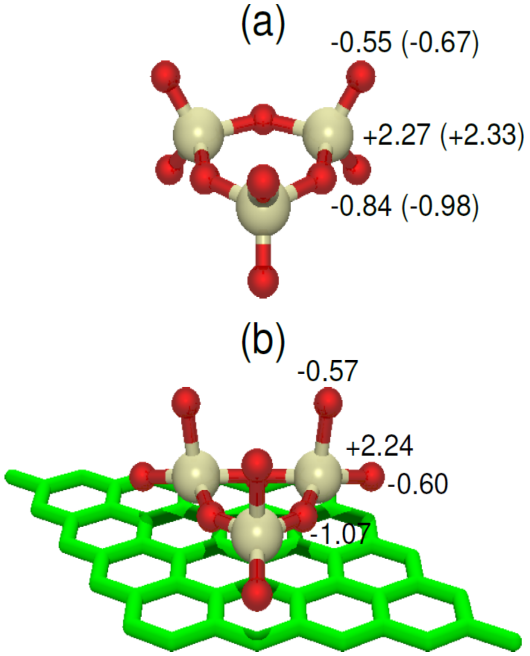

Figure 4.3 ball-and-stick representation of the most stable structure of the $(WO_3)_3$ building block, (a) in vacuum; (b) once deposited on the HOPG substrate. The effective charges on each ion are indicated, with density-functional theory reference data [15]for the isolated cluster in parentheses.

The total interaction energies of the three building blocks, defined from the optimized energies of the clusters in vacuum and in deposited form, amount to 0.42, 0.72, and 0.49 eV, respectively, the higher value obtained for the trimer originating from the better accommodation of this triangular minimum on the honeycomb lattice. These values are relatively minor in comparison with the intrinsic binding energy of the clusters, which amount to about 0.7 eV per tungsten-oxygen bond. This result is consistent with the noncovalent character of the interaction between the $(WO_3)_3$ cluster and the HOPG substrate, although polarization forces play a noticeable role.

The potential was first applied to simulate the basic coalescence between two $(WO_3)_3$ monomers on the HOPG substrate, without assuming rigid building blocks or fixed charges. Here a collision energy of 300 K was chosen, and 1000 independent trajectories were performed and stopped after 100 ps each, or if the two monomers had coalesced and formed chemical bonds at earlier times. Upon such a coalescence, a smooth friction force was added in order to relax the product to its nearby local minimum. A more accurate conjugate gradient minimization procedure was then applied in order to remove the possible residual thermal noise. Only a limited number of coalescence products was obtained from these simulations, and the statistical distribution of their occurrence is depicted in Figure 4.4 with three representative dimer structures.

The coalescence products generally undergo rather strong reorganization upon coalescence, the initial trimer structure being lost in the process. The lowest-energy 'inverted cage' configuration, which is also the most frequently obtained, bears some resemblance with the crystal form of WO_3. This preliminary investigation shows that atomistic rearrangements are significant upon coalescence of monomers, and confirms that is important to relax the geometries accordingly in our main simulation of assembly processes. However, the charges do not vary by more than 10% between the monomer and the resulting dimers, which indicates that they mainly depend on the local (fourfold) coordination of the tungsten atoms and supports our approximation of constant charges to model the growth of larger assemblies.

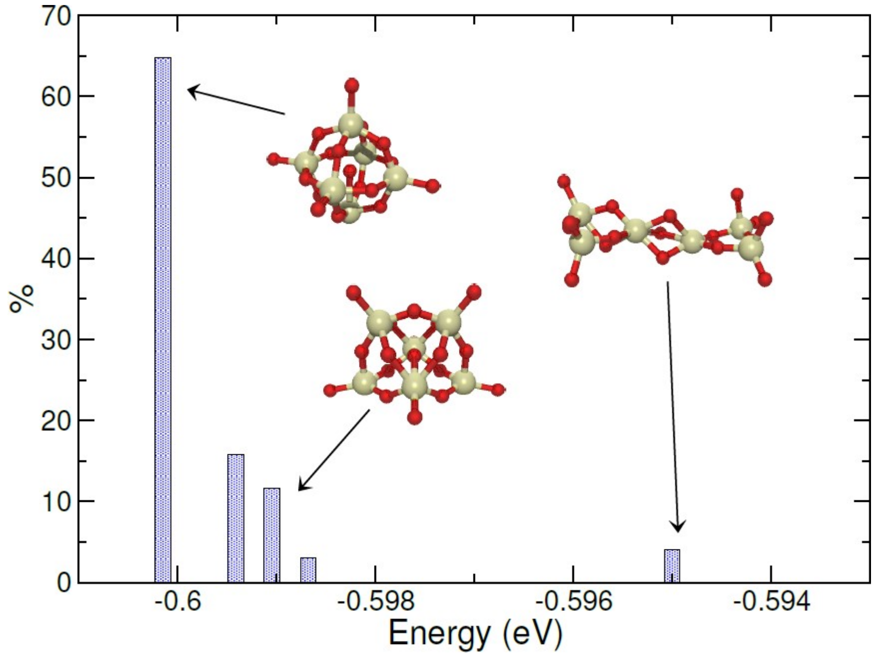

Figure 4.4 Distribution of coalescence products obtained from two $(WO_3)_3$ monomers at 300 K on HOPG, as a function of their binding energy. Three remarkable structures are highlighted

B. Simulation of the assembly process on HOPG

We now present and discuss the results obtained for the growth of $(WO_3)_3$ units into larger assemblies on HOPG, which we simulated in a stepwise fashion as described in the previous section. Two series of simulations were performed at collision energies of 100 and 600 K, the results of which are depicted in Figure 4.5. At 100 K, the assembly has a clear ramified, fractal-like character that is no longer present if the assembly is grown at 600 K. The samples obtained by successive growth have been subject to annealing at 600 K for 1 nanosecond, before being cooled down for 100 ps at 100 K in order to remove most of the thermal noise, treating all atomic degrees of freedom of the nanostructure without assuming rigid building blocks but keeping the partial charges fixed on all ions. The resulting structures, also represented in Figure 4.5, look rather similar to one another and indicate that the ramifications are lost simply by this mild heating process.

The structures of the assemblies at the atomic level were examined by relaxing the final configurations using the full potential with fluctuating charges. Unfortunately, the pair distribution functions turn out to be poorly instructive and we turn instead to the distributions of partial charges carried by the ions and heights (coordinates perpendicular to the substrate), whose distributions are represented in Figs. 6 and 7, respectively. These distributions are more sensitive to the assembly and the subsequent annealing process.

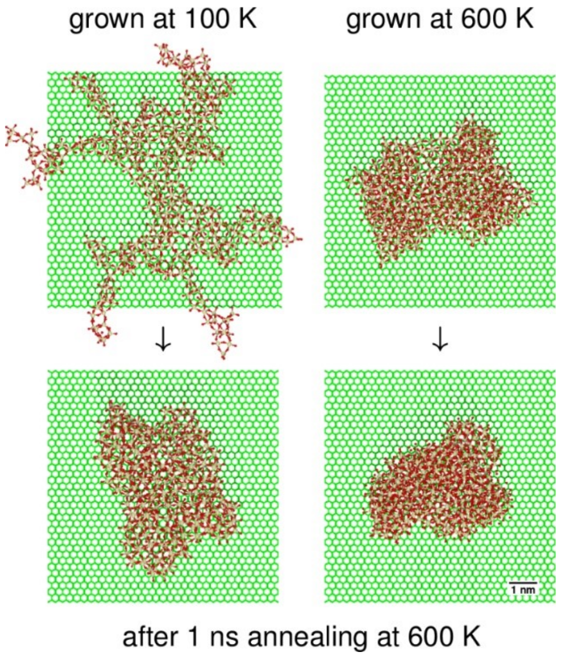

Figure 4.5 Assemblies obtained from 100 units of $(WO_3)_3$ monomer clusters at 100 or 600 K collision energies (upper panels), and after annealing at 600 K (lower panels).

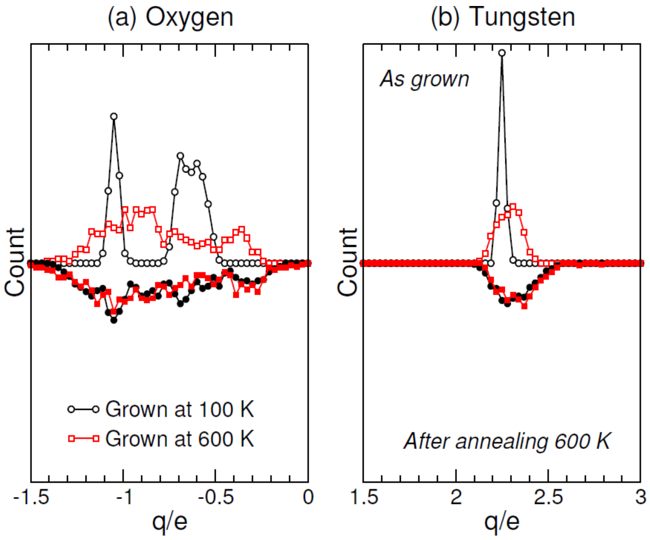

Figure 4.6 Distributions of partial charges carried by the oxygen and tungsten ions in the final $[(WO_3)_3]_{100}$ assemblies grown at 100 or 600 K (upward data), and after annealing at 600 K (downward data).

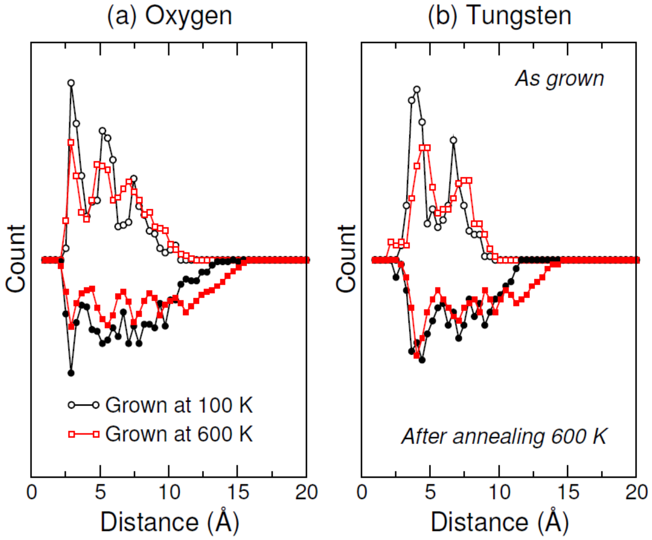

Figure 4.7 Distributions of distances of the tungsten and oxygen ions in the final $[(WO_3)_3]_{100}$ assemblies grown at 100 or 600 K (upward data), and after annealing at 600 K (downward data).

The oxide anions exhibit bimodal distributions, especially in the colder assembly, which retains most of the ordered character of the initial building block. This bimodality is associated to the different charges carried by dangling (-0.6e) and bridging (-1.05e) oxygen ions. The broadening found at 600 K and in the annealed assemblies indicates a large level of structural disorder. In contrast, tungsten ions are always fourfold coordinated with a charge close to their value of +2.27e in the isolated monomer. Structural disorder in the hot or annealed assemblies is again seen in the significant broadening.

The height distributions represented in Fig 7 are also multimodal as the result of atomistic layering near the substrate. For tungsten they expand beyond the size of the monomer, which indicates that the growth also proceeds perpendicular to the surface. This is in accordance with the results of the bimolecular collisions investigated in the previous section. The more extended height distributions found for oxygen ions are associated with the dangling bonds pointing away from the substrate.

Upon annealing, the height distributions shrink noticeably for both ion types, by about 1 Å. This shrinking is consistent with the visual depiction of the nanostructures themselves in Figure 4.5 and with the gyration radii, which vary from 317 Å to 122 Å at 100 K but also from 110 Å to 85 Å at 600 K.

Finally, we have also explored the possible interaction between two small assemblies and their merging into a larger nanostructure by simulating the coalescence process at 600 K. The growth of $(WO_3)_3$ building blocks into $[(WO_3)_3]_{100}$ at 600 K was repeated and the two products were randomly rotated and placed at 5 Å from each other and given a small negative velocity of 10-6 atomic units to trigger coalescence. A MD simulation thermostatted at 600 K was then performed for 100 ps using the approximation of fixed charges but without assumption regarding rigidity. The final product $[(WO_3)_3]_{200}$ thus obtained was finally cooled down at 100 K and locally minimized. It is depicted in Figure 4.8.

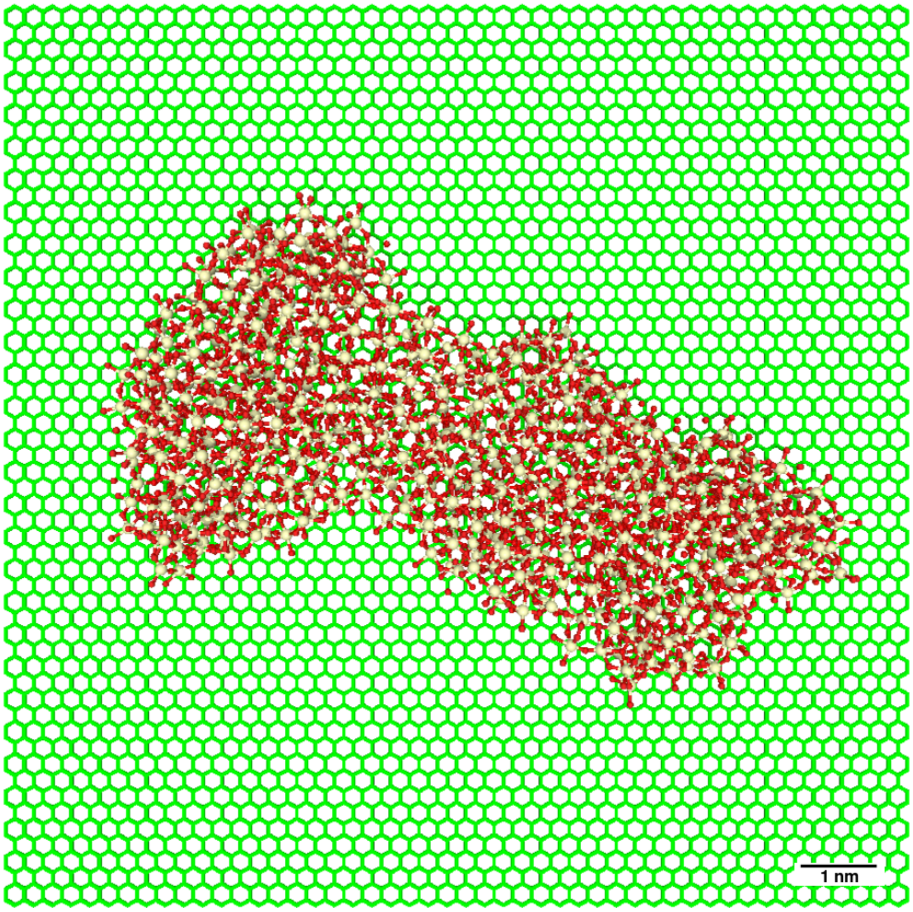

Figure 4.8 Coalescence product $[(WO_3)_3]_{200}$ obtained by merging two $[(WO_3)_3]_{100}$ nanostructures grown at 600 K and locally relaxed.

Although the product keeps the largely disordered character of the initial assemblies, a general orientation along the primitive symmetry axes of graphite can generally be noticed. The different crystal structures of HOPG and tungsten oxide contribute to keeping the assembly disordered through geometric frustration upon the growth process. The interaction with the surface is thus found to be sufficiently strong to drive the nanostructure toward preferential orientations.

4.4.4 Comparison of Theoretical Simulations to Experimental Results

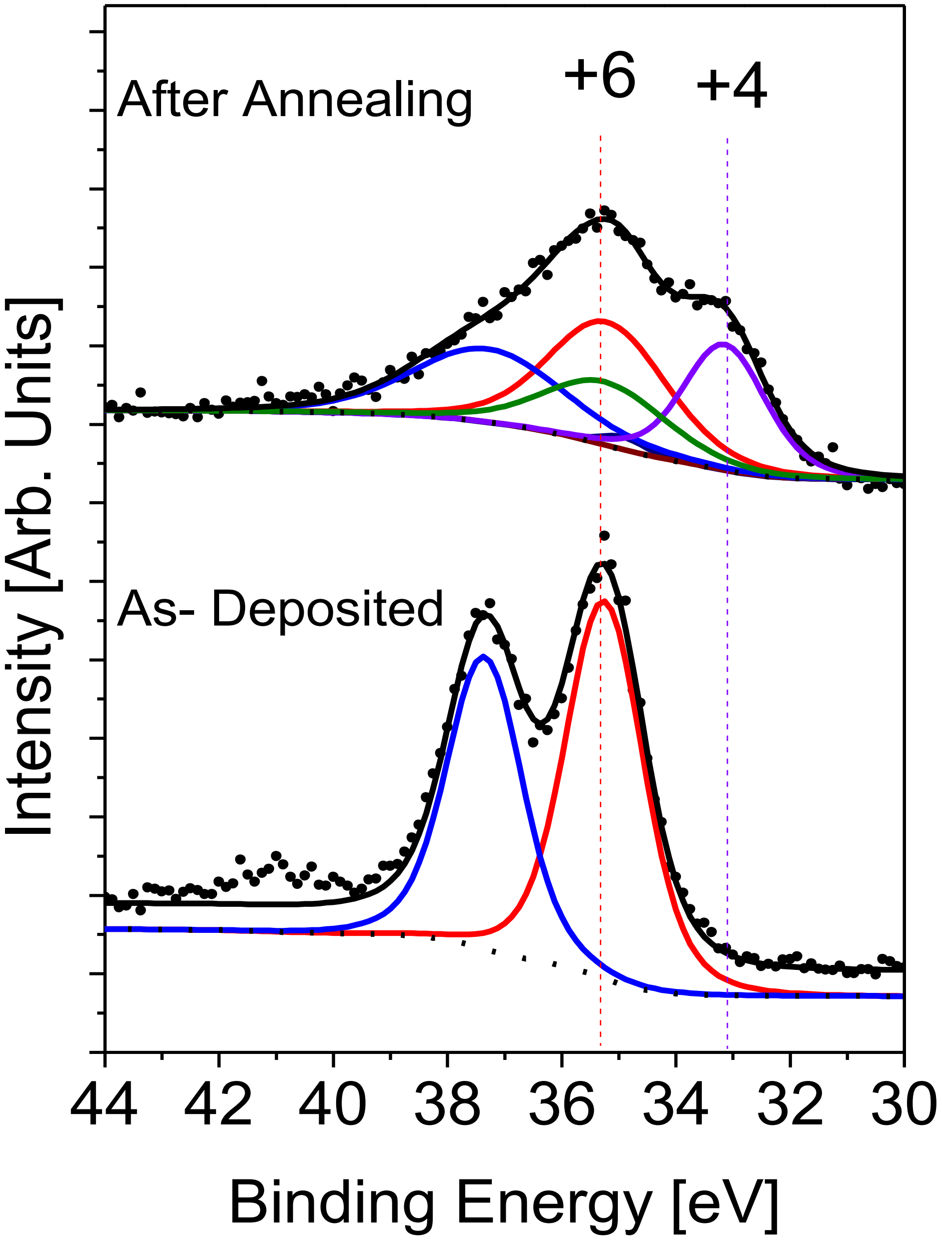

Figure 4.9 XPS Spectra of as-deposited $(WO_3)_3$ clusters and $(WO_3)_3$ clusters after annealing to 673 K

Our simulations correctly predict the small fractal-like structures for $(WO_3)_3$ clusters deposited on HOPG at 100 K. At low temperature, the diffusion of the clusters is suppressed. Both of the simulated and experimental results show ramified structures as a consequence of the diffusion limited aggregation process. However, the predicted annealing structures are inconsistent with the annealing structures observed via AFM. The simulated annealing structures have lost the ramification features during the annealing process while the structures observed via AFM still preserve that. It is evident from the AFM image that the sintering process of clusters are suppressed in this case, which could indicate that the interaction between the tungsten oxide clusters with the underlying graphite surface was underestimated in the present model.

For the structures resulting from deposition at 600 K, simulations show compact aggregates and the coalesced structures with certain orientation preference along the primitive symmetry axes of graphite. However, there is no evidence from our simulations for the formation of elongated crystalline nanowires, or to the contribution of the substrate as a driving force to such crystallization. The epitaxial growth of nanowire on HOPG surface usually depends on the step-edge preferred nucleation of nanoparticles or atoms.[17]Since the nanowire structures we observed are on terraces, this is unlikely to be case in our system. The other possibility is that there could be an interfacial reaction taking place at the $(WO_3)_3$/HOPG interface leading to a stronger interaction between $(WO_3)_3$ clusters and HOPG surface and consequently, an aligned growth of nanowires. It has been shown in other systems that metal oxides on carbonaceous support may form carbides under reactive conditions[18]. XPS investigation of $(WO_3)_3$ clusters on HOPG indicated the reductions of tungsten as shown from W(4f) peak before and after annealing. Therefore,

WO_3 may undergo reduction with the carbon support to form tungsten carbide. In this case, upon heating, $(WO_3)_3$ clusters will diffuse on HOPG, meanwhile reaction with carbon surface will help to immobilize the $(WO_3)_3$ clusters. It has been shown in the example of epitaxial growth of rare earth metal silicides on Si(110) surface that the formation of nanowires of metal silicides was observed due to an anisotropic lattice mismatch[19]. In this scenario, the nucleation sites on the two long edges of the nanowires are not energetically favored due to the high strain energy, which leads to an oriented growth along the long side. It is well known that the lattice mismatch between graphene and the underlying substrate can cause the graphene sheets to be periodically buckled due to the strain effect.[20] It is also suggested that metal clusters supported on graphene can be stabilized by the strain on the graphene layer.[21] Since the bulk WO_3 has a monoclinic symmetry which is very different from the underlying graphite, it is reasonable to assume that the lattice mismatch between WO_3 and graphite can exist. Although an interfacial layer between WO_3 and graphite may help to relieve some of the stress, a preferential growth along the graphite axes can still take place to induce the oriented growth of the nanowires. This growth mechanism will be more favorable at higher temperature, by providing a higher mobility of the $(WO_3)_3$ to navigate the surface to find the lowest energy sites.

As far as computational modeling is concerned, the present potential used in the MD simulations is not reactive and cannot account for carbide formation. Neither can it describe terraces or steps that are likely to play a role in anchoring the nanostructures and driving their one-dimensional growth. One additional limitation of the simulations is the much limited time and length scales with respect to experiment. Had the simulations been longer, higher degrees of crystallinity would likely have been obtained. Even given these limitations, our coalescence simulations predict elongated nanostructures with a width that is comparable to that measured for the nanowires, thereby suggesting that the nanowires could originate from clusters containing about 100 basic $(WO_3)_3$ units.

4.5 Conclusions

The assembling behaviors of $(WO_3)_3$ clusters on HOPG have been studied both experimentally and theoretically. Small fractal-like aggregates were observed for $(WO_3)_3$ clusters on HOPG at 100 K, which were also predicted by simulations. Directional growth of nanowires for $(WO_3)_3$ clusters on HOPG was observed at 600 K, differing more markedly from the more compact aggregates predicted by theory. Additional XPS spectra suggest that the strain between $(WO_3)_3$ clusters and the underlying carbon support are responsible for the oriental growth of nanowire and the immobilization of $(WO_3)_3$ clusters on HOPG through possible carbide formation. Despite its limitations especially regarding time and length scales, the computational approach manages to find preferential orientations for the elongated nanostructures with lateral dimension comparable to that measured on the nanowires, only based on the natural symmetries of the underlying HOPG substrate. The underestimation of the interaction between the clusters and the substrate in the present model thus appears to result mainly from its neglect of chemistry. In this respect, it would be valuable to extend this work to electronic structure calculations of the interaction of small tungsten oxide clusters on defective graphite substrates, especially near steps where nucleation is believed to occur.

Acknowledgments

This material is based upon work supported by the Air Force Office of Scientific Research (AFOSR) under Grant Number, FA9550-15-1-0259 (KHB).

References

(1) Poizot, P.; Laruelle, S.; Grugeon, S.; Dupont, L.; Tarascon, J. M. Nature 2000, 407, 496.

(2) Macht, J.; Iglesia, E. Phys Chem Chem Phys 2008, 10, 5331.

(3) Huang, X.; Zhai, H. J.; Kiran, B.; Wang, L. S. Angewandte Chemie-International Edition 2005, 44, 7251.

(4) Bondarchuk, O.; Huang, X.; Kim, J.; Kay, B. D.; Wang, L. S.; White, J. M.; Dohnalek, Z. Angewandte Chemie-International Edition 2006, 45, 4786.

(5) Kim, Y. K.; Rousseau, R.; Kay, B. D.; White, J. M.; Dohnalek, Z. J Am Chem Soc 2008, 130, 5059.

(6) Kim, J.; Kay, B. D.; Dohnalek, Z. J Phys Chem C 2010, 114, 17017.

(7) Pomp, S.; Kuhness, D.; Barcaro, G.; Sementa, L.; Mankad, V.; Fortunelli, A.; Sterrer, M.; Netzer, F. P.; Surnev, S. J Phys Chem C 2016, 120, 7629.

(8) Li, Z. J.; Zhang, Z. R.; Kim, Y. K.; Smith, R. S.; Netzer, F.; Kay, B. D.; Rousseau, R.; Dohnalek, Z. J Phys Chem C 2011, 115, 5773.

(9) Tang, X.; Bumueller, D.; Lim, A.; Schneider, J.; Heiz, U.; Gantefor, G.; Fairbrother, D. H.; Bowen, K. H. J Phys Chem C 2014, 118, 29278.

(10) Calvo, F.; Bowen, K.; Tang, X. The Journal of Physical Chemistry C 2014, 118, 1306.

(11) Ohno, K. Theoretica chimica acta 1964, 2, 219.

(12) Steele, W. A. Surf Sci 1973, 36, 317.

(13) González, B. S.; Hernández-Rojas, J.; Bretón, J.; Gomez Llorente, J. M. The Journal of Physical Chemistry C 2007, 111, 14862.

(14) Van Belle, D.; Froeyen, M.; Lippens, G.; Wodak, S. J. Molecular Physics 1992, 77, 239.

(15) Li, S.; Dixon, D. A. The Journal of Physical Chemistry A 2006, 110, 6231.

(16) Huang, X.; Zhai, H. J.; Kiran, B.; Wang, L. S. Angew Chem Int Ed Engl 2005, 44, 7251.

(17) Walter, E. C.; Zach, M. P.; Favier, F.; Murray, B. J.; Inazu, K.; Hemminger, J. C.; Penner, R. M. Chemphyschem 2003, 4, 131.

(18) Ma, J.; Zhu, S. G. Int J Refract Met H 2010, 28, 623.

(19) Chen, Y.; Ohlberg, D. A. A.; Williams, R. S. J Appl Phys 2002, 91, 3213.

(20) Loginova, E.; Nie, S.; Thurmer, K.; Bartelt, N. C.; McCarty, K. F. Phys Rev B 2009, 80.

(21) Zhou, M. A.; Zhang, A. H.; Dai, Z. X.; Feng, Y. P.; Zhang, C. J Phys Chem C 2010, 114, 16541.

5. Ion Induced Modification of Size-selected MoO_3 and WO_3 Clusters Deposited on HOPG

Xiang Li, Kevin A. Wepasnick, Xin Tang, Yi Wang, Kit H. Bowenb) and D. Howard Fairbrothera),b)

Departments of Chemistry and Materials Science, Johns Hopkins University, Baltimore, MD 21218

Gerd Gantefoer

Department of Physics, University of Konstanz, Universitätsstr. 10, 78457 Konstanz, Germany

Abstract

The effect of 4 keV Ar^+ ions on size-selected $(MoO_3)_n$ and $(WO_3)_n$ clusters, where n = 30±1, deposited on highly ordered pyrolytic graphite (HOPG) was studied by X-ray photoelectron spectroscopy (XPS) and atomic force microscopy (AFM). During deposition, both metal oxide clusters collected preferentially at step edges at low coverages, with larger cluster aggregates nucleating on the terraces at higher coverages. Under the influence of 4 keV Ar^+ ion bombardment, both clusters initially experienced oxygen loss and corresponding reduction of the transition metal before the remaining species were sputtered from the surface. However, MoO_3 was only partially reduced to MoO_2, while WO_3 was fully reduced to metallic tungsten. As a consequence of these variations in ion induced chemistry, changes in the surface morphology of MoO_3 and WO_3 following prolonged Ar^+ exposure differed significantly. For $(MoO_3)_{30\pm1}$, the size of the clusters decreased, due to removal of MoO_2 fragments. In contrast, for $(WO_3)_{30\pm1}$, the

formation of smaller sized clusters was also accompanied by the appearance of clusters that were much larger in size than the original “as deposited” clusters. The creation of these larger structures is ascribed to the mobility and coalescence of metallic tungsten species produced during the sputtering process. The contrast in the behavior of the molybdenum and tungsten oxide clusters illustrates the interplay that can exist between ion induced changes in speciation and morphology of deposited clusters.

5.1 Introductions

Transition metal oxide nanostructures have both technological and scientific significance due to their applications in the semiconductor industry and catalysis.[1] Nanosized clusters of transition metal oxides are especially interesting since they often exhibit novel electronic and magnetic properties compared to the corresponding bulk materials.[2,3] In addition to size, the properties of clusters are influenced by their shape and composition.[4,5] In most practical applications, clusters must be adsorbed onto solid surfaces.[6] However, although the properties of many clusters have been well studied in the gas phase, much less is known about the behavior of the corresponding surface bound clusters and how their composition and structure is modified by external stimuli, such as heat, light and charged particles.[7,8]

Ion bombardment is a widely used means to fabricate, [9] modify, [10] clean and analyze nanostructures.[11,12,13] For metal oxides, ion bombardment can directly remove material (physical sputtering) but also has the potential to change the chemical composition, metal oxidation state and valence band structure.[14,15,16,17] All of these transformations will affect both the chemical and physical properties of the nanostructures, independently or collectively. The effect of ion sputtering on thin films or bulk transition metal oxides has been extensively studied using a variety of different surface analytical techniques, e.g., X-ray photoelectron spectroscopy (XPS), Auger electron spectroscopy (AES), electron energy loss spectroscopy (EELS) and ultraviolet photoelectron spectroscopy (UPS). Many metal oxides (e.g., Nb_2O_5, MoO_3, Ta_2O_5) undergo reduction caused by preferential oxygen loss upon high-energy (~1-5 keV) ion bombardment, decreasing the metal's formal oxidation state and in some instances leading to the formation of metallic species.[18,19,20,21] In addition to better understanding the extent to which ion induced chemical transformations observed in bulk materials and thin films can be extrapolated to chemically analogous nanosized clusters, there is also a need to understand how the structure of deposited clusters (e.g. size, shape, aggregation state) change under the influence of ion bombardment. In this regard, structural transformations may arise as a result of the energy imparted to the surface during ion bombardment or as a consequence of differences in intrinsic reactivity and surface mobility of new species created as a consequence of ion bombardment. The study of such transformations is unique for deposited clusters since there is no analog for isolated gas phase clusters.

In a previous study,[22] we have demonstrated our ability to soft-land size-selected metal and metal oxide clusters on highly ordered pyrolytic graphite (HOPG) surfaces, and to control the coverage of deposited clusters by varying deposition time or beam current. In this paper, we have studied the effect of ion bombardment on size-selected molybdenum and tungsten trioxide (MoO_3 and WO_3) clusters. These two transition metal oxide clusters were chosen as prototypical examples of transition metal oxides due to their chemical similarity (being in the same periodic group) and also their importance in surface science and catalytic applications.[23,24,25] Previous experiments on bulk samples and thin films of these transition metal oxides have shown that ion bombardment of molybdenum trioxides and tungsten trioxides leads to the formation of substoichiometric oxides and a reduction of the metal's oxidation state. For molybdenum trioxides, ion induced effects are restricted to the reduction of MoO_3 to MoO_2, with no evidence of metallic species being formed by Ar^+ ions in the energy regime from 400 eV to 5 keV.[18,20,26] However, for tungsten trioxides, metallic tungsten has been observed after sputtering with 3 keV and 5 keV Ar^+ ions.[18,26]

In the present study, soft-landed, sized-selected metal oxide clusters were prepared on HOPG prior to ion bombardment. The use of size-selected clusters deposited on an atomically smooth surface (HOPG) meant that changes in the structure and morphology of deposited clusters could be accurately probed by atomic force microscopy (AFM). Furthermore, the size of the deposited clusters were smaller than the inelastic mean free path (IMFP) of the photoelectrons created in XPS, which allowed XPS data to be used to quantify changes in both the speciation and concentration of the surface bound clusters. The focus of our study was to compare and contrast the effects of ion bombardment on the two different metal oxide clusters, with a particular emphasis on the relationship between changes in speciation and surface morphology. It should be noted that although the transformations we observe are caused by ion bombardment, they may also include contributions from the backscattered ions/neutrals produced by the interactions of the primary beam with the HOPG substrate.

5.2 Experimental Methods

Molybdenum oxide and tungsten oxide cluster anions were produced using a magnetron sputter ion source which has been described in detail previously.[22] Once produced, the molybdenum oxide cluster anions were extracted from the source chamber and then accelerated to 1000 V, while tungsten oxide clusters were accelerated to 500 V (based on our experience, using smaller voltages makes it easier to mass select heavier clusters). Mass selected $(MoO_3)_{30\pm1}^-$, $(WO_3)_{30\pm1}^-$ or $(WO_3)_{19\pm1}^-$ cluster anions were produced by passing the ion beam through a magnetic sector mass spectrometer and then refocused and collimated by a series of ion optics, before reaching the deposition chamber where they were decelerated to kinetic energies of less than 0.1 eV per cluster and soft landed onto a freshly cleaved HOPG substrate. The target was at room temperature and the pressure during cluster deposition was typically $\sim 10^{-8}$ mbar.

Following cluster deposition, samples were removed from the deposition chamber and the coverage and chemical composition of the deposited clusters were determined using XPS in a PHI 5400 XPS system. [22] Peak positions in the spectra were referenced to the C(1s) graphite peak (284.5 eV) of the HOPG substrate, and metal oxidation states were fit using mixed Gaussian(30%)/Lorentzian(70%) envelopes. Deposited clusters were also modified in the PHI 5400 XPS system by ion bombardment using a PHI 04-303 sputtering ion gun operated at 4 keV beam voltage, 25 mA emission and 25 mPa pressure of Ar. Ion bombardment was alternated with in situ XPS acquisitions at 30 second intervals. The ion flux [6.16×10^{17} ions/(s·cm^2)] was calculated from the target current (converted to number of ions) measured on the sample during ion bombardment, divided by the sample's surface area (the sample surface is fully covered by the ion beam). The ion dose was determined by simply multiplying the ion flux by the exposure time.

To characterize the surface structure of clusters, ex situ AFM images (PicoSPM LE AFM (Agilent Technologies)) were acquired both as a function of increasing cluster coverage and as a function of argon ion dose. Samples were removed from the vacuum chamber after deposition and/or argon ion bombardment and adhered to an AFM sample plate using double-sided carbon tape. All image rendering and height measurements were performed with commercially available software from Agilent Technologies. Analysis by AFM revealed that the coverage of clusters on the edge of the HOPG sample was smaller than in the middle. Consequently, we used the optical microscope attached to the AFM to help position the tip in the middle of each sample prior to imaging. In principle, the AFM tips can also pick up or move loosely bound clusters. We verified that this effect was not playing a role in our studies by checking that the AFM images we acquired were identical when the same region of the sample was repeatedly imaged. In some instances this required us to adjust the scan speed.

5.3 Results And Discussion

5.3.1 Cluster Deposition

Figure 5.1 shows AFM images of $(MoO_3)_{30\pm1}$ and $(WO_3)_{30\pm1}$ clusters soft-landed onto HOPG substrates as a function of increasing cluster coverage (controlled by varying the ion dose). Both $(MoO_3)_{30\pm1}$ and $(WO_3)_{30\pm1}$ clusters behave similarly. At relatively low coverages, both $(MoO_3)_{30\pm1}$ [Figure 5.1(a)-1(c)] and $(WO_3)_{30\pm1}$ [Figure 5.1(d)-1(f)] clusters preferentially attach to step-edges. Such phenomenon has been observed in other systems (especially metal clusters[27], but also for metal oxide nanoparticles [28,29,30]) and is an indication of high cluster mobility and a lower nucleation barrier at step edges. This greater ease of nucleation at step edges is a because the step edges consist of carbon atoms with fewer coordination numbers, free radicals, alcohols, carbonyls, or carboxylic acids and are more likely to trap clusters than the carbon atoms on the terraces.[30] As the cluster coverage increases, the clusters saturate the step-edge adsorption sites and larger structures composed of cluster aggregates appear on the HOPG terraces, presumably as a result of favorable cluster-cluster interactions. As the coverage increases, further cluster aggregates continue to populate the terrace and Figure 5.1(c) and 1(f) show that the HOPG surface becomes saturated with adsorbed clusters in a loosely packed arrangement at high coverage.

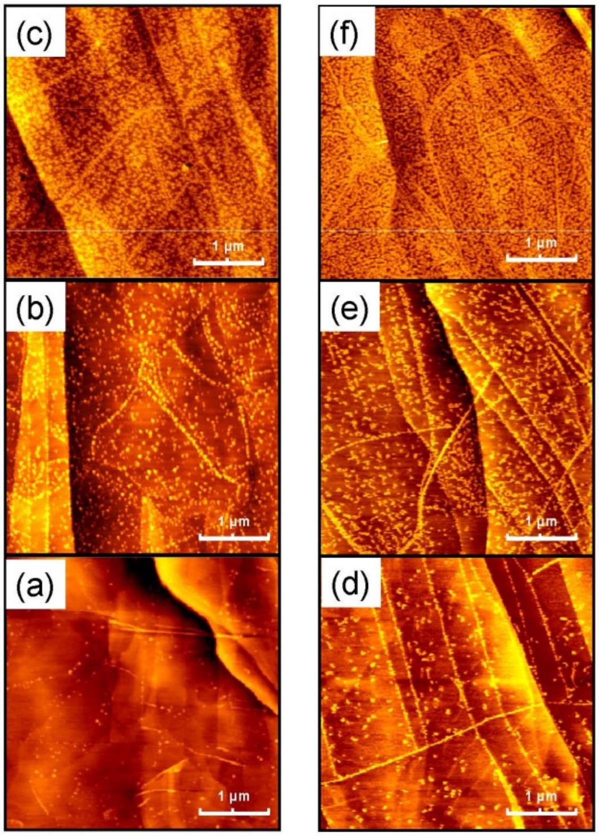

Figure 5.1 AFM images of $(MoO_3)_{30\pm1}$ [(a)-(c)] and $(WO_3)_{30\pm1}$ [(d)-(f)] clusters soft-landed on HOPG, shown as a function of increasing cluster coverage on moving from (a) to (c) and (d) to (f), respectively.

5.3.2 Effect of Ion Bombardment on Deposited Clusters

XPS was used to establish the effect of ion dose on the chemical composition, bonding and concentration of adsorbed $(MoO_3)_{30\pm1}$ and $(WO_3)_{30\pm1}$ clusters. In summary, the XPS data shown in Figure 5.2 reveals that ion bombardment transforms the oxide clusters in two largely sequential steps; ion induced reduction of the transition metal due to oxygen loss, followed by sputtering of the reduced species. The principle difference between molybdenum and tungsten oxide clusters is the extent of ion induced reduction that occurs prior to the onset of sputtering.

The initial coverage of $(MoO_3)_{30\pm1}$ and $(WO_3)_{30\pm1}$ clusters shown in the bottom XP spectra of Figure 5.2(a) and 2(b), correspond to the same cluster coverages as the AFM images of Figure 5.1(c) and 1(f), respectively. For $(MoO_3)_{30\pm1}$ clusters, the evolution of the Mo(3d) region under the influence of Ar^+ ion bombardment is shown in Figure 5.2(a). Prior to ion bombardment (ion dose=0), the spectral envelope contains two peaks, centered at 232.5 and 235.6 eV with an intensity ratio of 3:2 due to Mo($3d_{5/2}$) and Mo($3d_{3/2}$) transitions (Δ = 3.1 eV); the Mo($3d_{5/2}$) peak position is indicative of Mo atoms in a highly oxidized state, consistent with the formal +6 oxidation state of Mo in MoO_3. For comparatively small ion doses ($<1.0\text{x}10^{20}$ ions/cm^2), changes to the Mo(3d) envelope are dominated by a broadening of the overall spectral envelope to lower binding energies in the absence of any significant change in the integrated peak area. In this region, the spectral envelope can be reasonably well fit by a combination of fully oxidized MoO_3 clusters and two new Mo($3d_{5/2}$,$3d_{3/2}$) doublets associated with the production of Mo(V) and Mo(IV) species. To optimize the reliability of our spectral deconvolution, all of the Mo peak positions were based on literature XPS studies where single component molybdenum species (Mo, MoO_2 or MoO_3) were prepared and the Mo($3d_{5/2}$,$3d_{3/2}$) peak positions identified.[40] For an ion dose of $1.0x10^{21}$ ions/cm^2, Figure 5.2 shows that reduction of the parent MoO_3 cluster species to MoO_2 is essentially complete. For larger ion doses, a steady decrease in spectral intensity within the Mo(3d) region is observed while the shape of the spectral envelope itself remains unchanged. A comparison with the reference spectrum of a metallic Mo sample (shown in the uppermost left hand spectrum of Figure 5.2) confirms that ion induced reduction of $(MoO_3)_{30\pm1}$ is restricted to the conversion of Mo(VI) to Mo(IV).

The corresponding XP spectra showing the changes in the W(4f) region of $(WO_3)_{30\pm1}$ clusters adsorbed on HOPG as a function of Ar^+ ion dose are presented in Figure 5.2(b). Upon deposition (ion dose=0) the W(4f) spectral envelope can be well fit with two dominant peaks, centered at 35.9 and 38.0 eV and an intensity ratio of 4:3. The binding energy separation (2.1 eV) is consistent with the spin-orbit splitting between W($4f_{7/2}$) and W($4f_{5/2}$) transitions, while the W($4f_{7/2}$) peak position (35.9 eV) is indicative of tungsten atoms in a formal +6 oxidation state associated with the "as deposited" WO_3 clusters. A small contribution (~10.0 %) to the W(4f) envelope is ascribed the W($4f_{7/2,\ 5/2}$) doublet associated with W (+5) species, with a W($4f_{7/2}$) peak position at 34.9 eV. During the initial stages of argon ion bombardment (ion dose $\leq 2.6x10^{20}$ ions/cm^2), the W(4f) peak broadens to lower binding energies, analogous to the behavior of the Mo(3d) region for $(MoO_3)_{30\pm1}$ clusters. In this regime, the W(4f) spectral envelope can be fit to a combination of the W($4f_{7/2,5/2}$) doublet associated with the native W(VI) species along with two additional W($4f_{7/2,\ 5/2}$) doublets with W($4f_{7/2}$) peak positions at 34.7 and 33.3 eV that can be ascribed to W(V) and W(IV) species, respectively. However, for larger ion doses ($> 5.9x10^{20}$ ions/cm^2), and in contrast to the behavior of the Mo(3d) region for MoO_3 clusters, the W(4f) spectral envelope continues to broaden to lower binding energies. Spectral deconvolution of the W(4f) envelope in this regime reveals the appearance of a new W($4f_{7/2}$, $4f_{5/2}$) doublet with a W($4f_{7/2}$) peak position at 31.2 eV, whose presence indicates the formation of metallic tungsten. At even higher argon ion doses (> 1.0×10^{21} ions/cm^2), the metallic W peaks become the dominant features while the overall intensity in the W(4f) region decreases. A reference XP spectrum of a sputter cleaned metallic tungsten sample (shown in Figure 5.2(b)) confirms that ion induced reduction of WO_3 clusters produces metallic W(0). It should be noted that the effect of Ar^+ ion bombardment was also examined on smaller size $(WO_3)_{19\pm1}$ clusters (Molecular Weight = 4404), which have a nearly equal mass to $(MoO_3)_{30\pm1}$ (Molecular Weight = 4318).

The XP spectra in Figure 5.2 reveal that MoO_3 clusters were only partially reduced to MoO_2, while WO_3 clusters were reduced to metallic tungsten. This difference is consistent with previous studies on bulk and thin films of MoO_3 and WO_3, [18,20,26] indicating that the effects of ion bombardment are similar for deposited clusters. The different phenomena observed for MoO_3 vs, WO_3 upon sputtering is at least in part a reflection of the significant difference in the mass of argon (40 amu) and either oxygen (16 amu) or molybdenum (96 amu) atoms compared to the mass difference between argon (40 amu) and tungsten (184amu). These mass differences mean that the effective momentum transfer between incident argon ions and tungsten atoms will be much less efficient than that to either oxygen or molybdenum, facilitating WO_3reduction.[15] These effects and other phenomena which contribute to different ion induced effects on metal oxides can be found in previous papers. [31] Further ion bombardment caused MoO_2 and W to be sputtered from the surface. The sputtering process, which occurs for ion doses in excess of approximately 1.0×10^{21}

ions/cm^2, is evidenced by a systematic decrease in the signal intensities within the Mo(3d) and W(4f) regions (see Figure 5.2), while the spectral envelopes remain unchanged.

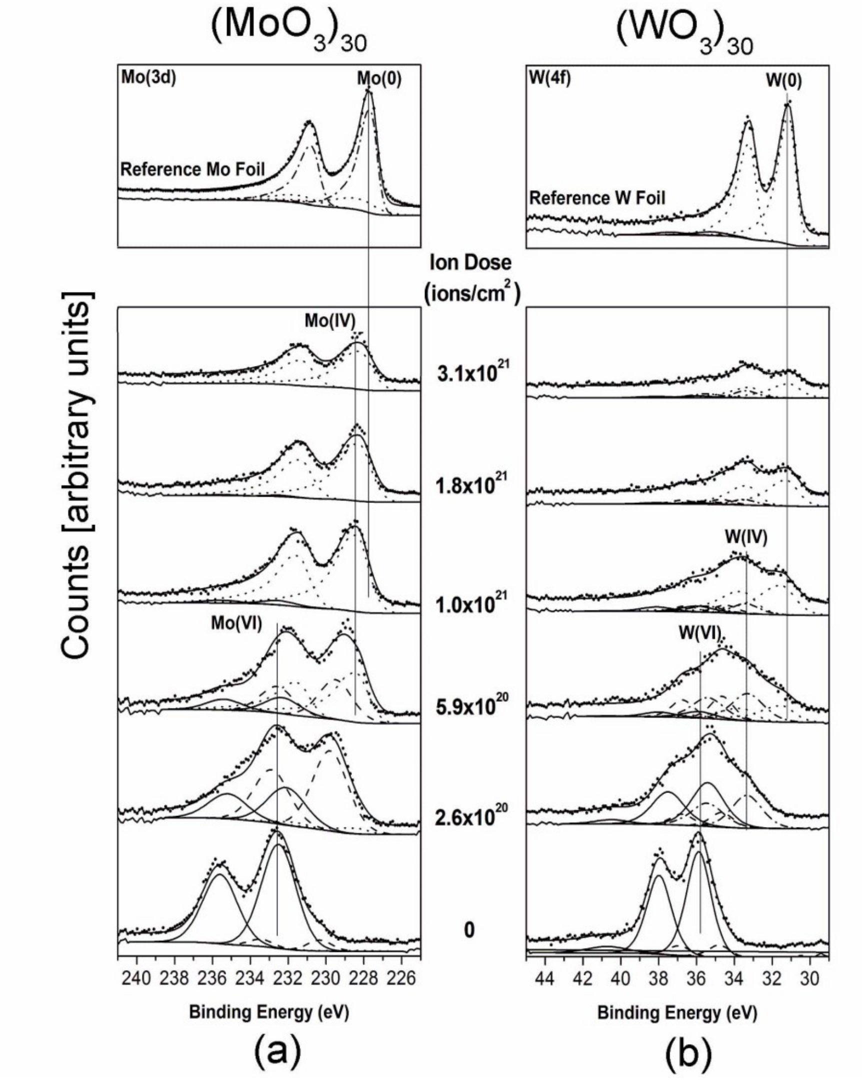

Figure 5.2 Effect of Ar$^+$ ion dose on (a) the Mo(3d) region of $(MoO_3)_{30\pm1}$ clusters and (b) the W(4f) region of $(WO_3)_{30\pm1}$ clusters, as shown by XPS. Reference XP spectra of sputter cleaned molybdenum and tungsten foils are also shown for comparison.

AFM images were used to determine how argon ion dose affected the structure, size and concentration of adsorbed clusters. By acquiring AFM images on samples which had been analyzed by XPS after ion bombardment we could investigate how the structure of the adsorbed clusters responds to the chemical transformations induced by ion bombardment.

Figure 5.3 shows AFM images illustrating the effect of Ar^+ ion bombardment on deposited $(MoO_3)_{30\pm1}$ [Figure 5.3(a)-(c)] and $(WO_3)_{30\pm1}$ [Figure 5.3(d)-(f)] clusters. For the “as deposited” $(MoO_3)_{30\pm1}$ clusters, Figure 5.3(a) shows that they are relatively uniformly deposited on the HOPG surface. After an ion dose of $1.0x10^{21}$ ion/cm^2 [Figure 5.3(b)], there is little obvious change in the shape of the adsorbed clusters, except perhaps for a slight reduction in the cluster coverage and size. Based on the corresponding XPS data this image corresponds to the ion dose required to induce complete reduction of MoO_3 to MoO_2, in the absence of any significant MoO_2 sputtering. Since any MoO_2 clusters produced in vacuum will re-oxidize upon air exposure [22] prior to AFM imaging, we would not expect to see any significant change in the structure of the clusters. This is consistent with the similarity in structure and cluster size observed between the “as deposited” and ion exposed MoO_3 clusters in Figures 3(a) and 3(b), respectively. After an ion dose of 1.8×10^{21} ion/cm^2 [Figure 5.3(c)], however, a significant decrease in the size of the remaining clusters occurred [note the difference in height scale for Figure 5.3(c)]. This is consistent with the onset of MoO_2 sputtering as observed for the same ion dose by XPS (Figure 5.2). For even larger ion doses AFM results showed that the vast majority of the clusters were removed from the surface, leaving behind a comparatively flat HOPG substrate.

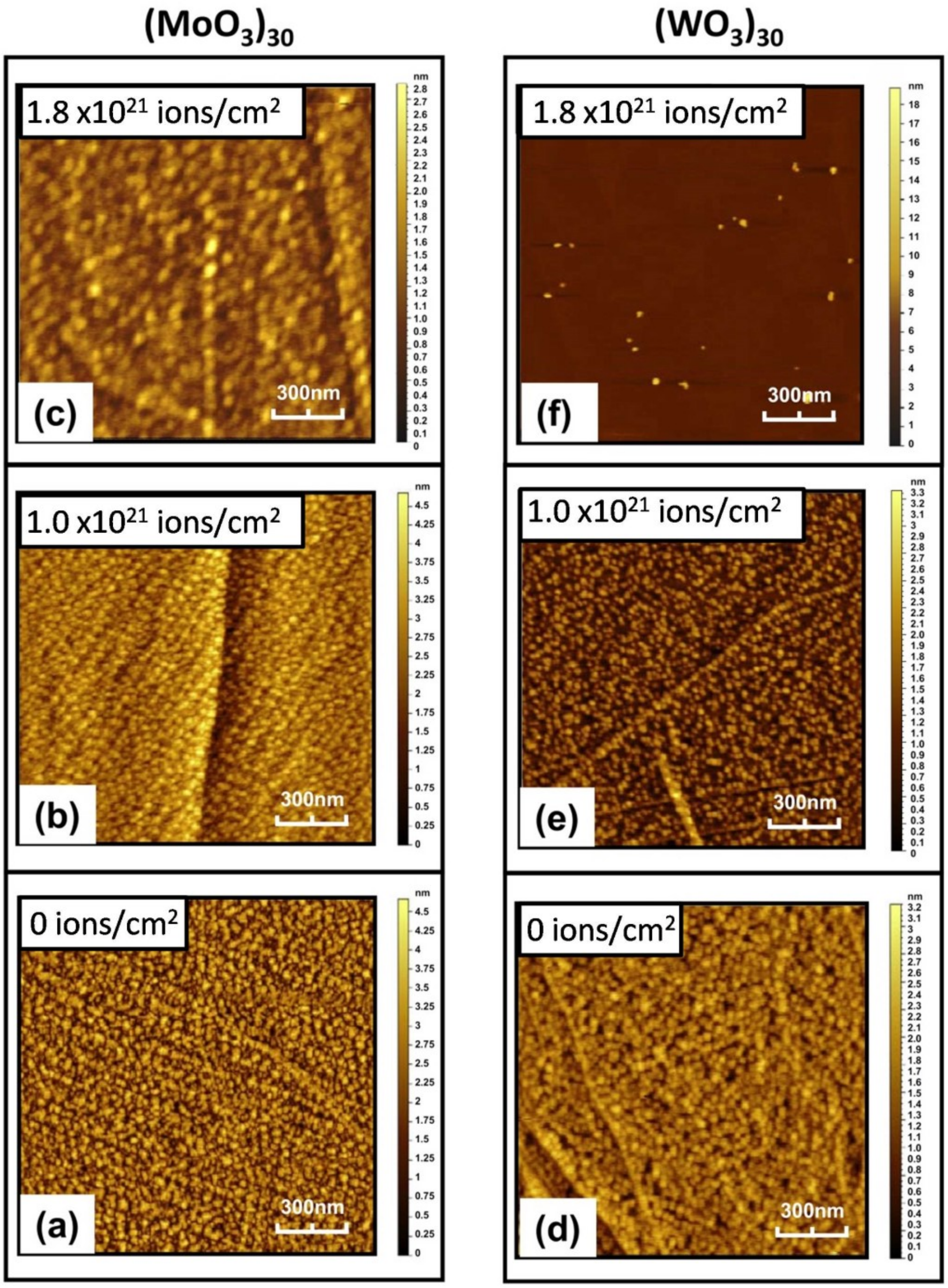

Figure 5.3 Effect of Ar$^+$ ion dose on the surface structure of deposited (MoO$_3$)$_{30\pm1}$ [(a)-(c)] and (WO$_3$)$_{30\pm1}$ [(d)-(f)] clusters, as shown by AFM.

Effect of Ar^+ ion dose on (a) the Mo(3d) region of $(MoO_3)_{30\pm1}$ clusters and (b) the W(4f) region of $(WO_3)_{30\pm1}$ clusters, as shown by XPS. Reference XP spectra of sputter cleaned molybdenum and tungsten foils are also shown for comparison.

For the $(WO_3)_{30\pm1}$ clusters, the initial structure prior to sputtering [Figure 5.3(d)] is similar to that observed for the $(MoO_3)_{30\pm1}$ clusters [Figure 5.3(a)]. After an argon ion dose of 1.0×10^{21} ion/cm^2 [Figure 5.3(e)] the two-dimensional coverage of tungsten clusters decreased and the underlying HOPG substrate is now clearly visible in places, consistent with the XPS data for the same ion dose which reveals that a large fraction of the WO_3 clusters have been fully reduced to metallic tungsten and the coverage of tungsten atoms has begun to decrease. However, as the ion dose was increased further to 1.8×10^{21} ion/cm^2 [Figure 5.3(f)], at a point where the XPS data in Figure 5.2 indicates that the prevalent change involves a loss of metallic tungsten atoms, a dramatic change in the structure of the tungsten clusters was observed by AFM. Specifically, a small number of extremely large structures had formed. This is perhaps most apparent in Figure 5.3(e)-3(f) by noting the change in height scale for the Figure 5.3(f). To check the validity of this phenomenon we conducted separate ion bombardment experiments on a different $(WO_3)_{30\pm1}$ sample and observed the same changes in the AFM images. It is also worth noting that numerous smaller clusters are also present after an ion dose of 1.8×10^{21} ion/cm^2, although they are not observed in the image because their presence is obscured by the increase in height scale needed to capture the large structures that had formed. A representative AFM image highlighting the presence of these smaller clusters is shown in Figure 5.4.

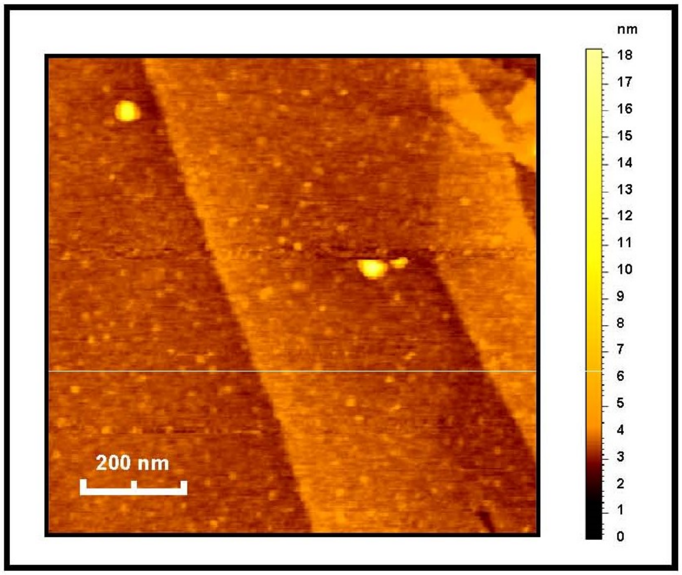

Figure 5.4 AFM image of sputtered $(WO_3)_{30}$ clusters (ion dose of 1.8x10^{21} ions/cm^2). It should be noted that to acquire these images the scan speed was decreased to reduce tip induced displacement of adsorbed clusters and help identify the presence of small clusters on the surface.

Figure 5.5 shows more quantitative information on the effect that Ar^+ ion bombardment has on cluster heights, obtained by (top) comparing AFM line scans taken through the clusters observed after an ion dose of 1.8x10^{21} ion/cm^2 and (bottom) comparing between the height distributions of the "as deposited" $(MoO_3)_{30\pm1}$ and $(WO_3)_{30\pm1}$ clusters to the height of the clusters observed after an argon ion dose of 1.8x10^{21} ion/cm^2. For the "as deposited" clusters, the average height and height distribution of both $(MoO_3)_{30\pm1}$ and $(WO_3)_{30\pm1}$ clusters was very similar; 1.9 ± 0.4 nm for $(MoO_3)_{30\pm1}$ and 1.9 ± 0.3 nm for $(WO_3)_{30\pm1}$ clusters. For the $(MoO_3)_{30\pm1}$ clusters exposed to an ion dose of 1.8x10^{21} ion/cm^2 the size of the remaining clusters decreased to 0.7±0.2 nm. This decrease in cluster size compared to the "as deposited" clusters can be ascribed to the onset of MoO_2 sputtering, in accord with the XPS data shown in Figure 5.3. In contrast, for the $(WO_3)_{30\pm1}$ clusters exposed to the same ion dose the size of the remaining clusters increased to 4.2 ± 1.4 nm.

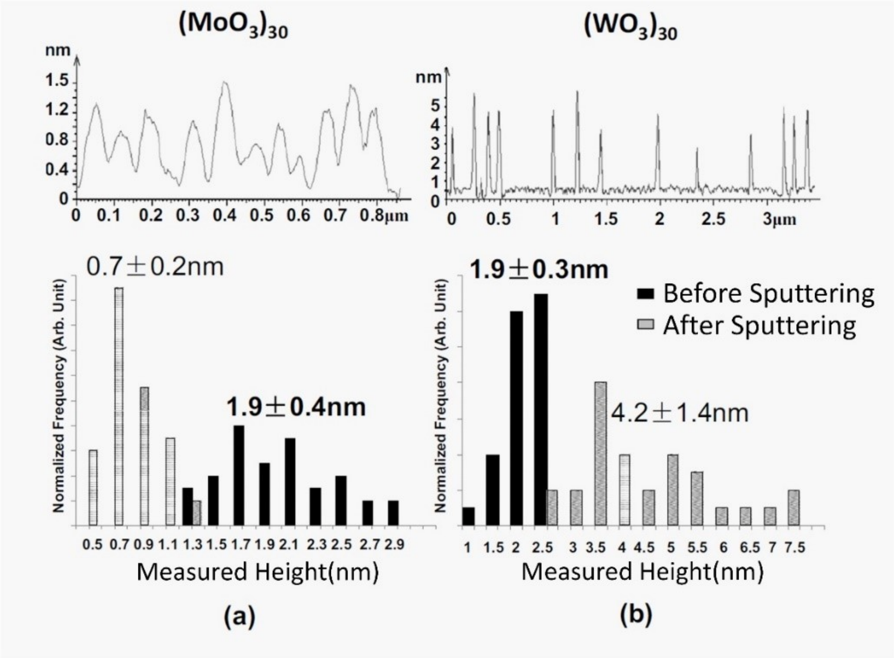

Figure 5.5 (Top) AFM line scans showing cluster heights after (a) $(MoO_3)_{30}$ and (b) $(WO_3)_{30}$ clusters were exposed to an argon ion dose of $1.8\text{x}10^{21}$ ions/cm^2. (Bottom) Comparison of the height distribution of "as deposited" (a) $(MoO_3)_{30}$ and (b) $(WO_3)_{30}$ clusters to those observed after an argon ion dose of $1.8\text{x}10^{21}$ ions/cm^2. For $(MoO_3)_{30\pm1}$ clusters, height distributions were based on measurements of 40 individual clusters before and after ion bombardment. For $(WO_3)_{30\pm1}$ clusters, 30 individual clusters were analyzed before and after ion bombardment.

We hypothesize that the appearance of a small number of much larger clusters compared to the "as deposited" oxide clusters is a consequence of the mobility and subsequent coalescence of small metallic tungsten clusters produced during WO_3 bombardment. This assertion is consistent with previous observations on the increased mobility of smaller clusters and metal vs. metal oxide clusters.[22] Ion bombardment could also help to initiate metal cluster coalescence by providing additional energy to the surface which would facilitate the diffusion and coalescence process. For metallic tungsten, evidence of such an effect has been observed in a previous study where ion bombardment transformed small bunches of tungsten nanowires into tungsten cones.[32] It should also be noted that we also observed many small (~0.7 nm in height) tungsten clusters after this ion dose (see Figure 5.4). These clusters could be pinned by defects created by the sputtering process, or be too large for cluster mobility. The idea that cluster size may be influencing the mobility and/or coalescence properties of the metallic tungsten clusters is also supported by the absence of large aggregates at lower ion doses, where XPS data revealed that metallic tungsten had already formed. The absence of significant coalescence phenomena during ion irradiation of MoO_3 is entirely consistent with the reduced mobility and propensity to coalesce expected for metal oxide clusters compared to metal clusters.

5.4 Summary and Conclusions

During the initial stages of bombardment, the ion induced reduction of MoO_3 clusters to MoO_2 produces little change in the structure or size of the adsorbed clusters. However, larger ion doses induce sputtering of MoO_2 and a decrease in the cluster size. For $(WO_3)_{30\pm1}$ clusters, the W(VI) atoms in WO_3 are completely reduced to W(0) by ion bombardment. We hypothesize that the mobility and coalescence of sufficiently small metallic tungsten clusters formed during ion bombardment leads to the appearance of a small concentration of new larger sized clusters. Thus, although molybdenum and tungsten are in the same group in the periodic table, ion bombardment produces very different changes in their composition and surface morphology. In a broader sense, this study also demonstrates the important interplay that can exist between the ion induced chemical modification and structure of adsorbed clusters.[22]

Acknowledgments

This work was supported by the Division of Materials Science and Engineering, Basic Energy Sciences, U.S. Department of Energy, under Grant No. DE-FG02-09ER46558. The authors also thank the Materials Sciences Surface Analysis Laboratory of Johns Hopkins University(JHU). K.A.W. also acknowledges the JHU Department of Chemistry for the award of a Rudolf Sonneborn Fellowship.

References

(1) C. N. R. Rao and B. Raveau, Transition metal oxides : structure, properties, and synthesis of ceramic oxides, 2nd ed. (Wiley-VCH, New York, 1998).

(2) X. Huang, H. J. Zhai, B. Kiran, and L. S. Wang, Angewandte Chemie-International Edition 2005, 44, 7251.

(3) N. O. Jones, S. N. Khanna, T. Baruah, M. R. Pederson, W. J. Zheng, J. M. Nilles, and K. H. Bowen, Physical Review B 2004,70, 134422.

(4) C. C. Jarrold, D. W. Rothgeb, E. Hossain, and J. E. Mann, Journal of Chemical Physics 2010, 132, 064302.

(5) D. W. Rothgeb, S. E. Waller, and C. C. Jarrold, The Journal of Physical Chemistry A 2010, 114, 11312.

(6) A. W. Castleman, S. A. Claridge, S. N. Khanna, C. B. Murray, A. Sen, and P. S. Weiss, Acs Nano 2009, 3, 244.

(7) P. Jensen, Reviews of Modern Physics 1999, 71, 1695.

(8) V. N. Popok, I. Barke, E. E. B. Campbell, and K.-H. Meiwes-Broer, Surface Science Reports 2011, 66, 347.

(9) I. P. Jain and G. Agarwal, Surface Science Reports 2011, 66, 77.

(10) E. Taglauer, Applied Surface Science 1982, 13, 80.

(11) J. P. Coad and Cunningh.Jg, J. Electron Spectrosc. Relat. Phenom. 1974, 3, 435.

(12) D. J. Ball, T. M. Buck, G. H. Wheatley, and D. Macnair, Surf. Sci. 1972, 30, 69.

(13) A. Benninghoven, Surf. Sci. 1973, 35, 427.

(14) S. Storp and R. Holm, J. Electron Spectrosc. Relat. Phenom. 1979,16, 183.

(15) R. Kelly, Mater. Sci. Eng. A 1989, 115, 11.

(16) R. Kelly, Nucl. Instrum. Methods 1981, 182, 351.

(17) V. S. Smentkowski, Prog. Surf. Sci. 2000, 64, 1.

(18) T. J. Driscoll, L. D. Mccormick, and W. C. Lederer, Surf. Sci. 1987, 187, 539.

(19) D. R. Baer, M. H. Engelhard, A. S. Lea, P. Nachimuthu, T. C. Droubay, J. Kim, B. Lee, C. Mathews, R. L. Opila, L. V. Saraf, W. F. Stickle, R. M. Wallace, and B. S. Wright, J. Vac. Sci. Technol. A 2010, 28, 1060.

(20) K. S. Kim, W. E. Baitinger, J. W. Amy, and N. Winograd, J. Electron Spectrosc. Relat. Phenom. 1974, 5, 351.

(21) M. A. Langell, Surf. Sci. Rep. 1987, 186, 323.

(22) K. A. Wepasnick, X. Li, T. Mangler, S. Noessner, C. Wolke, M. Grossmann, G. Gantefoer, D. H. Fairbrother, and K. H. Bowen, J. Phys. Chem. C 2011, 115, 12299.

(23) A. Katrib, P. Leflaive, L. Hilaire, and G. Maire, Catalysis Letters 1996,38, 95.

(24) C. MartIn, G. Solana, P. Malet, and V. Rives, Catalysis Today 2003,78, 365.

(25) D. G. Barton, M. Shtein, R. D. Wilson, S. L. Soled, and E. Iglesia, The Journal of Physical Chemistry B 1999, 103, 630.

(26) N. V. Alov, D. M. Kutsko, and K. V. Bordo, J Surf Investig-X-Ray Synchro 2008, 2, 184.

(27) G. M. Francis, L. Kuipers, J. R. A. Cleaver, and R. E. Palmer, Journal of Applied Physics 1996, 79, 2942.

(28) M. P. Zach, K. H. Ng, and R. M. Penner, Science 2000, 290, 2120.

(29) B. J. Murray, Q. Li, J. T. Newberg, J. C. Hemminger, and R. M. Penner, Chemistry of Materials 2005, 17, 6611.

(30) J. Taing, M. H. Cheng, and J. C. Hemminger, Acs Nano 2011, 5, 6325.

(31) D. F. Mitchell, G. I. Sproule, and M. J. Graham, Surface and Interface Analysis 1990, 15, 487.

(32) F. Y. Xie, L. Gong, X. Liu, J. Chen, W. G. Xie, and W. H. Zhang, Appl. Surf. Sci. 2009, 256, 693.

6. Catalytic Dehydration of 2-Propanol by Size-Selected $(WO_3)_n$ and $(MoO_3)_n$ Metal Oxide Clusters

Xin Tang,[1] Dennis Bumueller,[2] Alane Lim,[1] John Schneider,[2]

Ulrich Heiz,[3]

Gerd Ganteför,[2] D. Howard Fairbrother,[1] Kit H. Bowen[1]

[1]Department of Chemistry, Johns Hopkins University, Baltimore, Maryland 21218, USA

[2]Department of Physics, University of Konstanz, 78457 Konstanz, Germany

[3]Department of Chemistry – Catalysis Research Center, Technische Universität München, 85748 Garching, Germany

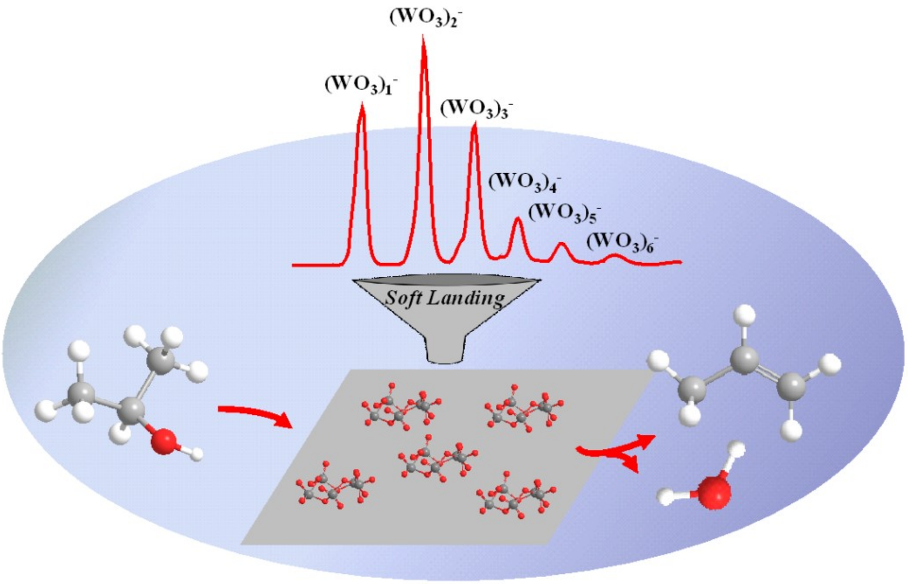

Abstract

Here, we report the catalytic dehydration of 2-propanol by metal oxide clusters, $(WO_3)_n$ and $(MoO_3)_n$ (n = 1, 2, 3, 5, 30), prepared by mass selecting and soft-landing metal oxide cluster anions created in the gas phase. Temperature programmed reaction (TPR) was used to characterize the catalytic activity of the deposited clusters by measuring the production of propene from 2-propanol. The nature of the support, the thermal history, size of the cluster and cluster composition were all found to play important roles in influencing catalytic activity. $(WO_3)_3$ clusters deposited on HOPG (Highly Ordered Pyrolytic Graphite) and oxide supports exhibited catalytic activity, although $(WO_3)_1$ monomers deposited on HOPG did not catalyze 2-propanol dehydration effectively, an effect ascribed to their coalescence into large aggregates on HOPG. For tungsten oxide clusters deposited on annealed oxide films, catalytic activity was observed for all cluster sizes and was linearly correlated with the size of the deposited clusters. Two different mechanisms, linear-scaling of active sites and cluster ripening, could account for this linear dependence. However, even on oxide supports, deposited tungsten oxide clusters lost catalytic activity after annealing to 400 °C. The effect is consistent with the loss of dioxo groups rather than any cluster aggregation. Compared to tungsten oxide clusters, molybdenum oxide clusters exhibited little or no catalytic activity toward the dehydration of 2-propanol, rationalized by the decrease in Lewis acidity of molybdenum – oxygen bonds.

6.1 Introduction

Clusters are assemblies of atoms and molecules with sizes ranging from sub-nanometer to a few nanometers. Because the size of clusters falls into the non-scalable region, many of their properties, i.e. electron structures, geometric structures, magnetic properties etc., are strongly dependent on their size.[1,2] As catalysts, clusters also exhibit size dependent catalytic properties. For example, Au_n clusters deposited on magnesia thin films were found to induce CO oxidation starting at $n = 8$.[3,4] Likewise, studies of Pd_n clusters deposited on $TiO_2(110)$ were found to show strong size effects during CO oxidation.[5] The correlation between the cluster size and catalytic activity suggests a novel way for tuning catalytic activities, i.e., by selecting specific cluster sizes.

To generate size-selected cluster catalysts, mass spectrometric methods such as quadruple mass spectrometry,[5-8] time of flight (TOF),[9,10] and magnetic sector mass spectrometry[11,12] have been used to mass-select cluster ions, followed by soft-landing them onto supports. For heterogeneous catalysis studies, these mass-selected clusters have several advantages over those synthesized by other methods. Compared to nanoclusters synthesized by solution[13] or sol-gel methods,[14] soft-landed, mass-selected clusters are free of stabilizers, such as ligands and surfactants that could complicate or even block catalytic active sites. Compared to methods such as physical vapor deposition (PVD)[15,16] or chemical vapor deposition (CVD),[17] mass-selected cluster deposition allows for "atom by atom" control of cluster size and composition, critical to the ability to tune the catalytic activity of many cluster catalysts. Additionally, when the number of atoms in mass-selected clusters is relatively small, high-level quantum calculations can be applied to elucidate their structure in the presence or absence of underlying supports.[4,18]

Consequently, the examination of catalytically active sites, e.g., steps, and their corresponding electronic properties may also be computationally tractable.

In contrast to studies on size-selected metal cluster catalysts, there is a relative paucity of information on the properties of metal oxide clusters. Examples include studies of the structures of vanadium oxide clusters on rutile $TiO_2(110)$ surfaces[19] and investigations on the stabilities of cobalt oxide clusters on diamond and alumina supports.[20] In addition, our group has studied the structure of molybdenum oxide[12,21], tungsten oxide,[21] and titanium oxide clusters[22] formed from size selected clusters deposited on HOPG (Highly Ordered Pyrolytic Graphite) surfaces. Other researchers have used PVD to deposit small tungsten oxide and molybdenum oxide clusters (predominantly trimers) onto $TiO_2(110)$ and other supports and studied their catalytic dehydration, dehydrogenation and condensation properties.[23-27] Systematic, size-dependent cluster catalyst studies, however, are not possible with thermal methods of evaporation. In related gas phase studies, the reaction products formed by collisions between small, mass-selected molybdenum sub-oxide cluster anions and water molecules were shown to be dependent on the number of molybdenum atoms in the cluster.[28] Gas-phase, metal oxide cluster anions have also been studied via anion photoelectron spectroscopy, and several of these have also been investigated theoretically.[29-32] Together, anion photoelectron spectroscopy and theory can uncover both the electronic and the geometric structure of clusters as a function of their sizes and composition. This is important because both reactivity and catalytic activity depend strongly on electronic and geometrical structure.[33,34] Moreover, previous studies have shown that the ultimate structure of deposited clusters, including the propensity for cluster aggregation and site-specific nucleation are regulated by cluster size, composition, deposition rate and the nature of the support.[11,12,22,35,36] All of these variables will play a role in determining both the electronic and geometrical structure of the deposited clusters with likely impacts on the reactivity and catalytic activity of the clusters. The present study explores the catalytic dehydration of 2-propanol using mass-selected $(MoO_3)_n$ and $(WO_3)_n$ clusters deposited on two different substrates, HOPG and an annealed metal oxide. This catalytic activity was studied using temperature programmed reaction (TPR) to probe the formation of propene from 2-propanol.

6.2 Experimental Methods

In this work, metal oxide clusters were produced as anions by a magnetron source. After mass selection and deceleration, they were then deposited (soft-landed) onto a substrate in an Ultra-High Vacuum (UHV) environment (1×10^{-9} Torr). In the magnetron source, a metal target was placed in a magnetic field and biased to -500 V, where a mixture of argon, helium and oxygen gases was also present. The argon gas was ionized to create argon cations, which in turn sputtered the metal target to produce metal atoms and electrons. Upon reaction with oxygen to form oxides, these metal oxides aggregated, attached electrons, and formed metal oxide cluster anions. The added helium served to cool and transport the cluster anions downstream, where they were accelerated before entering a magnetic sector mass spectrometer (25° sector magnet with resolution of $m/\Delta m = 20$). By tuning the magnetic field strength, $(WO_3)_n^-$ (n = 1, 2, 3, 5, 30) and $(MoO_3)_n^-$ (n = 1, 2, 3, 5, 30) cluster anions were mass-selected and focused by ion optics before entering the deposition chamber, where they were soft-landed (kinetic energy < 0.1eV/atom) onto a freshly peeled HOPG surface. The sample was cooled to approximately -160 ^{o}C by liquid nitrogen (LN_2) during cluster deposition and could be heated by passing current through a tantalum plate mounted behind and attached to the sample (i.e., resistive heating). The temperature of the sample was monitored by a K-type thermocouple attached to the back of the sample holder. Upon deposition, clusters are presumed to lose their excess charge to the conductive surface and to become neutral clusters. The number of clusters deposited on surface is calculated by integrating the cluster current over the deposition time. By assuming a cluster sticking coefficient of unity, a monolayer of (WO_3) will require 2.6×10^{14} clusters for the case of $(WO_3)_1$ monomer. Details of the source and deposition chamber can be found in references [12] and [21], and a schematic is provided as Figure 6.S1 in the supporting information.

Once clusters had been deposited onto the HOPG substrate, a TPR setup, using a Hiden HAL/3F PIC quadruple mass spectrometer (QMS), was used to characterize their catalytic activity. After cluster deposition, the sample temperature was increased to 25 ºC, at which point 2-propanol was adsorbed. This allowed for the chemisorption of 2-propanol onto oxides instead of the formation of physisorbed 2-propanol at low temperatures.[24] The 2-propanol was purified by several freeze-pump-thaw cycles before being background dosed through a UHV compatible leak valve. Unless noted, 0.2 L propanol was dosed (2×10^{-9} Torr for 100 s). Once the 2-propanol had been adsorbed, the sample was cooled to -50 ºC and then heated to 400 ºC with a temperature ramping rate of 2 ºC/s. The sample was cooled after 2-propanol adsorption to ensure a flat baseline by starting the temperature ramp well below the 2-propanol desorption temperature. The reaction products desorbed from the surface during the temperature ramp were detected and identified by the QMS, which was positioned normal to the plane of the substrate and at a distance of 5 mm. To minimize the contribution from background gases and maximize the sensitivity towards species desorbing directly from the substrate, the QMS ionizer was surrounded by a custom built glass shroud. Thus, in a typical experimental run, both 2-propanol and the mass-selected metal oxide cluster anions were co-deposited onto a substrate in a sequential fashion, which was then subsequently heated. Samples could also be transferred to an adjacent UHV chamber, where they were characterized by X-ray Photoelectron Spectroscopy (in situ XPS) with non-monochromatic Mg Kα-rays (1253.6 eV), and analyzed with a high energy electron analyzer. The structures of the deposited clusters were also characterized ex-situ by Atomic Force Microscopy (AFM). AFM images were acquired using a PicoSPM LE AFM (Agilent Technologies) operated in magnetic tapping mode using Co-Cr tips obtained from MikroMasch (NSC18). In principle, AFM tips could pick up and/or move loosely bound clusters adsorbed onto a surface. This potential issue was addressed by verifying that the AFM images remained unchanged after the same region was repeatedly imaged.

6.3 Results

6.3.1 Mass Spectra and XPS Characterization of Metal Oxide Clusters

Figure 6.1 shows the mass spectra of both the tungsten oxide (a) and molybdenum oxide (b) cluster anions used in this work. Both mass spectra show individually well-resolved peaks for the smaller ($n \leq 10$) metal oxide cluster sizes. Therefore, by appropriately tuning the mass filter we can size-select different clusters for deposition. Once deposited, the chemical composition of these clusters was characterized by in situ XPS as shown in Figure 6.2. For the tungsten oxide clusters shown in Figure 6.2(a), the XP spectral envelope in the W (4f) region shows two peaks, i.e., W $4f_{5/2}$ and W $4f_{7/2}$, with their peak positions centered at 37.7 eV and 35.6 eV, respectively. The binding energy of W $4f_{7/2}$ indicates that W is in its highest oxidation state, i.e., VI. [21,37] Meanwhile, the XP spectral envelope in the Mo (3d) region in Figure 6.2(b) also shows a doublet, i.e., Mo $3d_{3/2}$ and Mo $3d_{5/2}$, with peak positions centered at 235.6 eV and 232.5 eV, respectively. The binding energy of the Mo $3d_{5/2}$ peak confirms that molybdenum atoms are also in their highest (VI) oxidation state.[21,38]

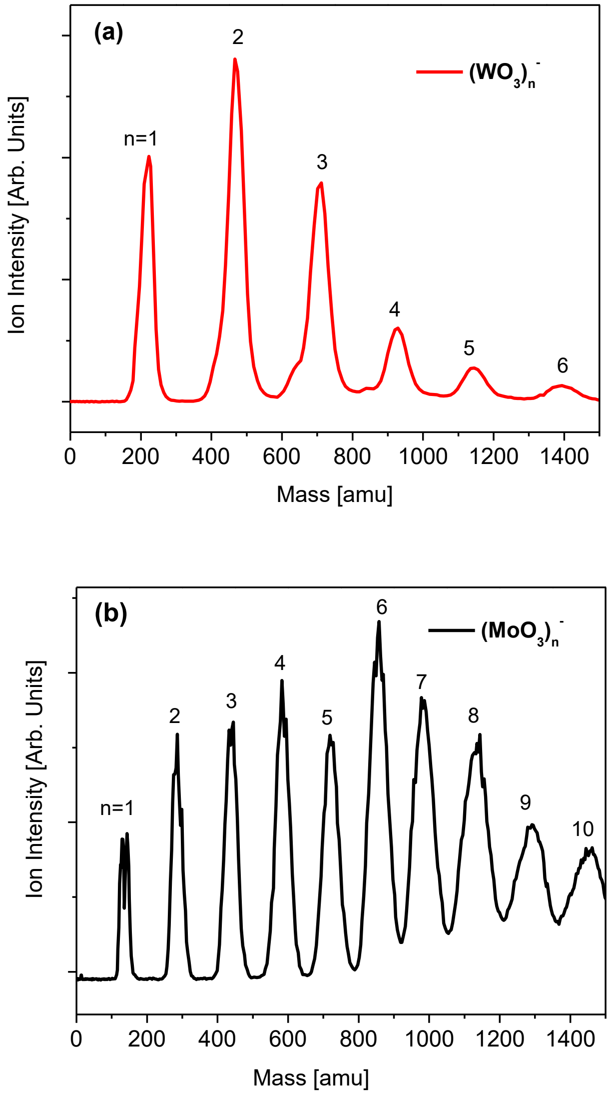

Figure 6.1 Mass spectra of (a) $(WO_3)_n$ and (b) $(MoO_3)_n$ cluster anions

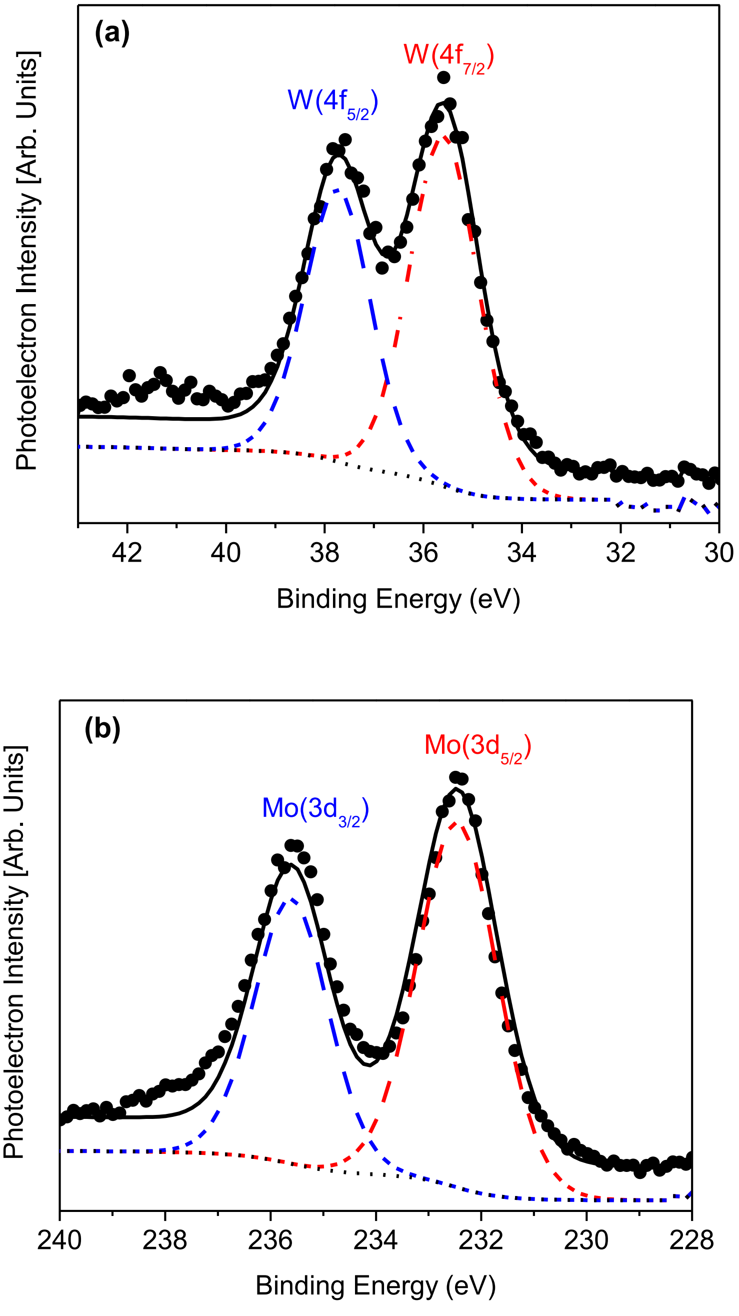

Figure 6.2 In situ XPS envelopes of (a) W(4f) region for $(WO_3)_n$ clusters and (b) Mo(3d) region for $(MoO_3)_n$ clusters deposited on HOPG

6.3.2TPR of 2-propanol on $(WO_3)_n$ Clusters

Figure 6.3(a) and 3(b) show the TPR traces of 0.2 L 2-propanol adsorbed on HOPG both without and with deposited $(WO_3)_3$ clusters, respectively. In the absence of $(WO_3)_3$ clusters, Figure 6.3(a) shows that the main desorption products detected by the QMS were 2-propanol's fragmentation products at m/z = 45, 41, and 43 amu, consistent with measurements of gas phase 2-propanol. Since all three species originate from desorbed 2-propanol, they exhibit coincident desorption profiles. However, when $(WO_3)_3$ clusters were deposited onto the HOPG surface, Figure 6.3(b) reveals that a new, higher temperature, peak appears at m/z = 41 amu in the absence of any corresponding peaks at m/z = 45 amu and m/z = 43 amu. Since the peak at m/z = 41 amu is the major fragmentation peak for propene, we assign this peak to the production of propene as a result of reactions between 2-propanol and the deposited $(WO_3)_3$ clusters (Other major propene fragmentation products at m/z = 39, 42, 27, 40 amu were also observed, verifying this assignment). Once the contribution to the m/z = 41 amu trace from 2-propanol desorption at lower temperatures was subtracted, a symmetric propene desorption profile is observed (see Figure 6.3(d)). Examples of this deconvolution procedure are shown in the supporting information (Figure 6.S2). The desorption temperature of propene is about 190 °C, higher than the propene desorption temperature (127 °C) observed in previous studies when 2-propanol reacts with $(WO_3)_3$ clusters deposited on $TiO_2(110)$.[23] Since a different temperature ramp rate (1.8 °C/s) was used in the two studies, a Redhead analysis[39] was necessary to compare the desorption energy of propene. Assuming a frequency factor $\nu_1 = 10^{13}$ s^{-1}, the calculated desorption energies of propene from $(WO_3)_3$ clusters adsorbed on

HOPG and $TiO_2(110)$ are 29.2 and 25.2 kcal/mol, respectively, close to the predicted value (26–28 kcal/mol) for propene formation from 2-propanol on $(WO_3)_3$ clusters.[23]

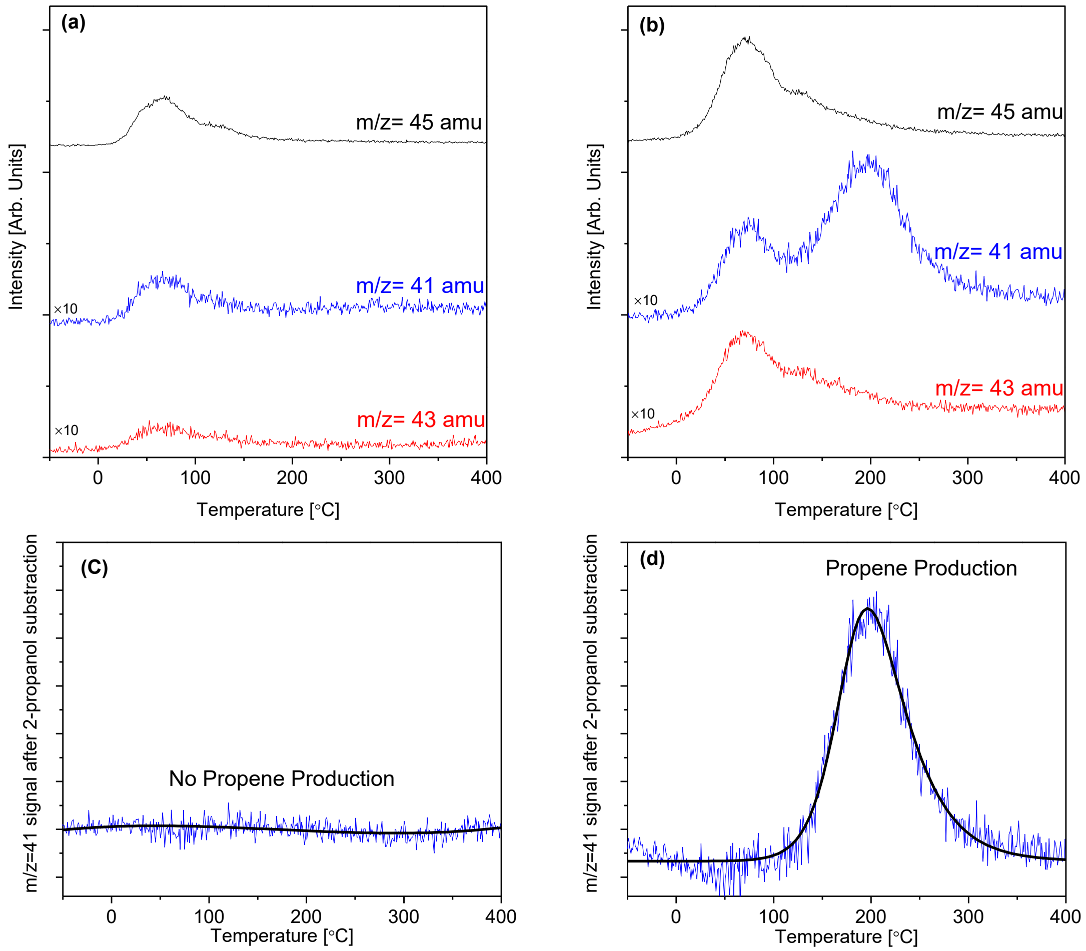

Figure 6.3 TPR trace of 2-propanol on HOPG (a) without deposited $(WO_3)_3$ clusters and (b) with deposited $(WO_3)_3$ clusters. m/z = 41 amu signal after subtraction of the 2-propanol contribution for HOPG (c) without deposited $(WO_3)_3$ clusters and (d) with deposited $(WO_3)_3$ clusters

Figure 6.4 displays TPR traces for propene production as a function of the total number of $(WO_3)_3$ clusters deposited on HOPG, each sample having been dosed with 0.2 L of 2-propanol. As the number of clusters increased, the propene desorption temperature remained almost constant at around 190 (± 5) °C although the propene peak area increased. Moreover, analysis of the propene peak area plotted as a function of the number of $(WO_3)_3$ clusters deposited reveals a linear correlation between the total number of clusters deposited and the propene yield (see inserted figure in Figure 6.4).

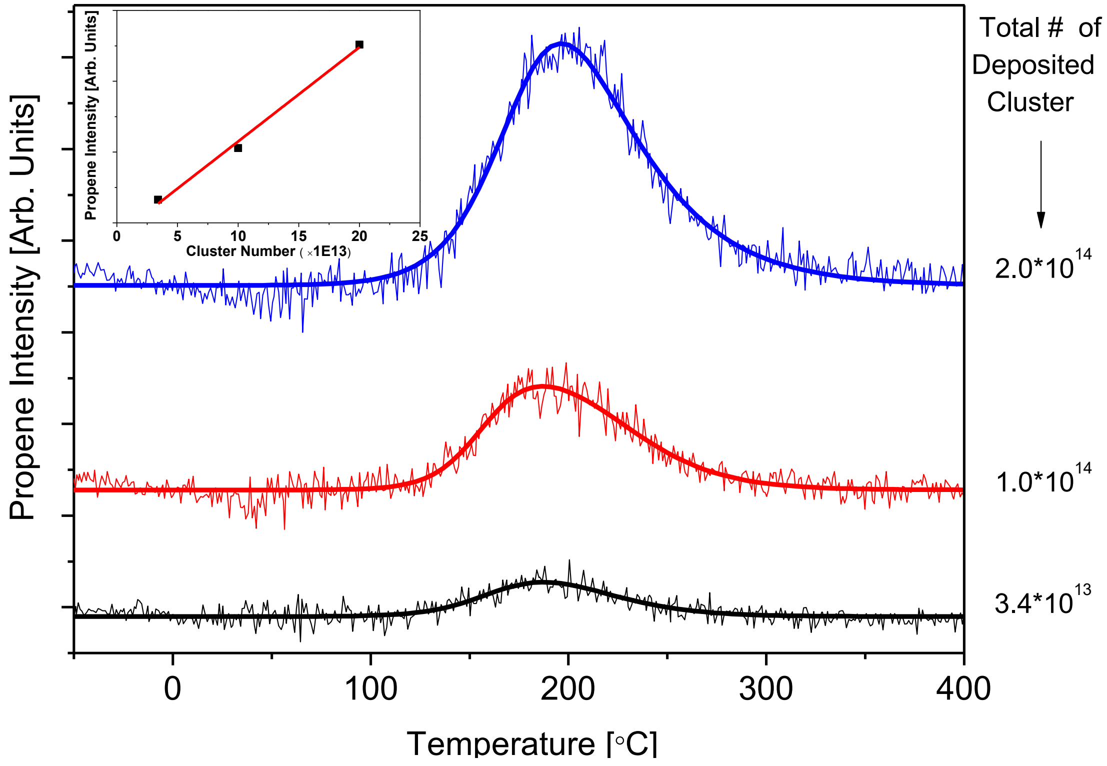

Figure 6.4 TPR traces of propene production vs. the number of $(WO_3)_3$ clusters deposited on HOPG. Insert shows a linear fitting between the propene yield vs. the number of $(WO_3)_3$ clusters deposited on HOPG

Figure 6.s 5(a) and 5(b) show TPR traces of propene production for $(WO_3)_3$ clusters adsorbed on HOPG before and after annealing to 400 °C, respectively. Before annealing,

$(WO_3)_3$ clusters were active for propene production. However, after annealing, the same clusters were no longer active toward propene production (92% loss of the catalytic activity). AFM was used to determine the structures of the as-deposited clusters as well as the effect of annealing, shown in Figure 6.5(c) and Figure 6.5(d), respectively. For the as-deposited $(WO_3)_3$ clusters, Figure 6.5(c) showed some degree of aggregation indicating the mobility of $(WO_3)_3$ clusters on HOPG surface, as expected for small sized clusters on HOPG.[21] The cluster aggregates are about 0.5~0.6 nm in height and their sizes are as large as several tens of nanometers revealed from the line scan shown in Figure 6.5(e). Therefore the $(WO_3)_3$ clusters deposited on HOPG aggregated into mostly two dimensional structures. However, no strong step-edge preference for cluster nucleation on the HOPG surface was observed, suggesting that clusters become immobilized once they have aggregated. Most importantly, in the context of the present investigation, the surface structure did not change visibly after annealing to 400 °C.

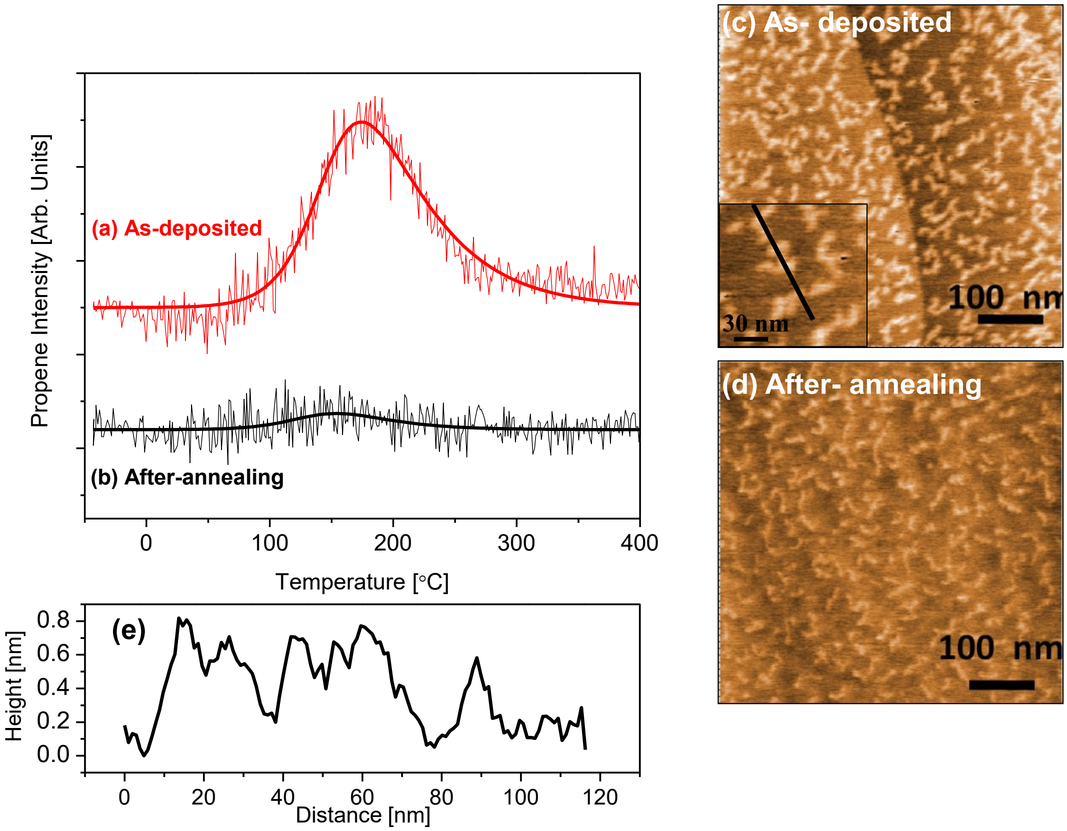

Figure 6.5 TPR traces of propene production of (WO$_3$)$_3$ clusters deposited on HOPG (a) as-deposited and (b) after-annealing to 400 °C; corresponding AFM images of the (c) as-deposited (insert shows a magnified image of the cluster aggregates) and (d) after-annealing (WO$_3$)$_3$ clusters deposited on HOPG; (e) A line scan of cluster aggregates along the black solid line shown in (c)

To investigate the support effect on the cluster activity, (WO$_3$)$_1$ was deposited onto two different supports, i.e., HOPG and annealed tungsten oxide films, and their catalytic activity was compared. Figure 6.6(a)(I) shows (WO$_3$)$_1$ monomers deposited on HOPG, while Figure 6.6(a)(II) shows (WO$_3$)$_1$ monomers deposited on annealed WO$_3$ films. As can be seen in Figure 6.6(a)(I), (WO$_3$)$_1$ monomers deposited on HOPG are relatively inactive. However, on annealed WO$_3$ films, deposited (WO$_3$)$_1$ monomers became active, as seen in

Figure 6.6(a)(II) (The propene peak area is at least five times larger for $(WO_3)_1$ monomers deposited on HOPG[40]). Thus, annealed oxide films are a significantly better support for promoting catalytically active tungsten oxide clusters.

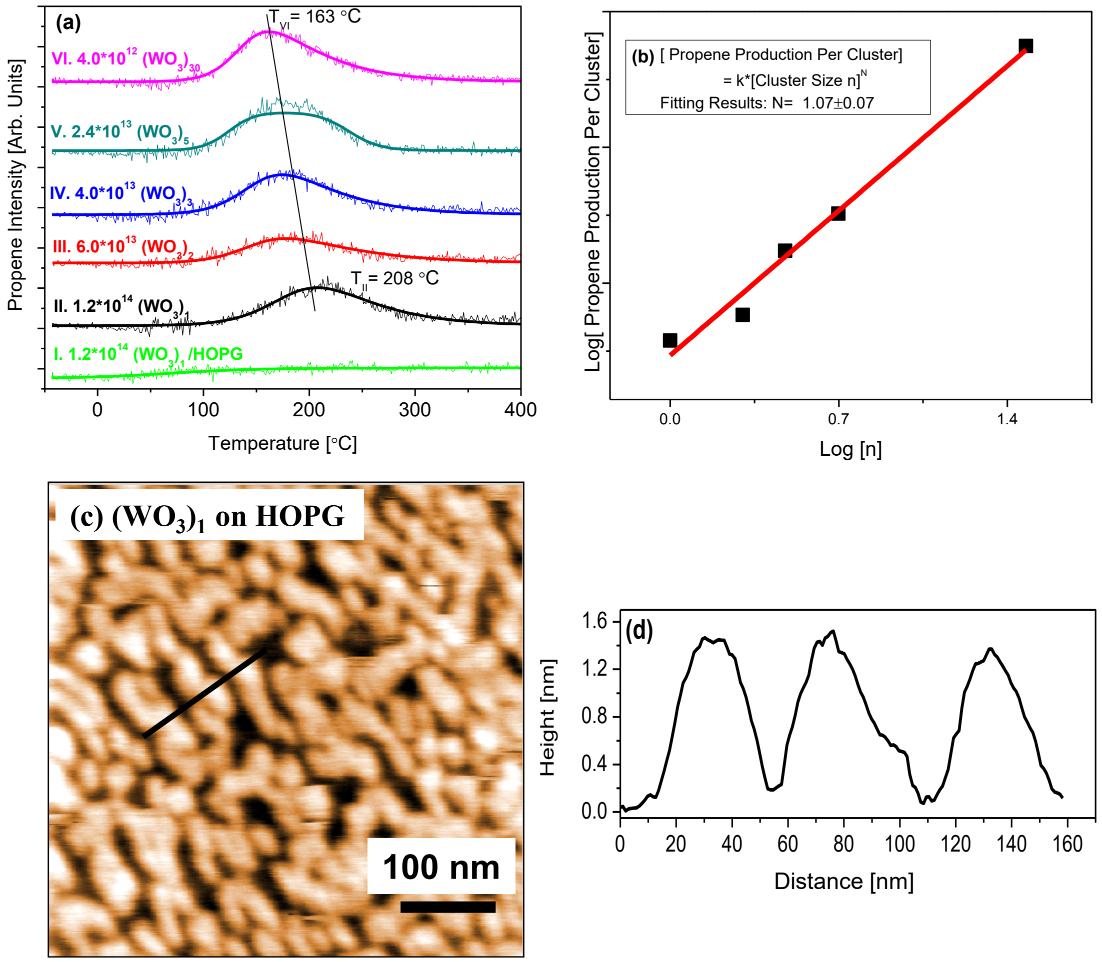

Figure 6.6 (a) TPR traces of propene production for (I) $(WO_3)_1$ clusters deposited on HOPG and (II) - (VI) $(WO_3)_n$ clusters deposited on annealed WO_3 films (n= 1, 2, 3, 5, 30) after dosing 0.2 L propanol; (b)Plot of Log[Propene Production per $(WO_3)_n$ cluster] vs. Log [Cluster Size n]; (c) AFM image of $(WO_3)_1$ monomers deposited on HOPG; (d) A line scan of cluster aggregates along the black solid line shown in (c)

Figure 6.6(a)(II) – (VI) presents TPR traces of propene production as a function of cluster size for $(WO_3)_n$ (n= 1, 2, 3, 5, 30) clusters deposited on annealed tungsten oxide films. All of these cluster sizes are active toward propene production. For each trace, the total number of W atoms deposited is the same. This was accomplished by ensuring that the total number of deposited clusters times that cluster's size (n number) was kept constant between different experiments. The propene desorption peak area for all the different sizes of clusters on the annealed oxide films displayed a similar value irrespective of the cluster size. This implies a correlation between the propene yield and the number of tungsten atoms involved in catalysis. Thus, a log-log fitting was applied to extrapolate the order of dependence. Indeed, by plotting Log [Propene production per cluster] vs. Log [Cluster size n] as shown in Figure 6.6(b), the gradient (N) is very close to 1 ($N = 1.07 \pm 0.07$), indicating a linear correlation exists.

Figure 6.7 displays the TPR traces for propene production for $(MoO_3)_3$ clusters and $(MoO_3)_1$ monomers deposited on HOPG [Figure 6.7(a) and (b)] and $(MoO_3)_n$ clusters deposited on annealed MoO_3 films [Figure 6.7 (c)-(g)]. In contrast to the behavior of $(WO_3)_n$ clusters, these TPR traces show that none of the $(MoO_3)_n$ clusters are catalytically active for 2-propanol dehydration to form propene, regardless of their size or the nature of the support.

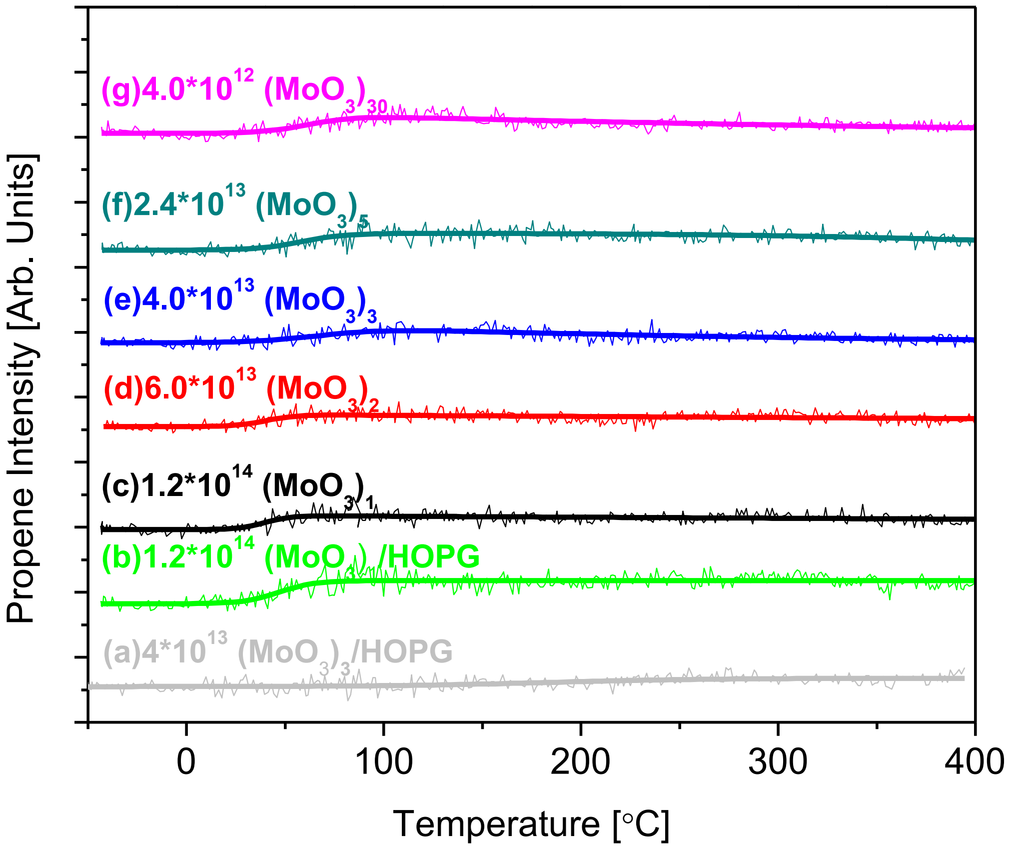

Figure 6.7 TPR traces of propene production for (a) $(MoO_3)_3$ and (b) $(MoO_3)_1$ clusters deposited on HOPG and (c)- (g) $(MoO_3)_n$ clusters deposited on annealed MoO_3 films (n = 1, 2, 3, 5, 30) [Note the y-axis scale is the same as the one in Figure 6.6(a)]

6.4 Discussion

6.4.1 Dehydration of 2-propanol on $(WO_3)_3$ Clusters

In previous studies Dohnálek et al. studied the catalytic dehydration of 2-propanol due to $(WO_3)_3$ trimers adsorbed on $TiO_2(110)$.[23] Through the use of IR spectroscopy and desorption measurements, the catalytic activity of these clusters was proposed to be a consequence of the presence of the O=W=O dioxo group within the cluster.[26]

Computational results also suggested that the dioxo groups were the favored sites for alcohol dehydration because of the greater Lewis acidity of these groups as compared to the monooxo groups, which translated into a lower activation energy barrier for alcohol dehydration via C-H and C-O bond cleavage.[26]

Results from the present investigation (Figure 6.3(b)) show that, as-deposited, mass-selected $(WO_3)_3$ clusters on HOPG are similarly catalytically active toward 2-propanol dehydration although they aggregate into cluster-island structures as shown in Figure 6.5(c). As seen in Figure 6.4, increasing the number of $(WO_3)_3$ clusters on the surface linearly increases propene production without changing the peak position indicating a linear increase of the accessible active sites in the cluster-island aggregates. These observations are qualitatively consistent with those of Dohnálek et al..[23] Annealing of the as-deposited clusters, however, leads to the 92% loss of catalytic activity as shown in Figure 6.5(b). In principle, this loss of activity might be a result of $(WO_3)_3$ cluster sintering on the HOPG surface during TPR heating, a phenomenon commonly observed for small clusters on HOPG surfaces.[41] However, as shown in Figure 6.5(c) and Figure 6.5(d), the AFM images acquired both before and after annealing did not exhibit dramatic changes in the surface morphology of the deposited clusters. Thus, aggregation effects do not appear to be responsible for the loss of activity. The likely interpretation, suggested by Dohnálek et al.[26] on the basis of IR data and desorption measurements is that annealing tungsten oxide results in the conversion of O=W=O dioxo groups into catalytically inactive W=O monooxo groups leading to a loss of catalytic activity. In this respect, a dioxo to monooxo bonding transformation would not necessarily change the surface morphology, but would diminish the catalytic activity of the clusters.

6.4.2 Influence of the Substrate

To probe the influence of the substrate, the activity of the $(WO_3)_1$ monomer was studied on two different substrates, i.e., on HOPG and on annealed WO_3 oxide films. Since annealed WO_3 oxide films themselves were shown to be catalytically inactive for 2-propanol dehydration (see Figure 6.5(b)), they were chosen as a point of comparison with HOPG substrates, which are also inactive towards 2-propanol dehydration in the absence of adsorbed clusters (See Figure 6.3(a)). Our results showed that $(WO_3)_1$ deposited on HOPG did not catalyze the dehydration reaction effectively, while the same quantity of $(WO_3)_1$ clusters deposited on annealed oxide films were catalytically active. [See (I) and (II) in Figure 6.6(a).] Generally, small clusters are extremely mobile on HOPG surfaces, and due to a combination of their mobility and high surface energy, they coalesce into larger aggregates with a reduced surface area[42] and a commensurate loss of catalytically active sites. Indeed, significant cluster aggregation is observed on HOPG in the case of deposited $(WO_3)_1$ monomers (see Figure 6.6(c)). As shown in Figure 6.6(d), $(WO_3)_1$ monomers aggregated three dimensionally on HOPG surface and coalesced into nanoparticles of about 1.5 nm in height. In contrast, much less cluster coalescence is observed for $(WO_3)_3$ clusters deposited on HOPG (compare Figure 6.5(c) and 6(c), Figure 6.5(e) and Figure 6.6(d)). This difference in aggregation behavior as a function of cluster size would explain the difference in reactivity between $(WO_3)_1$ and $(WO_3)_3$ deposited on HOPG. On the annealed WO_3 surface, we speculate that $(WO_3)_1$ becomes physically trapped or otherwise anchored, perhaps due to surface defects, preventing agglomeration. This is consistent with STM data from Dohnálek et al.[43] showing that $(WO_3)_3$ clusters deposited by PVD are immobilized on $TiO_2(110)$ surfaces, suggesting that the strength of interaction between tungsten oxide clusters and an underlying oxide surface will also be sufficiently large in magnitude to immobilize the clusters in the absence of significant aggregation and agglomeration. Unfortunately, direct imaging of the deposited clusters on annealed tungsten oxide surfaces by AFM is complicated by the roughness of the oxide support (see Figure 6.S3).

Analogous to the comparative study of $(WO_3)_1$, we compared 2-propanol dehydration reactions for $(WO_3)_3$ deposited on HOPG and annealed oxide films, shown in Figure 6.4 and Figure 6.6(a)(IV) respectively. For the same quantity of deposited $(WO_3)_3$ clusters the propene yield is approximately 6 times greater when they are deposited on annealed tungsten oxide as compared to HOPG substrates. Again, this observation underscores the importance of the support to prevent the cluster agglomeration. It should also be noted here that even for tungsten oxide clusters supported on annealed oxide films under this study, after annealing to 400 °C, none of the clusters studied are active toward the 2-propanol dehydration.

6.4.3 Size Dependent Catalytic Activity

We now discuss the size dependence of $(WO_3)_n$ catalytic activity on the dehydration of 2-propanol. Calculated structures from several groups[31,44-46] found $(WO_3)_n$ clusters, including the $(WO_3)_1$ monomer, to contain dioxo active sites, making all of them capable, in principle, of being catalytically active.

When $(WO_3)_1$ monomers were deposited on HOPG, they heavily coalesced and displayed low catalytic activity (see Figure 6.6(c) and Figure 6.6(a)(I)). In contrast, when $(WO_3)_1$ monomers were deposited on annealed tungsten oxide films they exhibited a measureable catalytic activity, suggesting a lack of aggregation (see Figure 6.6(a)(II)).

Thus, we chose to compare the catalytic activity of $(WO_3)_n$ clusters deposited on annealed tungsten oxide films. Indeed, Figure 6.6(a)(II) - (VI) indicate that all of the $(WO_3)_n$ clusters deposited on annealed WO_3 films are catalytically active toward the dehydration of 2-propanol. Moreover, by fitting the Log [Propene production per cluster] vs. Log [Cluster size n], a linear correlation ($N \approx 1$) was found between the cluster activity and the cluster size.

Two different mechanisms, i.e. linear-scaling of active sites and cluster ripening, could explain this linear scaling.

A. Linear scaling of active sites

Calculations[44] suggest that $(WO_3)_n$ clusters in the gas phase adopt a variety of structures, e.g., chains, rings or cage structures. Despite these possible isomeric structures, the most stable $(WO_3)_n$ isomers over the range of clusters studied in this previous investigation (n= 1~5) exhibit a 1:1 ratio in the number of O=W=O dioxo groups to the number of W atoms, e.g., $(WO_3)_3$ contains three dioxo active sites and three W atoms. As a result, the number of active sites in a given gas phase cluster is expected to scale linearly with cluster's size, i.e., with n. Although our clusters are supported on a surface and cover a wider range of cluster sizes, this linear dependency could still be operative. Additional support for the idea that the reactivity of the $(WO_3)_n$ clusters adsorbed on annealed tungsten oxide films is a reflection of a cluster size dependent reactivity can found in the systematic increase in the propene desorption peak temperature ($T_{VI} = 208$ °C for $(WO_3)_1$ and $T_{II} = 163$ °C for $(WO_3)_{30}$ in Figure 6.6(a)) observed as the deposited cluster sizes increase.

B. Cluster ripening

Another possibility that would explain the data shown in Figure 6.6(a) and (b) is that the deposited clusters aggregate and coalesce into similar sized clusters regardless of the initial size upon landing. In this scenario, although the size of the gas phase clusters is different, once they land onto the annealed metal oxide surface, surface ripening processes, i.e., Ostwald ripening and Smoluchowski ripening, modify the size of the clusters.[47] As an example of this phenomenon, the deposition of different sized silver clusters onto HOPG results in aggregates with similar sizes due to cluster coalescence.[41] However, the observation that the peak for propene desorption temperature varies systematically with increasing initial cluster size is seemingly inconsistent with the idea that cluster ripening leads to aggregates with similar sizes. Therefore, we believe that the data shown in Figure 6.6(b) is a consequence of differences in the reactivity of individual $(WO_3)_n$ clusters.

6.4.4 $(MoO_3)_n$ vs. $(WO_3)_n$

We also compared the dehydration of mass-selected, deposited $(MoO_3)_n$ clusters to $(WO_3)_n$ clusters. In common with studies on tungsten oxide clusters, $(MoO_3)_1$ and $(MoO_3)_3$ clusters were deposited onto HOPG but were found to be catalytically inactive (see Figure 6.7(a) and (b)). Size-selected $(MoO_3)_n$ clusters were also deposited onto annealed molybdenum oxide films, analogous to the studies conducted with WO_3 clusters. Figure 6.7 (a)-(g) show that none of the $(MoO_3)_n$ clusters sizes are active toward 2-propanol dehydration regardless of the size of the cluster or nature of the support. In related studies, when Dohnálek et. al. investigated the catalytic activity of $(MoO_3)_3$ clusters adsorbed on a graphene monolayer, itself grown on Pt(111), towards ethanol dehydration they also exhibited much lower catalytic activity than their $(WO_3)_3$ counterparts.[25] They ascribed this difference in the catalytic properties of (WO_3) and (MoO_3) clusters to the lower Lewis acidity of the metal center of $(MoO_3)_3$. Indeed, bulk studies on methanol dissociative adsorption have shown that MoO_3 is a weaker solid acid than WO_3.[48] Although theoretical calculations have found that the Lewis acidity of gas phase $(MoO_3)_n$ clusters is size dependent,[44] we discerned no obvious differences among the different $(MoO_3)_n$ cluster sizes. This suggests that any size dependent changes in Lewis acidity of $(MoO_3)_n$ clusters are insufficient to cause these clusters to become catalytically active towards 2-propanol dehydration.

6.5 Conclusions

The size dependent catalytic activity of 2-propanol dehydration on $(WO_3)_n$ and $(MoO_3)_n$ (n= 1, 2, 3, 5, 30) clusters supported on HOPG and annealed metal oxide films was studied. The ability of the support to immobilize the as-deposited clusters is suggested to play an important role in determining their catalytic activity. For $(WO_3)_n$ clusters deposited on annealed oxide films, we assert that the catalytic activity is a size dependent effect, although it is also possible that this is a consequence of cluster ripening. For $(MoO_3)_n$ clusters, low or no dehydration activity was observed for all of the clusters investigated, an effect ascribed to the lower Lewis acidity of the $(MoO_3)_n$ as compared to the $(WO_3)_n$ clusters.

Acknowledgments

This material is based on work supported by the Air Force Office of Scientific Research (AFOSR) under Grant No. FA9550-11-1-0068, the National Science Foundation (NSF)under Grant No. CHE-1360692, and the Defense Threat Reduction Agency (DTRA) under Grant No. HDTRA-1-12-1-007

Supporting Information

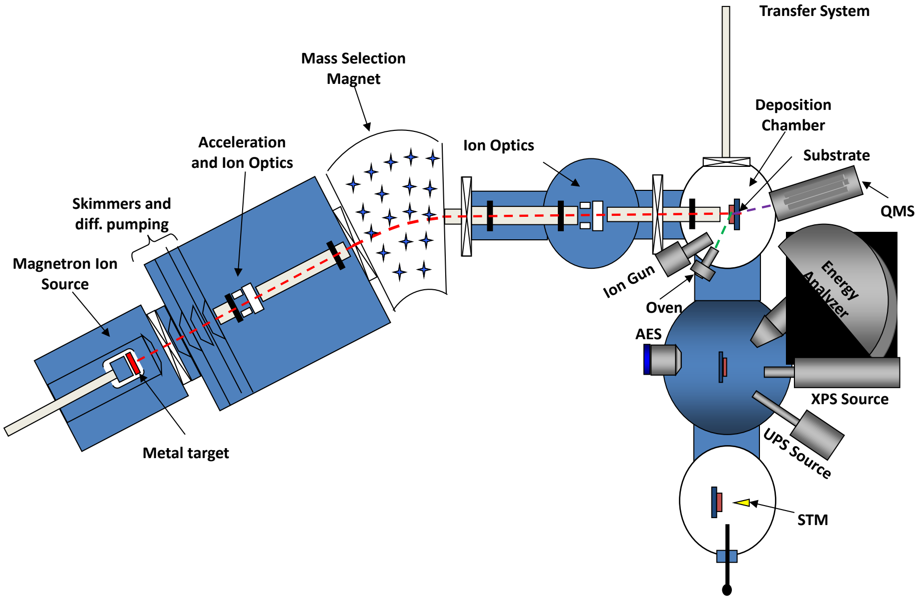

Figure 6.S1 Schematic of cluster deposition apparatus including cluster source, ion optics, magnetic sector, deposition chamber and surface analysis chambers.

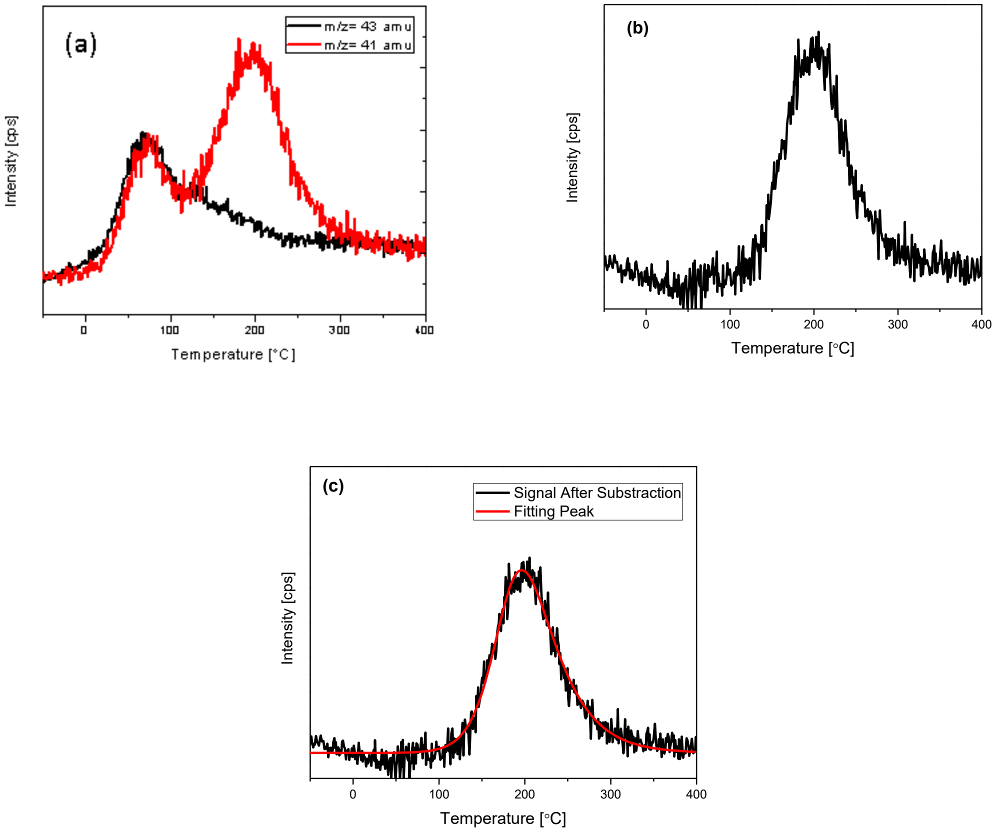

Figure 6.S2. Spectral Deconvolution for Propene Production (a) Normalized m/z = 41 amu and m/z= 43 amu TPR traces (b) Propene signal profile after subtraction of normalized m/z=43 amu signal from m/z= 41 amu signal (c) Peak Fitting for Propene Profile by Asymmetric Double Sigmoidal function. This function is chosen because it well resembles the peak profile for propene production

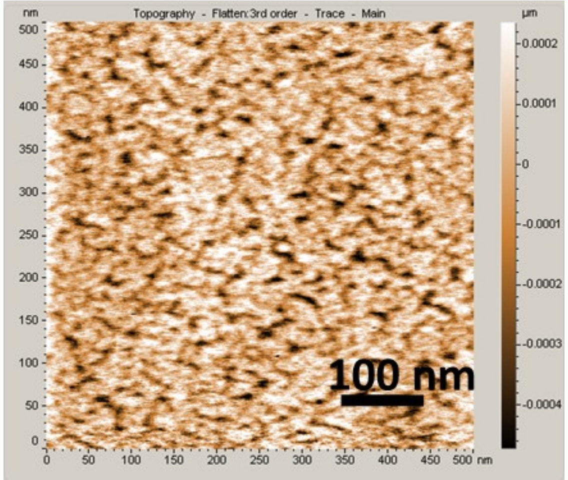

Figure 6.S3 AFM image of the WO_3 support. The annealed tungsten oxide substrate was prepared by depositing $(WO_3)_n$ cluster onto HOPG substrate where a full monolayer is achieved. The WO_3 film is then annealed to 400 °C.

References

(1) Billas, I. M. L.; Becker, J. A.; Chatelain, A.; Deheer, W. A. Phys Rev Lett 1993, 71, 4067.

(2) Castleman, A. W.; Bowen, K. H. The Journal of Physical Chemistry 1996, 100, 12911.

(3) Landman, U.; Yoon, B.; Zhang, C.; Heiz, U.; Arenz, M. Top Catal 2007, 44, 145.

(4) Yoon, B.; Hakkinen, H.; Landman, U.; Worz, A. S.; Antonietti, J. M.; Abbet, S.; Judai, K.; Heiz, U. Science 2005, 307, 403.

(5) Kaden, W. E.; Wu, T. P.; Kunkel, W. A.; Anderson, S. L. Science 2009, 326, 826.

(6) Heiz, U.; Vanolli, F.; Trento, L.; Schneider, W. D. Rev Sci Instrum 1997, 68, 1986.

(7) Jodicke, H.; Schaub, R.; Bhowmick, A.; Monot, R.; Buttet, J.; Harbich, W. Rev Sci Instrum 2000, 71, 2818.

(8) Lei, Y.; Mehmood, F.; Lee, S.; Greeley, J.; Lee, B.; Seifert, S.; Winans, R. E.; Elam, J. W.; Meyer, R. J.; Redfern, P. C.; Teschner, D.; Schlogl, R.; Pellin, M. J.; Curtiss, L. A.; Vajda, S. Science 2010, 328, 224.

(9) von Issendorff, B.; Palmer, R. E. Rev Sci Instrum 1999, 70, 4497.

(10) Wortmann, B.; Mende, K.; Duffe, S.; Grönhagen, N.; von Issendorff, B.; Hövel, H. physica status solidi (b) 2010, 247, 1116.

(11) Tong, X.; Benz, L.; Kemper, P.; Metiu, H.; Bowers, M. T.; Buratto, S. K. J Am Chem Soc 2005, 127, 13516.

(12) Wepasnick, K. A.; Li, X.; Mangler, T.; Noessner, S.; Wolke, C.; Grossmann, M.; Gantefoer, G.; Fairbrother, D. H.; Bowen, K. H. The Journal of Physical Chemistry C 2011, 115, 12299.

(13) Lin, J.; Zhou, Z.; Li, Z.; Zhang, C.; Wang, X.; Wang, K.; Gao, G.; Huang, P.; Cui, D. Nanoscale Research Letters 2013, 8, 170.

(14) Tamil Selvan, S.; Nogami, M.; Nakamura, A.; Hamanaka, Y. J Non-Cryst Solids 1999, 255, 254.

(15) Liang, Z.; Khosravian, H.; Uhl, A.; Meyer, R. J.; Trenary, M. Surf Sci 2012, 606, 1643.

(16) Óvári, L.; Bugyi, L.; Majzik, Z.; Berkó, A.; Kiss, J. The Journal of Physical Chemistry C 2008, 112, 18011.

(17) Khosravian, H.; Liang, Z.; Uhl, A.; Trenary, M.; Meyer, R. The Journal of Physical Chemistry C 2012, 116, 11987.

(18) Moseler, M.; Walter, M.; Yoon, B.; Landman, U.; Habibpour, V.; Harding, C.; Kunz, S.; Heiz, U. J Am Chem Soc 2012, 134, 7690.

(19) Price, S. P.; Tong, X.; Ridge, C.; Shapovalov, V.; Hu, Z. P.; Kemper, P.; Metiu, H.; Bowers, M. T.; Buratto, S. K. Surf Sci 2011, 605, 972.

(20) Ferguson, G. A.; Yin, C. R.; Kwon, G.; Tyo, E. C.; Lee, S.; Greeley, J. P.; Zapol, P.; Lee, B.; Seifert, S.; Winans, R. E.; Vajda, S.; Curtiss, L. A. J Phys Chem C 2012, 116, 24027.

(21) Li, X.; Wepasnick, K. A.; Tang, X.; Wang, Y.; Bowen, K. H.; Fairbrother, D. H.; Gantefoer, G. Journal of Vacuum Science & Technology B 2012, 30.

(22) Tang, X.; Li, X.; Wang, Y.; Wepasnick, K.; Lim, A.; Fairbrother, D. H.; Bowen, K. H.; Mangler, T.; Noessner, S.; Wolke, C.; Grossmann, M.; Koop, A.; Gantefoer, G.; Kiran, B.; Kandalam, A. K. Journal of Physics: Conference Series 2013, 438, 012005.

(23) Kim, Y. K.; Rousseau, R.; Kay, B. D.; White, J. M.; Dohnalek, Z. J Am Chem Soc 2008, 130, 5059.

(24) Li, S. C.; Li, Z. J.; Zhang, Z. R.; Kay, B. D.; Rousseau, R.; Dohnalek, Z. J Phys Chem C 2012, 116, 908.

(25) Li, Z. J.; Fang, Z. T.; Kelley, M. S.; Kay, B. D.; Rousseau, R.; Dohnalek, Z.; Dixon, D. A. J Phys Chem C 2014, 118, 4869.

(26) Li, Z. J.; Smid, B.; Kim, Y. K.; Matolin, V.; Kay, B. D.; Rousseau, R.; Dohnalek, Z. J Phys Chem Lett 2012, 3, 2168.

(27) Rousseau, R.; Dixon, D. A.; Kay, B. D.; Dohnalek, Z. Chemical Society Reviews 2014.

(28) Rothgeb, D. W.; Mann, J. E.; Jarrold, C. C. J Chem Phys 2010, 133.

(29) Huang, X.; Zhai, H. J.; Kiran, B.; Wang, L. S. Angewandte Chemie-International Edition 2005, 44, 7251.

(30) Huang, X.; Zhai, H. J.; Waters, T.; Li, J.; Wang, L. S. Angew Chem Int Edit 2006, 45, 657.

(31) Sun, Q.; Rao, B. K.; Jena, P.; Stolcic, D.; Kim, Y. D.; Gantefor, G.; Castleman, A. W. J Chem Phys 2005, 122.

(32) Zhai, H. J.; Kiran, B.; Cui, L. F.; Li, X.; Dixon, D. A.; Wang, L. S. J Am Chem Soc 2004, 126, 16134.

(33) Hammer, B.; Nørskov, J. K. In Advances in Catalysis; Bruce C. Gates, H. K., Ed.; Academic Press: 2000; Vol. Volume 45, p 71.

(34) Somorjai, G. A.; Carrazza, J. Industrial & Engineering Chemistry Fundamentals 1986, 25, 63.

(35) Bonanni, S.; Aït-Mansour, K.; Harbich, W.; Brune, H. J Am Chem Soc 2012, 134, 3445.

(36) Jensen, P. Rev Mod Phys 1999, 71, 1695.

(37) Xie, F. Y.; Gong, L.; Liu, X.; Chen, J.; Xie, W. G.; Zhang, W. H.; Chen, S. H. Appl Surf Sci 2009, 256, 693.

(38) Werfel, F.; Minni, E. Journal of Physics C: Solid State Physics 1983, 16, 6091.

(39) Falconer, J. L.; Schwarz, J. A. Catalysis Reviews 1983, 25, 141.

(40) The exact value cannot be more accurately determined because any propene signal from $(WO3)_1$/HOPG is on the same scale as the background noise

(41) Goldby, I. M.; Kuipers, L.; von Issendorff, B.; Palmer, R. E. Appl Phys Lett 1996, 69, 2819.

(42) Carroll, S. J.; Weibel, P.; Issendorff, B. v.; Kuipers, L.; Palmer, R. E. Journal of Physics: Condensed Matter 1996, 8, L617.

(43) Bondarchuk, O.; Huang, X.; Kim, J.; Kay, B. D.; Wang, L. S.; White, J. M.; Dohnalek, Z. Angewandte Chemie-International Edition 2006, 45, 4786.

(44) Li, S. G.; Dixon, D. A. J Phys Chem A 2006, 110, 6231.

(45) Sai, L.; Tang, L.; Huang, X.; Chen, G.; Zhao, J.; Wang, J. Chem Phys Lett 2012, 544, 7.

(46) Wang, B.; Chen, W. J.; Zhao, B. C.; Zhang, Y. F.; Huang, X. J Phys Chem A 2010, 114, 1964.

(47) Fukamori, Y.; Konig, M.; Yoon, B.; Wang, B.; Esch, F.; Heiz, U.; Landman, U. Chemcatchem 2013, 5, 3330.

(48) Badlani, M.; Wachs, I. Catal Lett 2001, 75, 137.

7. Decomposition of DMMP by Size-Selected $(MoO_3)_3$ Clusters

Xin Tang[1], Zachary Hicks[1], Linjie Wang[1], Gerd Ganteför[2], D. Howard Fairbrother[1], Kit H. Bowen[1] a)

Roman Tsyshevsky[3], Jianwei Sun[4], Maija M. Kuklja[3] b)

1 Department of Chemistry, Johns Hopkins University, Baltimore, Maryland 21218, USA

2 Department of Physics, University of Konstanz, 78464 Konstanz, Germany

3Department of Materials Science, University of Maryland, College Park, Maryland 20742, USA

4Department of Physics, Temple University, Philadelphia, Pennsylvania 19122, USA

Abstract

The adsorption and decomposition behavior of dimethyl methylphosphonate (DMMP), a chemical warfare agent (CWA) simulant, on size-selected molybdenum oxide trimer clusters, i.e. $(MoO_3)_3$, was studied. X-ray photoelectron spectroscopy (XPS) and temperature programmed reaction (TPR) were used to study the surface compositions of the DMMP on $(MoO_3)_3$ and the reaction products, respectively. The TPR showed both desorption and decomposition of DMMP on $(MoO_3)_3$ clusters with methanol as the major gaseous product observed after decomposition. Theoretical investigation of DMMP on $(MoO_3)_3$ clusters suggested that, in addition to pure $(MoO_3)_3$ clusters, reduced molybdenum oxide clusters and hydroxylated molybdenum oxide clusters play an important role in lowering the reaction barrier of DMMP decomposition.

7.1 Introduction

Organophosphate compounds are well known for their toxicity, as they are used in pesticides, herbicides, and as chemical warfare agents (CWA). As such it is of significant interest to study their adsorption and decomposition behaviors on various filter materials used to protect people from exposure.[1] Dimethyl methylphosphonate (DMMP) is commonly used as a CWA simulant due to its lower toxicity, low vapor pressure, and its structural similarity to some nerve agents. In addition to the traditional carbon-based filter material[2], the adsorption and decomposition properties of metal oxides towards CWA simulants have been widely studied. Some of the oxides that have been studied include TiO_2 [3,4], Al_2O_3 [4,5] MgO[4,5], WO_3[4], La_2O_3[5] ,CeO_2[6], SiO_2 [7,8]. Many of the metal oxides studied exhibited considerable activity in adsorbing and decomposing the simulant molecules. In studies on DMMP, it was found that on most metal oxides DMMP first binds to the acid sites of the metal oxides surface, i.e. metal ion site, and then undergoes a stepwise decomposition process resulting in the loss of methoxy groups. [5,6]

Currently, most of the experimental studies of DMMP decomposition on metal oxides have been performed on either micro-particles or on single crystal surfaces. A few theoretical reports found in literature show that simulations were used to determine the binding sites and energies between DMMP and some metal oxide clusters, i.e. hydroxylated $(TiO_2)_n$ [9], $(SiO_2)_n$ [10,11], and $(ZnO_2)_n$ [12]. However, details of the decomposition mechanisms are still poorly understood. An addition of decomposition studies on small, well-defined metal oxide structures, such as clusters, would allow for detailed theoretical modeling to shed light on the decomposition process.

In this work, the adsorption and decomposition of DMMP molecules on $(MoO_3)_3$ trimer clusters was studied experimentally and theoretically. X-ray photoelectron spectroscopy (XPS) and temperature programmed reaction (TPR) were used to investigate the fate of DMMP on $(MoO_3)_3$ clusters. Density function theory (DFT) based calculations were used to investigate both the adsorption configuration as well as the decomposition pathway of the DMMP molecule on $(MoO_3)_3$ clusters.

7.2 Experimental Methods

Molybdenum oxide trimer clusters $(MoO_3)_3$ were prepared as negative anions by a magnetron sputtering source. After mass selection and deceleration, they were then deposited (soft-landed) onto a highly-ordered pyrolitic graphite (HOPG) substrate in an ultra-high vacuum (UHV) environment ($1x10^{-9}$ torr).

The magnetron setup consisted of a molybdenum target placed in a magnetic field and biased to -500 V while a mixture of argon, helium and oxygen gases was introduced. The argon gas was ionized to create argon cations, which sputtered the metal target to produce molybdenum atoms and electrons. After reaction with the oxygen to form oxides, the resulting metal oxides aggregated, attached electrons, and formed molybdenum oxide cluster anions. The added helium served to cool and transport the cluster anions down the beamline, where they were then electrostatically accelerated before entering a magnetic sector mass spectrometer (25° sector magnet with resolution of $m/\Delta m = 20$). By tuning the magnetic field strength, $(MoO_3)_3^-$ cluster anions were mass-selected and focused by ion optics before entering the deposition chamber, where they were soft-landed (<1eV) onto a freshly peeled HOPG surface. The resulting sample can be cooled to approximately $-160^\circ C$ by liquid nitrogen (LN_2) or heated via resistive heating by passing current through the

HOPG, with the temperature of the sample being monitored by a K-type thermocouple spring loaded to the back of the HOPG.

Once clusters had been deposited onto the HOPG substrate, a TPR set-up, using a Hiden HAL/3F PIC quadrupole mass spectrometer (QMS), was used to characterize their activity. The reaction products that desorbed from the surface during a temperature ramp were detected and identified by the QMS which was positioned normal to the plane of the substrate and at a distance of 5 mm. To minimize the contribution from background gases and maximize the sensitivity towards species desorbing directly from the substrate the QMS ionizer was surrounded by a custom built glass shroud. In addition, deposited samples could also be transferred *in situ* to an adjacent UHV chamber, where they were characterized by X-ray Photoelectron Spectroscopy (*in situ* XPS) with non-monochromatic Mg Kα-rays (1253.6 eV), with the ejected electron kinetic energy analyzed via a high energy hemispherical analyzer. The sample can be *in situ* heated by e-beam heating with the temperature measured by a K type thermocouple connected to the sample holder.

Typically, in the TPR experiment, 0.2 Langmuir of DMMP was first dosed to a freshly-peel HOPG surface cooled to -173 ºC. After that, $(MoO_3)_3$ clusters were deposited into the multilayers of DMMP. By depositing $(MoO_3)_3$ clusters into the DMMP layer, one can expect that the clusters can preferentially interact with the surrounding DMMP molecules rather than sintering. Indeed, monodispersed molybdenum oxide clusters were observed via *ex-situ* atomic force microscopy. (See Figure 7.S1 in the Supporting Information) The number of clusters deposited is calculated by integrating the ion current over the deposition time. Following the deposition, the surface temperature was first raised to 0 ºC to desorb the vast majority of physisorbed DMMP, and eventually to 450 ºC with a ramping rate of

2 ºC/s. In the XPS studies, a higher pressure of DMMP (5×10^{-7} torr) was dosed during deposition in order to saturate the adsorption sites on $(MoO_3)_3$. In both cases the deposition was performed with the substrate at room temperature. The DMMP was purified by several freeze-pump-thaw cycles before being background dosed through a UHV compatible leak valve.

7.3 Density Functional Theory Calculations

Calculations were carried out within density functional theory (DFT)[13,14] using a hybrid B3LYP functional[15,16], its long range corrected version CAM-B3LYP [17], and a B3LYP+D3 functional including Grimme's empirical dispersion[18]. In addition to the three variants of the B3LYP functional, a recently developed meta-generalized-gradient (meta-GGA) functional SCAN [19,20] was also employed for calculations of desoprtion energies. The double-ζ 6-31+G(d,p) basis set was used for the H, C, O, and P atoms. The LanL2DZ basis set, [21,22,23] including the Los Alamos effective core potential, was used for the Mo atoms. Vibrational frequencies were calculated for relevant atomistic configurations to distinguish energy minima and transition states. The stationary points corresponding to the energy minima were positively identified by having no imaginary frequencies, and the transition states were confirmed to have exactly one imaginary frequency. Reaction paths were investigated by conducting intrinsic reaction coordinate computations using the Hessian-based Predictor-Corrector integrator algorithm [24,25]for each transition state. All calculations were carried out in the Gaussian09 code[26]. The modified version of the Gausian 03 code [27]was used to perform calcuations using the SCAN functional.

7.4 Results

7.4.1 XPS characterization of DMMP on $(MoO_3)_3$ Clusters

The temperature dependent XPS spectra of the P(2p) region for DMMP on $(MoO_3)_3$ are displayed in Figure 7.1. As shown in the Figure 7.1(a), the P(2p) peak of DMMP on $(MoO_3)_3$ at room temperature was centered at 133.5 eV, compared to the 134.0 eV in the control case of DMMP adsorbed on clean HOPG. The slightly lower binding energy of the P(2p) peak indicates that the phosphorus in DMMP on $(MoO_3)_3$ was partially reduced at room temperature. After heating the sample to 200 °C and allowing it to cool back to room

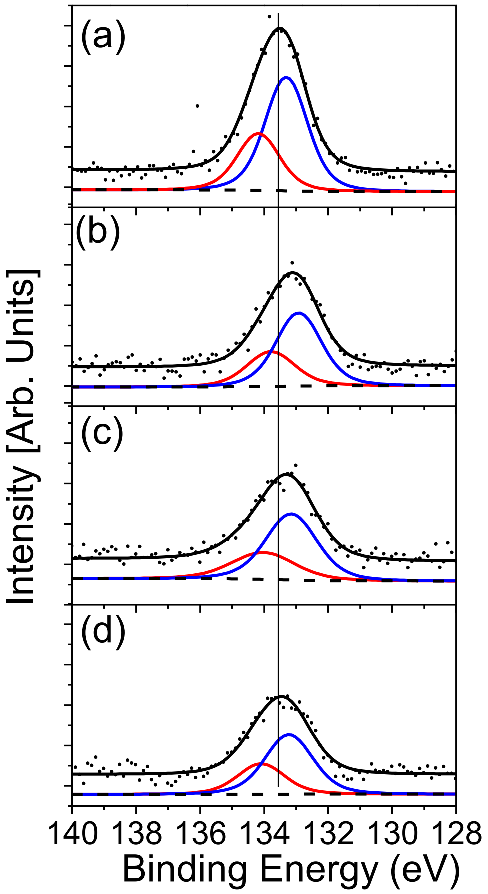

Figure 7.1 XPS spectra of the P(2p) envelope of DMMP adsorbed on $(MoO_3)_3$ clusters as a function of annealing temperature (a) RT (b) 200 °C(c) 300 °C(d) 400 °C

temperature, the binding energy of the P(2p) peak shifted slightly to an even lower binding energy of 133.1eV (Figure 7.1(b)). Further annealing to higher temperatures (300 °C and 400 oC) shifted the P(2p) peak back to the original position, possibly due to the formation of a PO_x species, which was previously seen with DMMP on other oxides.[6] (Figure 7.1(c)(d)).

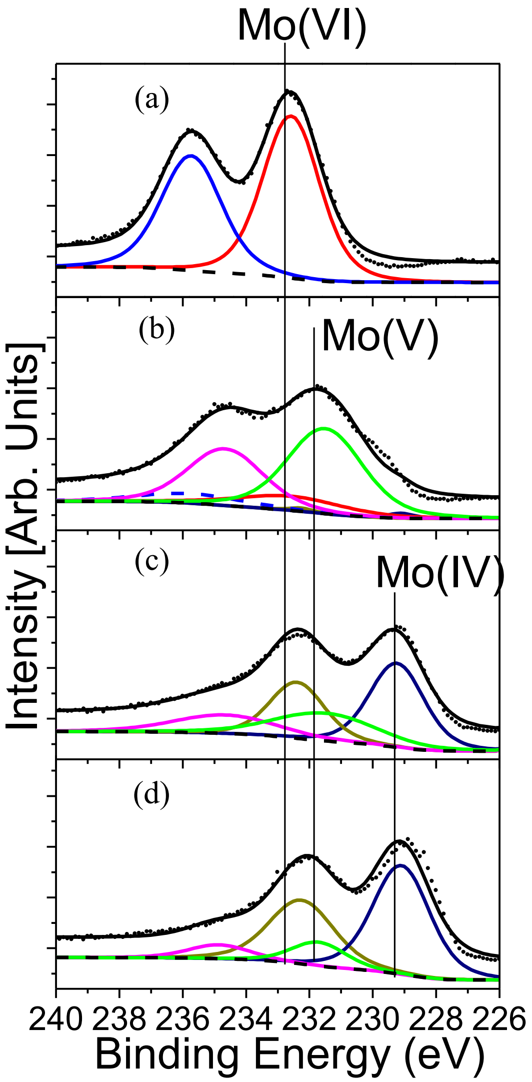

Figure 7.2 XPS spectra of the Mo(3d) envelope of $(MoO_3)_3$ clusters as a function of annealing temperature (a) RT (b) 200ºC(c) 300ºC(d) 400ºC.

The temperature dependent XPS spectra of the Mo(3d) region is shown in Figure 7.2. The XPS spectra for the Mo(3d) of $(MoO_3)_3$ at room temperature displayed a doublet peak, $3d_{5/2}$ and $3d_{3/2}$, centered at 232.5 eV and 235.6 eV, respectively (Figure 7.2(a)). The binding energy of Mo($3d_{5/2}$) is consistent with the binding energy of Mo($3d_{5/2}$) in Mo(VI), indicating the presence of MoO_3.[28] After heating to 200 °C (Figure 7.2(b)), the binding energy of Mo(3d) shifted to a lower binding energy, which indicates that MoO_3 was reduced. Further annealing to 300°C and 400 °C caused more reduction, resulting in a mixture of lower oxidation species, i.e. Mo(IV) and Mo(V). (Figure 7.2(c)(d))

The relative atomic ratio of P to Mo at different temperatures was calculated and is shown in Figure 7.3. This ratio is calculated by dividing the peak area of P(2p) and Mo(3d) with their respective relative sensitivity factor (R.S.F.) and comparing the resulting values. The as-deposited DMMP on $(MoO_3)_3$ ratio of P to Mo is around 0.31. This indicates that for every $(MoO_3)_3$ cluster, about one DMMP molecule (~0.95) is adsorbed to it. It's worth noting that the ratio of P to Mo decreased with increasing temperature from room temperature to 200 ^{o}C. The loss of phosphorus upon heating is possibly due to the desorption of intact DMMP and other phosphorus-containing species such as reaction products. The decrease in the P to Mo ratio is dramatic from room temperature to 200 ^{o}C, and flat from 200 ^{o}C to 400 ^{o}C, indicating the vast majority of DMMP and phosphorous containing compounds desorbed during the temperature range of RT to 200 ^{o}C.

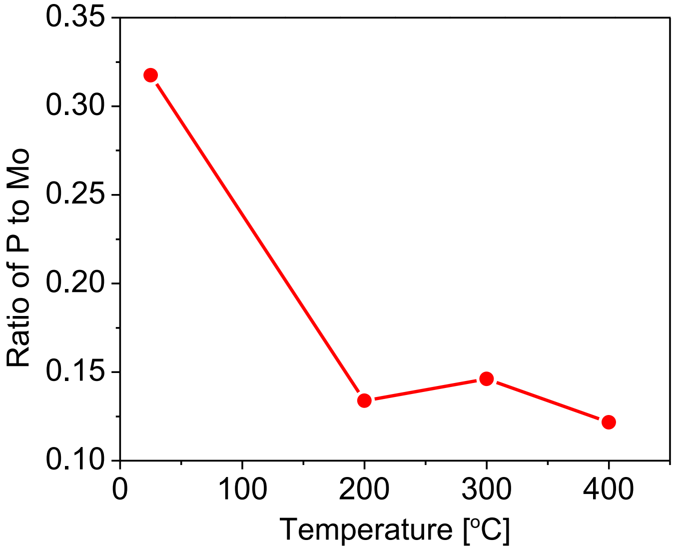

Figure 7.3 The relative atomic ratio of P to Mo of DMMP on $(MoO_3)_3$ Clusters as a function of annealing temperature.

7.4.2 Temperature programmed reaction (TPR) of DMMP on $(MoO_3)_3$

The TPR profiles of DMMP on $(MoO_3)_3$ clusters are recorded in Figure 7.4, for the masses of 124 amu, 79 amu, 46 amu, 32 amu, 31 amu, 16 amu, 15 amu, and 2 amu. The mass of 124 amu corresponds to the parent ion of DMMP, while the mass of 79 amu is ascribed to the major fragment of DMMP (PO_3^+). The mass of 46 amu corresponds to dimethyl ether, while 32 and 31 amu are the masses for methanol and its deprotonated form, methoxy, respectively. Masses 16, 15, and 2 amu are methane, methyl, and hydrogen respectively. The TPR profiles of DMMP on HOPG without clusters were included in the supporting information (Figure 7.S2).

Both 124 and 79 amu showed the same desorption profiles, with a desorption peak centered at 100 °C. This is consistent with the XPS result showing that the majority of

DMMP desorbed in the temperature range of RT to 200 °C. Using Redhead Analysis[29] a desorption energy of 23.4 kcal/mol was determined for intact DMMP. For the masses of 32 and 31 amu, a broad desorption peak was observed in both cases, indicating the production of methanol upon heating. The peak position, centered around 200 °C, gives a desorption energy of 29.8 kcal/mol for methanol. The lower temperature shoulder at 107 °C for 31 amu is a minor fragment from DMMP. No peaks were observed resulting from H_2 (2 amu), CH_4 (16 amu), and dimethyl ether (46 amu). The desorption profile of 15 amu replicated the desorption profile of DMMP. Further subtraction of DMMP contribution will reveal an additional shoulder around 198 °C, corresponding to a desorption energy of 29.7 kcal/mol for the methyl group. (see Figure 7.S3) In contrast, only desorption of DMMP was observed on the HOPG surface.

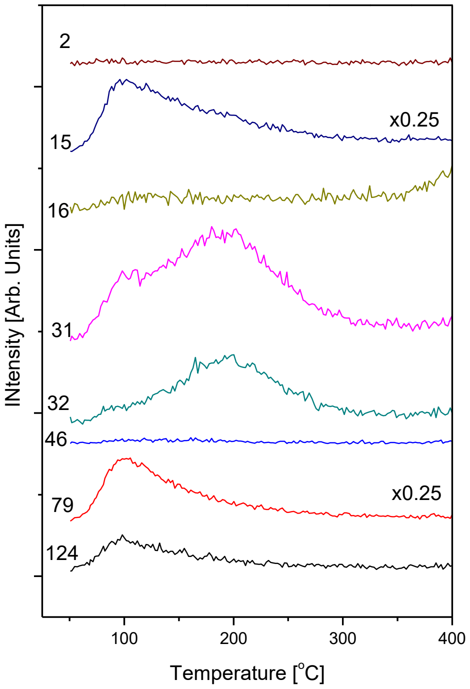

Figure 7.4 Temperature programmed reaction profile of DMMP on $(MoO_3)_3$

7.4.3 DMMP adsorption on $(MoO_3)_3$

Oxygen vacancies and hydroxyl groups are very common on various metal oxide surfaces.[30] It is reasonable to assume that the surface of the clusters could be populated with some reduced molybdenum metal centers as well as some residual hydroxyl groups. Therefore, while simulating adsorption and decomposition of DMMP on molybdenum oxide clusters several models were considered. (Figures 5 and 6) The models include a DMMP molecule adsorbed on: (1) an ideal cluster, $(MoO_3)_3$, (Figure 7.5b), (2) a reduced cluster, Mo_3O_8, (Figure 7.5c), and (3) a series of hydroxylated clusters $Mo_3O_9H_n$ (n=1-3, Figure 7.6a-h).

Calculations show that the most stable configuration of DMMP adsorbed on the $(MoO_3)_3$ cluster corresponds to the structure in which the DMMP molecule is oriented with its phosphoryl oxygen inside the cluster ring with the methyl and methoxy groups placed between the oxygen atoms of the cluster (Figure 7.5b). This is consistent with previous studies on Al_2O_3, MgO[5] and WO_3[4].

Figure 7.5b shows a noticeable elongation of the P-O bond (by ~0.04 Å) and shortening of the P-OCH_3 bond (by ~0.02-0.04 Å) in DMMP adsorbed on $(MoO_3)_3$ clusters when compared with the gas-phase molecule. The distances of the P-CH_3 and O-CH_3 bonds change slightly (by ~0.01 Å) when DMMP is adsorbed on $(MoO_3)_3$. The desorption energy of DMMP on $(MoO_3)_3$, calculated using B3LYP, is 17.7 kcal/mol (Table 7.1). The desorption energy obtained using the long range corrected CAM-B3LYP functional (24.1 kcal/mol) is ~6 kcal/mol higher than B3LYP estimation, whereas the inclusion of van-der-Waals interactions via Grimme's empirical dispersion tends to increase the resulting desorption energy by additional ~8 kcal/mol (32.0 kcal/mol). A similar trend is observed for the different adsorption configurations of DMMP on the stoichiometric and reduced clusters (Table 7.1). The desorption energies, recalculated using the meta-GGA SCAN functional developed for accurate prediction of weak nonbonding interactions[19], are consistent with B3LYP+D3 estimations. We therefore will refer in our discussion of the desorption energies to the numbers obtained at B3LYP+D3 level.

Resulting structures indicate that there is no additional adsorption sites available on the $(MoO_3)_3$ clusters for adsorbing another DMMP molecule, leaving one DMMP adsorbed on one $(MoO_3)_3$ as consistent with the XPS results.

The DMMP adsorption on the reduced Mo_3O_8 cluster was simulated (Figure 7.5c). The DMMP adsorbed molecule has a slightly shortened P-OCH_3 (by ~0.015 Å) and elongated PO-CH_3 (by ~0.015 Å) bonds as compared to the DMMP molecule adsorbed on an ideal $(MoO_3)_3$ cluster (Figure 7.5b). The calculated desorption energy is 40 kcal/mol (Figure 7.5c, Table 7.1).

There is a negligible change in bond distances of the DMMP molecule adsorbed on the hydroxylated cluster in comparison to DMMP adsorbed on ideal cluster (Figure 7.5b and d). The calculated desorption energy of the DMMP molecule from the hydroxylated cluster is 28.6 kcal/mol (Figure 7.5d, Table 7.1). The desorption energies obtained for different configurations of DMMP on $Mo_3O_9H_2$ and $Mo_3O_9H_3$ clusters fall in the range 19-28 kcal/mol (Figure 7.6b-h, Table 7.1).

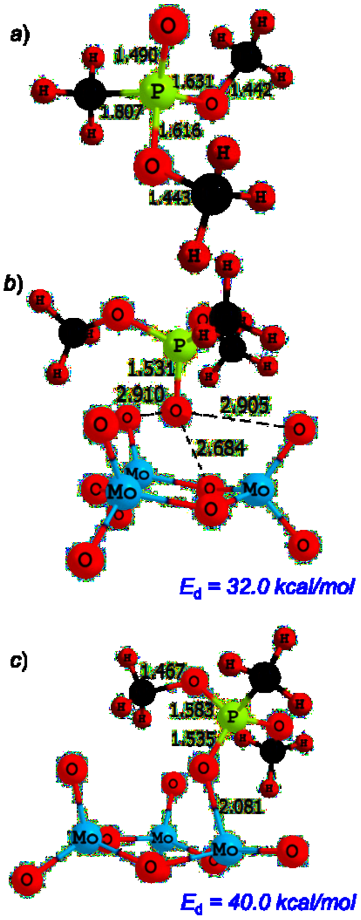

Figure 7.5 Geometry structures of the DMMP molecule a) in gas-phase; b) adsorbed on a $(MoO_3)_3$ cluster; c) adsorbed on a reduced Mo_3O_8 cluster (ZPVE corrected desorption energies calculated using B3LYP+D3 functional are in blue)

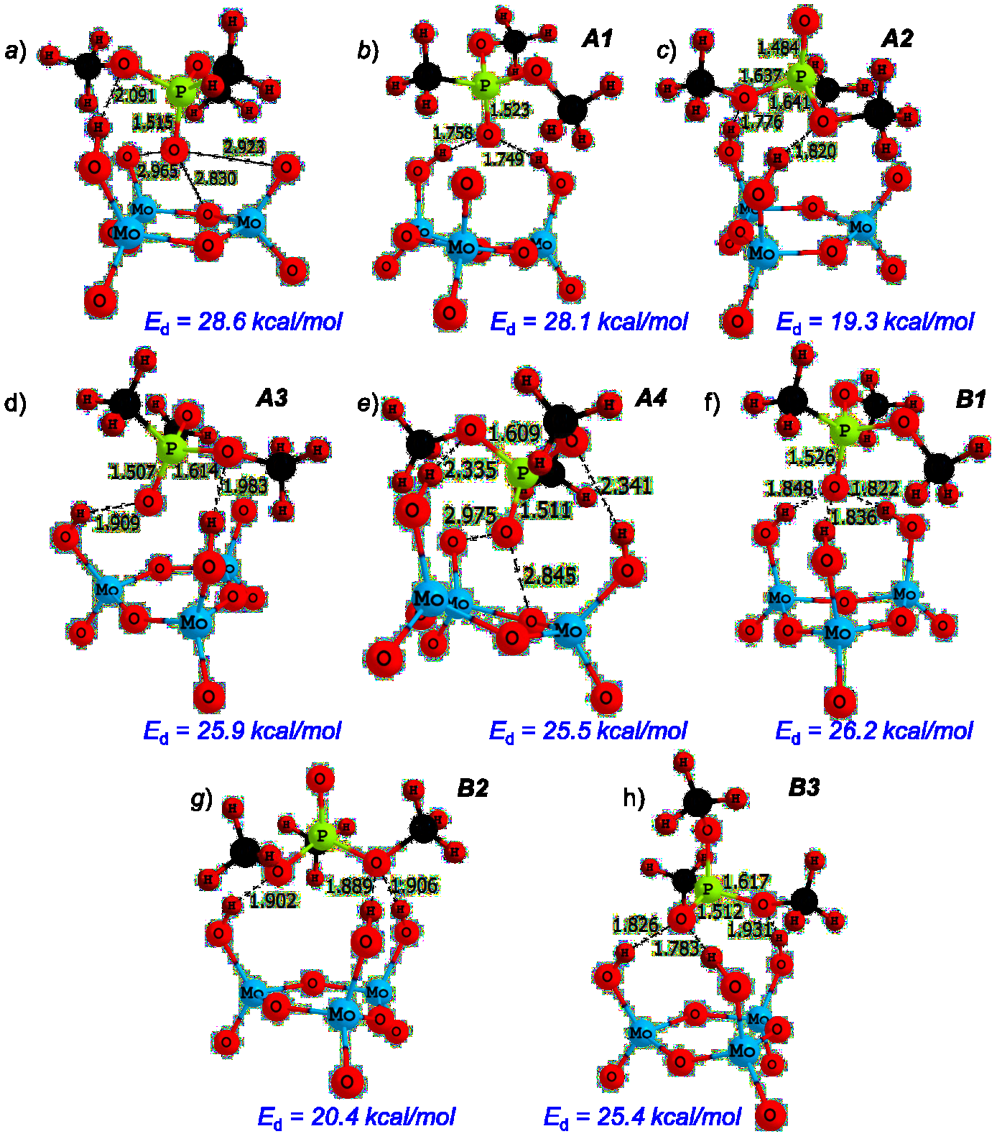

Figure 7.6 Geometry structures of the DMMP molecule adsorbed on the hydroxylated a) Mo_3O_9H, b)-e) $Mo_3O_9H_2$, and f)-h) $Mo_3O_9H_3$ clusters (ZPVE corrected desorption energies calculated using B3LYP+D3 functional are in blue).

Table 7.1 Calculated and experimental desorption energies (in kcal/mol) of the DMMP molecule from the molybdenum oxide clusters

Cluster		Theory							Exp.
		B3LYP		CAM-B3LYP		B3LYP+D3		SCAN[a]	
		E	E+ZPVE	E	E+ZPVE	E	E+ZPVE	E	
Mo_3O_9		19.1	17.7	25.6	24.1	33.8	32.0	35.7	23.4
Mo_3O_8		29.5	28.6	35.4	34.2	41.4	40.0	35.8	
Mo_3O_9H		15.5	13.8	21.9	19.9	30.7	28.6	31.4	
$Mo_3O_9H_2$	Config. ***A1***	19.1	17.1	22.9	20.6	30.1	28.1	25.6	
	Config. ***A2***	9.6	7.8	12.3	10.2	21.3	19.3	15.7	
	Config. ***A3***	15.9	14.0	20.3	18.2	28.0	25.9	23.5	
	Config. ***A4***	-		20.0	17.9	27.2	25.5	26.9	
$Mo_3O_9H_3$	Config. ***B1***	19.2	17.4	27.4	25.4	28.3	26.2	23.8	
	Config. ***B2***	11.2	9.6	19.8	18.0	22.6	20.4	15.0	
	Config. ***B3***	19.5	17.6	20.7	18.5	27.6	25.4	21.9	

[a] Total electronic energies were obtained through single point calculations using geometry structure optimized with B3LYP+D3 functional

7.4.4 DMMP decomposition on $(MoO_3)_3$

Decomposition mechanisms of DMMP in the gas phase and on the molybdenum oxide clusters were studied using the CAM-B3LYP functional. Although the CAM-B3LYP functional underestimates energies of the DMMP desorption from $(MoO_3)_3$ relative to the B3LYP+D3 method, the decomposition energies obtained using these functionals were found to be in good agreement.

In order to study the decomposition of DMMP adsorbed on molybdenum oxide clusters and in the gaseous phase we simulated cleavage of the P=O (Eq. 1, Path 1, Figure 7.7), P-CH_3 (Eq. 2, Path 2, Figure 7.7), O-CH_3 (Eq. 3, Path 3, Figure 7.7), and P-OCH_3 (Eq. 4, Path 4, Figure 7.7) bonds together with concerted intramolecular elimination of methanol (Eq. 5, Path 5, Figure 7.7). In addition to these five reactions, we also studied the mechanism of methanol elimination involving cluster-to-molecule intermolecular hydrogen transfer that can occur on the hydroxylated $Mo_3O_9H_n$ (n=1,2) clusters. (Eq. 6, Path 6, Figure 7.7). Calculated activation barriers and reaction energies are collected in Table 7.2.

$(CH_3)PO(OCH_3)_2 \rightarrow (CH_3)P(OCH_3)_2 + {}^3O(\text{atom})$

(1)

$CH_3)PO(OCH_3)_2 \rightarrow {}^{\bullet}PO(OCH_3)_2 + {}^{\bullet}CH_3$

(2)

$(CH_3)PO(OCH_3)_2 \rightarrow (CH_3)PO(OCH_3)O^{\bullet} + {}^{\bullet}CH_3$

(3)

$(CH_3)PO(OCH_3)_2 \rightarrow (CH_3)P^{\bullet}O(OCH_3) + {}^{\bullet}OCH_3$

(4)

$((CH_3)PO(OCH_3)_2 \rightarrow (CH_2)PO(OCH_3) + HOCH_3$

(5)

$H_n(MoO_3)_3\text{-}(CH_3)PO(OCH_3)_2 \rightarrow H_{n-1}(MoO_3)_3\text{-}(CH_3)PO(OCH_3) + HOCH_3$

(6)

The breaking of the P=O bond in the gaseous phase requires the highest energy (130.7 kcal/mol) among all probed reactions. The cleavage of the P-OCH_3 bond is a noticeably less costly process (93.1 kcal/mol), whereas breaking the P-CH_3 and O-CH_3 bonds requires ~10 kcal/mol less energy (84.0 and 83.3 kcal/mol, respectively). The elimination of methanol is the most energetically favorable process with an activation barrier of 67.5 kcal/mol. These findings are consistent with results of the recent study reporting methyl and methanol, among other products, of DMMP pyrolysis in gaseous phase[31].

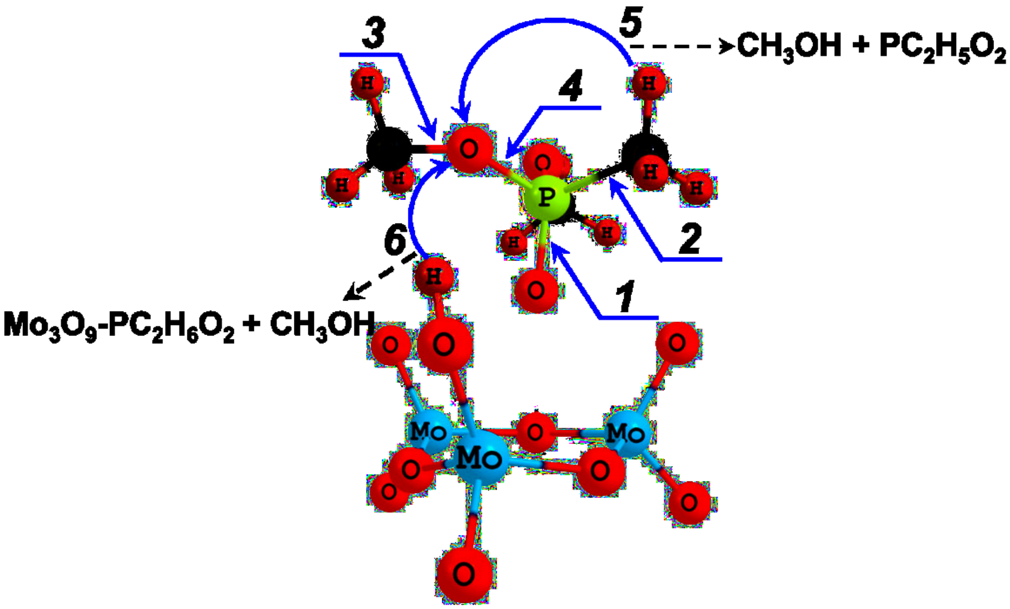

Figure 7.7 Schematic representation of decomposition channels of DMMP. (1) Breaking of the P=O bond. (2) Breaking of the P-CH_3 bond. (3) Breaking of the O-CH_3 bond. (4) Breaking of the P-OCH_3 bond. (5) Elimination of methanol via intramolecular proton transfer. (6) Elimination of methanol via intermolecular proton transfer.

Table 7.2 Calculated (including ZPVE corrections) and experimental decomposition energies (in kcal/mol) of DMMP adsorbed on molybdenum oxide clusters. (Reaction energies for methanol loss reactions are shown in parentheses)

Reaction	Gas	Oxide cluster				EXP
		Mo_3O_9	Mo_3O_8	Mo_3O_9H	$Mo_3O_8H_2$	
P=O	130.7	-	-	-	-	-
P-CH_3	84.0	90.5	56.4	75.8	75.5	-
O-CH_3	83.3	91.3	22.1	30.7	20.6	29.7
P-OCH_3	93.1	95.9	68.1	87.6	70.3	-
CH_3OH loss (intramolecular)	67.5 (65.5)	72.3 (71.2)	70.7 (66.5)	71.5 (86.8)	71.4 (2.9)	29.8
CH_3OH loss (intermolecular)	-	-	-	23.9 (12.3)	20.0 (2.9)	

The decomposition of DMMP adsorbed on ideal $(MoO_3)_3$ clusters requires even higher energy than decomposition in the gaseous phase (Table 7.2). The energy required for cleavage of P-CH_3 and O-CH_3 bonds increases by ~6-8 kcal/mol. The elimination of methanol remains the most favorable process and requires ~20 kcal/mol lower energy (72.3

kcal/mol) as compared to homolysis of the P-CH_3 (90.5 kcal/mol), O-CH_3 (91.3 kcal/mol) and P-OCH_3 (95.9 kcal/mol) bonds.

Significantly lower energies are required for the decomposition of DMMP on reduced Mo_3O_8 clusters as compared to the gaseous phase (Table 7.2). Cleavage of the O-CH_3 bond requires 25.1 kcal/mol instead of the 91.3 kcal/mol on an ideal $(MoO_3)_3$ cluster. Table 7.1 reveals a reduction of P-CH_3 and P-OCH_3 bond energies by ~30 kcal/mol as compared to a DMMP molecule adsorbed on an ideal cluster.

The activation barrier predicted for methanol elimination from the DMMP molecule adsorbed on Mo_3O_8 cluster (70.7 kcal/mol) is only 1.6 kcal/mol lower than in the molecule adsorbed on ideal $(MoO_3)_3$ cluster (72.3 kcal/mol) and 2.8 kcal/mol higher than in gaseous phase (67.5 kcal/mol).

The decomposition of the DMMP molecule adsorbed on a hydroxylated Mo_3O_9H cluster via bond cleavage pathways also requires lower energies than the gaseous phase DMMP or DMMP on an ideal cluster (Table 7.2). The energies of P-OCH_3 (87.6 kcal/mol), P-CH_3 (75.8 kcal/mol), and O-CH_3 (30.7 kcal/mol) bonds cleavage are 8.3, 14.7, and 60.6 kcal/mol lower as compared to a DMMP molecule adsorbed on an ideal cluster. Elimination of methanol via intramolecular hydrogen transfer (Eq. 5, Path 5, Figure 7.7) requires 82.3 kcal/mol, which is 14-17 kcal/mol higher than the activation energies calculated for DMMP in gaseous phase (67.5 kcal/mol), adsorbed on an ideal cluster (72.3 kcal/mol), and adsorbed on a reduced cluster (70.7 kcal/mol).

Unlike the gaseous phase, ideal and reduced clusters, the elimination of methanol from the DMMP molecule adsorbed on a hydroxylated cluster may also proceed via intermolecular hydrogen transfer (Eq. 6, Path 6, Figure 7.7). Our calculations showed that this reaction channel requires the activation energy as low as 23.9 kcal/mol.

The calculated energy of O-CH_3 bond dissociation in the DMMP molecule adsorbed on a $Mo_3O_9H_2$ cluster (20.6 kcal/mol) is 10 kcal/mol lower than that on a Mo_3O_9H cluster (30.7 kcal/mol), whereas the activation barrier of intermolecular methanol elimination (Eq. 6, Path 6, Figure 7.7) is 20 kcal/mol. The intramolecular elimination of methanol requires 71.4 kcal/mol.

7.5 Discussion

7.5.1 Adsorption and Desorption of DMMP on $(MoO_3)_3$

Our results allow us to analyze the adsorption characteristics of DMMP on $(MoO_3)_3$. The XPS results indicated that the initial adsorption of DMMP onto $(MoO_3)_3$ can occur at room temperature. The XPS spectra of the P(2p) region of DMMP on $(MoO_3)_3$ at room temperature already contained partially reduced phosphorus as shown in Figure 7.1(a). Our theory shows that stoichiometric $(MoO_3)_3$ clusters do not decompose DMMP, therefore the presence of partially reduced DMMP at room temperature could be caused by some nonstoichiometric Mo_3O_{9-x} cluster species within the cluster beam, which have the capability to reduce phosphorus. It is interesting to note that each $(MoO_3)_3$ cluster adsorbs about one DMMP molecule, possibly due to steric effects and limited adsorption sites within the clusters. This agrees well with the results of our theoretical modeling, which show that the binding energy of the second DMMP molecule (12.5 kcal/mol) is ~8 kcal/mol lower than that of the first (19.5 kcal/mol).

Experimentally, the decreasing of the P to Mo ratio in XPS upon heating (Figure 7.3) and the TPR results (Figure 7.4) provide some insight into the desorption behavior of

DMMP on these clusters. The TPR profile of both the DMMP parent ion (124 amu) and its major fragment (79 amu) exhibited a desorption peak around 107 ºC. This resulted in a binding energy, as calculated via Redhead Analysis, of about 23.4 kcal/mol (Table 7.1), which is higher than the desorption energy of DMMP from SiO_2 [7]possibly due to the stronger Lewis acidity of $(MoO_3)_3$ clusters. Upon comparing to theory, the desorption energy of DMMP from $(MoO_3)_3$ clusters falls in the range of theoretically calculated values for DMMP desorbed from stoichiometric $(MoO_3)_3$ clusters (32 kcal/mol), Mo_3O_9H clusters (28.6 kcal/mol), $Mo_3O_9H_2$ clusters (19.3-28.1 kcal/mol), and $Mo_3O_9H_3$ clusters (20.4-26.2 kcal/mol), (Figures 5 and 6, Table 7.1). The experimentally determined binding energy is calculated from the center of the DMMP desorption peaks (124 and 79 amu), but when the broadness of the peaks is considered it indicates a range of desorption energies (Figure 7.4). The broad range of desorption energies can be explained by a non-homogenous composition for the deposited clusters.

7.5.2 Decomposition of DMMP on $(MoO_3)_3$

Since the reduction of DMMP was seen on $(MoO_3)_3$ in XPS (Figure 7.2(b)), what are the reaction pathways and the reaction products of DMMP?

The TPR results show the loss of methanol upon heating, which is similar to the case of DMMP on CeO_x. Meanwhile, the reduction of the phosphorus of DMMP on $(MoO_3)_3$ as seen in XPS is consistent with the loss of methoxy group from DMMP (Figure 7.1(b)). However, the desorption energy of methanol from Redhead Analysis of TPR (29.8 kcal/mol) is significantly lower than the calculated activation barrier of methanol elimination from the DMMP molecule adsorbed on the stoichiometric $(MoO_3)_3$ (72.3 kcal/mol) and the non-stoichiometric Mo_3O_8 (70.7 kcal/mol) clusters (Table 7.2).

According to the results of our theoretical modeling, the presence of hydroxyls on the cluster may cause an approximately four-fold reduction of the energy required for methanol elimination (Table 7.2, Figure 7.8). The calculated activation barrier for methanol loss via cluster-to-molecule hydrogen transfer (Eq. 6, Figures 7 and 8) requires 20-24 kcal/mol which is consistent with experimentally estimated activation energy of 29.8 kcal/mol (Table 7.2).

Our results are consistent with earlier results indicating the important role of surface hydroxyls as nucleophiles in methanol elimination from DMMP. [5,30] We also need to note, that although our clusters were prepared by a magnetron sputtering source and were kept in UHV after deposition, it was still possible for the surface residual hydroxyls to influence the reaction behavior.[31] Mild annealing of the sample caused partial reduction of the $(MoO_3)_3$ clusters as seen in XPS (Figure 7.2(b)).

Further inspection of the decomposition energies collected in Table 7.1 revealed that the loss of a methyl group from DMMP seen in the TPR (Figure 7.4) with an activation energy of 29.7 kcal/mol can be explained by O-CH_3 bond cleavage in the DMMP molecule adsorbed on a reduced Mo_3O_8 and $Mo_3O_9H_n$ (n=1,2) clusters. Our calculations determined the decomposition energy of this bond cleavage are 22.1 (Mo_3O_8), 30.7 (Mo_3O_9H) and 20.6 ($Mo_3O_9H_2$) kcal/mol (Table 7.2, Figure 7.8) which is in good agreement with experiment. The calculation results indicate some level of selectivity in the decomposition of DMMP between the different stoichiometries of clusters with the non-stoichiometric Mo_3O_8 cluster preferentially removing a methoxyl methyl group and the Mo_3O_9H cluster preferentially removing an intact methoxy group via methanol elimination, while the $Mo_3O_9H_2$ cluster supports DMMP decomposition along either pathway.

The results of our joint experimental and theoretical study revealed the effect of surface hydroxyl and reducible metal centers on the activation energies of DMMP decomposition. The energies required for methanol and methyl loss from DMMP adsorbed on $Mo_3O_9H_n$ (n=1,2) and Mo_3O_8 clusters are 3-4 times lower compared to the gas phase and decomposition on an ideal stoichiometric cluster.

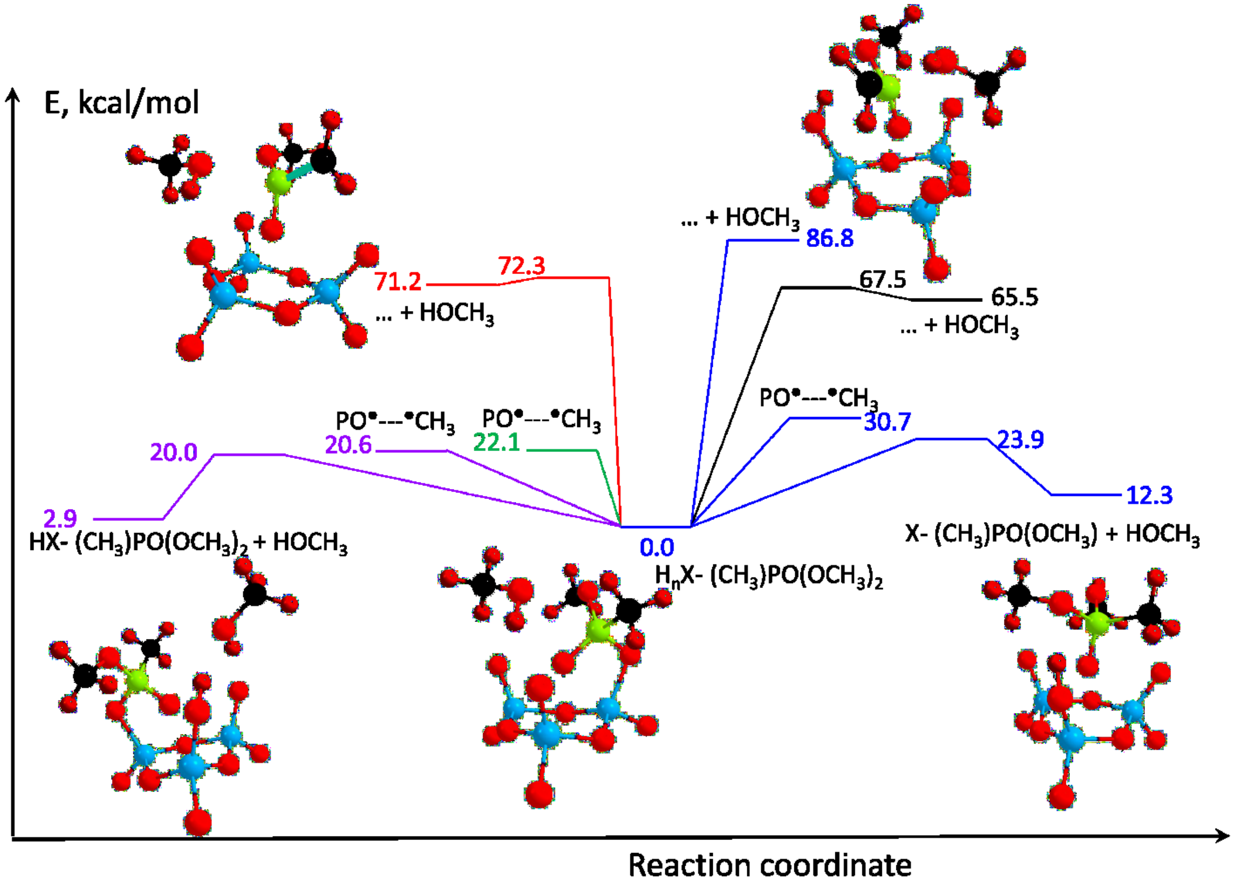

Figure 7.8 Schematic energy diagram for the decomposition of DMMP. Blue lines correspond to decomposition pathways of DMMP adsorbed on a Mo_3O_9H cluster, purple - $Mo_3O_9H_2$, green – Mo_3O_8 cluster, red – $(MoO_3)_3$ cluster, and black – gas phase.

7.6 Conclusion

The adsorption and decomposition behaviors of DMMP on size-selected $(MoO_3)_3$ clusters were studied experimentally by XPS and TPR and theoretically by DFT calculations. The experimental results indicated the decomposition of DMMP on $(MoO_3)_3$ involves the loss of a methoxy group leading to the production of methanol during the reaction, and the experiments provided the measured binding energies that helped validate the theoretical calculations. The theoretical calculations determined that hydroxyl groups on the cluster and partially reduced, non-stoichiometric, clusters had significantly lowered activation barriers for DMMP decomposition, showing the importance of the reducibility of a metal center and the presence of residual hydroxyl groups in metal oxide catalysis.

Acknowledgment

This material is based upon work supported by the Defense Threat Reduction Agency (DTRA) under grant number HDTRA1-15-1-0005

Supporting Information

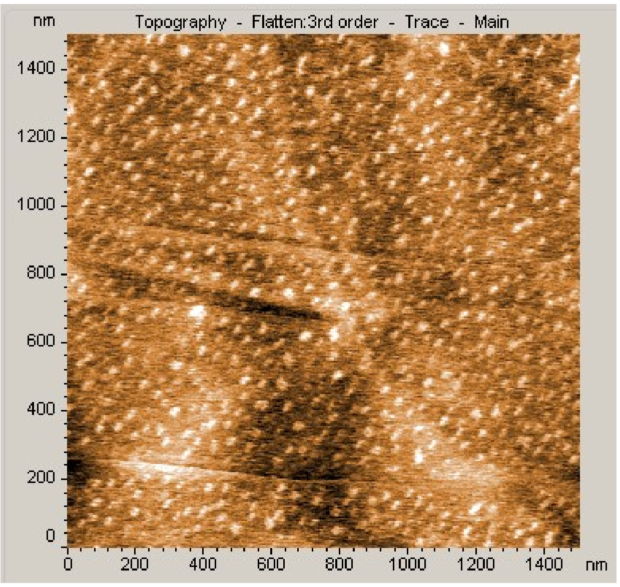

Figure 7.S1 AFM Images of Monodispersed Molybdenum Oxide Clusters

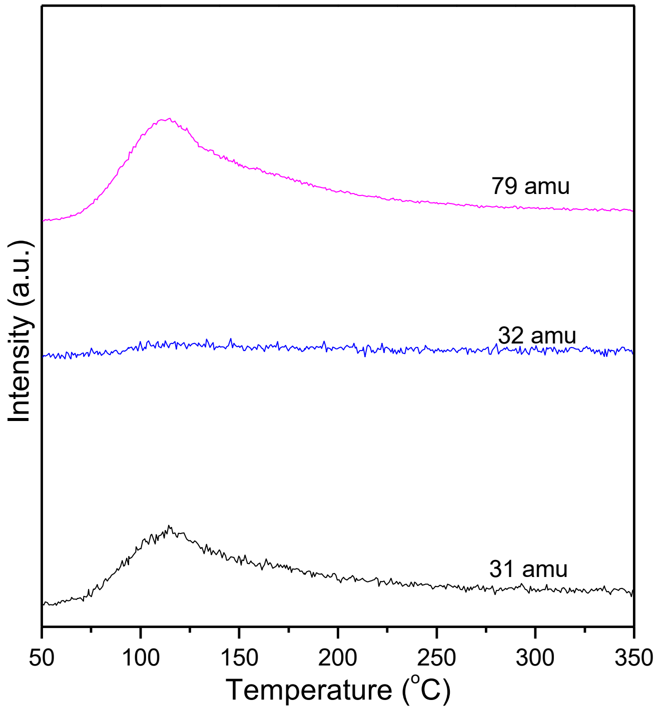

Figure 7.S2 TPD Profiles of DMMP on HOPG

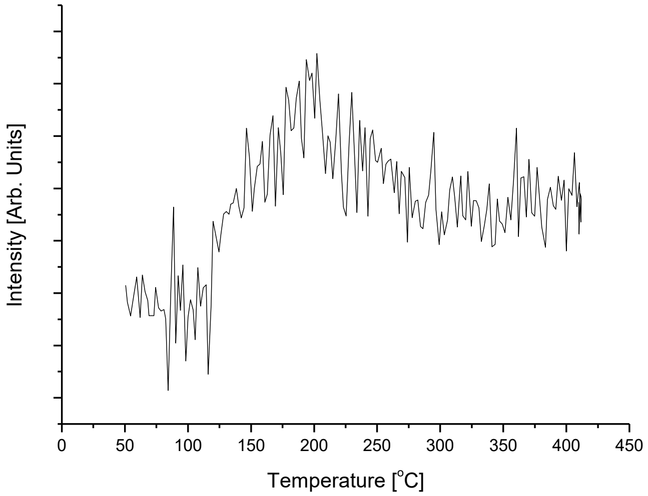

Figure 7.S3 Subtraction of DMMP Contribution from 15 amu

Reference

(1) Kim, K.; Tsay, O. G.; Atwood, D. A.; Churchill, D. G., Chem Rev 2011, 111 (9), 5345-5403.

(2) Yenisoy-Karakas, S.; Aygun, A.; Gunes, M.; Tahtasakal, E., Carbon 2004, 42 (3), 477-484.

(3) Rusu, C. N.; Yates, J. T., J Phys Chem B 2000, 104 (51), 12292-12298.

(4) Aurianblajeni, B.; Boucher, M. M., Langmuir 1989, 5 (1), 170-174.

(5) Mitchell, M. B.; Sheinker, V. N.; Mintz, E. A., J Phys Chem B 1997, 101 (51), 11192-11203.

(6) Chen, D. A.; Ratliff, J. S.; Hu, X. F.; Gordon, W. O.; Senanayake, S. D.; Mullins, D. R., Surf Sci 2010, 604 (5-6), 574-587.

(7) Wilmsmeyer, A. R.; Uzarski, J.; Barrie, P. J.; Morris, J. R., Langmuir 2012, 28 (30), 10962-10967.

(8) Wilmsmeyer, A. R.; Gordon, W. O.; Davis, E. D.; Troya, D.; Mantooth, B. A.; Lalain, T. A.; Morris, J. R., J Phys Chem C 2013, 117 (30), 15685-15697.

(9) Yang, L.; Tunega, D.; Xu, L.; Govind, N.; Sun, R.; Taylor, R.; Lischka, H.; DeJong, W. A.; Hase, W. L., J Phys Chem C 2013, 117 (34), 17613-17622.

(10) Troya, D.; Edwards, A. C.; Morris, J. R.,. J Phys Chem C 2013, 117 (28), 14625-14634.

(11) Taylor, D. E.; Runge, K.; Cory, M. G.; Burns, D. S.; Vasey, J. L.; Hearn, J. D.; Griffith, K.; Henley, M. V., J Phys Chem C 2013, 117 (6), 2699-2708.

(12) Paukku, Y.; Michalkova, A.; Leszczynski, J., J Phys Chem C 2009, 113 (4), 1474-1485.

(13) Hohenberg, P.; Kohn, W., Phys Rev B 1964, 136 (3B), B864-+.

(14) Kohn, W.; Sham, L. J., Phys Rev 1965, 140 (4A), 1133-&.

(15) Becke, A. D., J Chem Phys 1993, 98 (7), 5648-5652.

(16) Lee, C. T.; Yang, W. T.; Parr, R. G., Phys Rev B 1988, 37 (2), 785-789.

(17) Yanai, T.; Tew, D. P.; Handy, N. C., Chem Phys Lett 2004, 393 (1-3), 51-57.

(18) Grimme, S.; Antony, J.; Ehrlich, S.; Krieg, H., J Chem Phys 2010, 132 (15).

(19) Sun, J.; Remsing, R. C.; Zhang, Y.; Sun, Z.; Ruzsinszky, A.; Peng, H.; Yang, Z.; Paul, A.; Waghmare, U.; Wu, X.; Klein, M. L.; Perdew, J. P., Nat Chem 2016, advance online publication.

(20) Sun, J. W.; Ruzsinszky, A.; Perdew, J. P., Phys Rev Lett 2015, 115 (3).

(21) Hay, P. J.; Wadt, W. R., J Chem Phys 1985, 82 (1), 270-283.

(22) Hay, P. J.; Wadt, W. R., J Chem Phys 1985, 82 (1), 299-310.

(23) Wadt, W. R.; Hay, P. J., J Chem Phys 1985, 82 (1), 284-298.

(24) Hratchian, H. P.; Schlegel, H. B., J Chem Phys 2004, 120 (21), 9918-9924.

(25) Hratchian, H. P.; Schlegel, H. B., J Chem Theory Comput 2005, 1 (1), 61-69.

(26) Frisch, M. J.; Trucks, G. W.; Schlegel, H. B.; Scuseria, G. E.; Robb, M. A.; Cheeseman, J. R.; Scalmani, G.; Barone, V.; Mennucci, B.; Petersson, G. A.; Nakatsuji, H.; Caricato, M.; Li, X.; Hratchian, H. P.; Izmaylov, A. F.; Bloino, J.; Zheng, G.; Sonnenberg, J. L.; Hada, M.; Ehara, M.; Toyota, K.; Fukuda, R.; Hasegawa, J.; Ishida, M.; Nakajima, T.; Honda, Y.; Kitao, O.; Nakai, H.; Vreven, T.; Montgomery Jr., J. A.; Peralta, J. E.; Ogliaro, F.; Bearpark, M. J.; Heyd, J.; Brothers, E. N.; Kudin, K. N.; Staroverov, V. N.; Kobayashi, R.; Normand, J.; Raghavachari, K.; Rendell, A. P.; Burant, J. C.; Iyengar, S. S.; Tomasi, J.; Cossi, M.; Rega, N.; Millam, N. J.; Klene, M.; Knox, J. E.; Cross, J. B.; Bakken, V.; Adamo, C.; Jaramillo, J.; Gomperts, R.; Stratmann, R. E.; Yazyev, O.; Austin, A. J.; Cammi, R.; Pomelli, C.; Ochterski, J. W.; Martin, R. L.; Morokuma, K.; Zakrzewski, V. G.; Voth, G. A.; Salvador, P.; Dannenberg, J. J.; Dapprich, S.; Daniels, A. D.; Farkas, Ö.; Foresman, J. B.; Ortiz, J. V.; Cioslowski, J.; Fox, D. J. Gaussian 09, Gaussian, Inc.: Wallingford, CT, USA, 2009.

(27) Frisch, M. J.; Trucks, G. W.; Schlegel, H. B.; Scuseria, G. E.; Robb, M. A.; Cheeseman, J. R.; J. A. Montgomery, J.; Vreven, T.; Kudin, K. N.; Burant, J. C.; Millam, J. M.; Iyengar, S. S.; Tomasi, J.; Barone, V.; Mennucci, B.; Cossi, M.; Scalmani, G.; Rega, N.; Petersson, G. A.; Nakatsuji, H.; Hada, M.; Ehara, M.; Toyota, K.; Fukuda, R.; Hasegawa, J.; Ishida, M.; Nakajima, T.; Honda, Y.; Kitao, O.; Nakai, H.; Klene, M.; Li, X.; Knox, J. E.; Hratchian, H. P.; Cross, J. B.; Bakken, V.; Adamo, C.; Jaramillo, J.; Gomperts, R.; Stratmann, R. E.; Yazyev, O.; Austin, A. J.; Cammi, R.; Pomelli, C.; Ochterski, J. W.; Ayala, P. Y.; Morokuma, K.; Voth, G. A.; Salvador, P.; Dannenberg, J.

J.; Zakrzewski, V. G.; Dapprich, S.; Daniels, A. D.; Strain, M. C.; Farkas, O.; Malick, D. K.; Rabuck, A. D.; Raghavachari, K.; Foresman, J. B.; Ortiz, J. V.; Cui, Q.; Baboul, A. G.; Clifford, S.; Cioslowski, J.; Stefanov, B. B.; Liu, G.; Liashenko, A.; Piskorz, P.; Komaromi, I.; Martin, R. L.; Fox, D. J.; Keith, T.; Al-Laham, M. A.; Peng, C. Y.; Nanayakkara, A.; Challacombe, M.; Gill, P. M. W.; Johnson, B.; Chen, W.; Wong, M. W.; Gonzalez, C.; Pople, J. A. Gaussian 03, Revision D.02, Gaussian, Inc.: Wallingford CT, USA, 2004.

(28) Li, X.; Wepasnick, K. A.; Tang, X.; Wang, Y.; Bowen, K. H.; Fairbrother, D. H.; Gantefoer, G., J Vac Sci Technol B 2012, 30, 031806.

(29) Falconer, J. L.; Schwarz, J. A., Catal Rev 1983, 25 (2), 141-227.

(30) Head, A. R.; Tsyshevsky, R.; Trotochaud, L.; Yu, Y.; Kyhl, L.; Karshoglu, O.; Kuklja, M. M.; Bluhm, H., submitted.

(31) Liang, S. Y.; Hemberger, P.; Neisius, N. M.; Bodi, A.; Grutzmacher, H.; Levalois-Grutzmacher, J.; Gaan, S., Chem-Eur J 2015, 21 (3), 1073-1080.

8. Decomposition Behavior of DMMP on Cu and CuO Clusters

8.1 Introduction

The surface chemistry of organic phosphonate is critical to the adsorption and decomposition of organophosphorus chemical warfare agents[1]. Dimethyl methylphosphonate (DMMP) is widely used as a simulant for chemical warfare agents, due to its structural similarity to many nerve agents and its low toxicity.

The fate of DMMP on the surfaces of metal oxides was found to heavily depend on the nature of the oxides. Two possible non-dissociative adsorption mechanisms exist for DMMP on metal oxides[2]: adsorption via Lewis acid sites, i.e. metal ion centers, or Brønsted acid sites, i.e. hydroxyl groups. Dissociative adsorption can take place by a nucleophilic attack of the phosphorus atom to form bridge oxygen bound methyl methylphosphonate(MMP).[3] Further loss of methoxy groups is also possible, as observed on TiO_2 [3] and CeO_2 [4] oxides at elevated temperature. In many cases, these methoxides can produce either methanol[4] or ether[5] depending on the acidity of the oxides. It has to be noted that, in addition of the hydrolysis reaction mentioned above, the redox reactions can take place when oxygen defects are present. This usually happens on the oxides with a reducible metal center.[3]

In addition to many metal oxides studied, supported metal nanoparticles have also been used to decompose DMMP. In contrast to metal oxides, metal nanoparticles, such as Cu[6], Ni[7], can break both the P-O and P-C bond in DMMP, which can lead to the formation of atomic phosphorous species on surface.

In current study, we presented a general picture of DMMP decomposition pathways on metal and metal oxide clusters. The oxidation states of metal ions were varied while the corresponding reaction products for DMMP were studied accordingly. X-ray photoelectron spectra (XPS) and temperature programmed reaction(TPR) were used to study the reaction products of DMMP.

8.2 Experimental Methods

Copper and copper oxides clusters were prepared as anions by a magnetron sputtering source in our cluster deposition apparatus. The copper metal clusters were produced by sputtering of copper target with a mixture of argon and helium gas. Metal oxide clusters were produced by introducing oxygen gas into the sputtering and transport gas. Typically, the metal target is biased to -500V and the argon gas introduced is ionized and then bombards the metal target surface to create copper atoms and electrons. The helium gas serves to cool the copper atoms to facilitate the formations of clusters and also transport the as formed clusters downstream, where they were then electrostatically accelerated before entering a magnetic sector mass spectrometer (25° sector magnet with resolution of $m/\Delta m = 20$). By tuning the magnetic field strength, the cluster anions were mass-selected and focused by ion optics before entering the deposition chamber, where they were soft-landed (<1eV) onto a freshly peeled HOPG surface. The resulting sample can be cooled to approximately -170ºC by liquid nitrogen (LN_2) or heated via resistive heating by passing current through the HOPG, with the temperature of the sample being monitored by a K-type thermocouple spring loaded to the back of the HOPG.

For a better comparison of the reactivity of the clusters, the same size of the clusters was chosen for all clusters, i.e. ~6400 amu. A TPR set-up, consisted of a Hiden HAL/3F PIC quadrupole mass spectrometer (QMS) mounted on a linear translator and covered in a glass shroud, allows for the characterization of their activity of the as-deposited clusters.

In addition, deposited samples could also be transferred *in situ* to an adjacent UHV chamber with a different sample holder, where they were characterized by X-ray Photoelectron Spectroscopy (*in situ* XPS) with non-monochromatic Mg Kα-rays (1253.6 eV), with the ejected electron kinetic energy analyzed via a high energy hemispherical analyzer. The sample can be *in situ* heated by e-beam heating with the temperature measured by a K type thermocouple connected to the sample holder.

In the TPR experiment, 1 langmuirs of DMMP was pre-dosed onto a clean-cleaved HOPG surface cooled to -173 ºC via a leak valve. A physisorbed layer of DMMP on HOPG surface was formed. After that, 2.5×10^{12} copper or copper oxide clusters with a size of 6400 amu were deposited into the physisorbed layers of DMMP. This sequence is used since the preformed DMMP matrix may help to stabilize the small clusters After the cluster deposition, the surface temperature is first raised to desorb the vast majority of physisorbed DMMP, and then ramped to 450 ºC with a ramping rate of 2 ºC/s. In the XPS studies, a higher pressure of DMMP (5×10^{-7} torr) was dosed during deposition in order to saturate the adsorption sites on the clusters surface. In both cases the DMMP was purified by several freeze-pump-thaw cycles before being background dosed through a UHV compatible leak valve.

8.3 Experimental Results and Discussions

8.3.1 XPS Results of DMMP on Cu, CuO_x, CuO

The XPS spectra of P(2p) regions of DMMP on Cu, CuO_x and CuO at room temperature are shown in Figure 8.1. As indicated from the XPS spectra, the P(2p) regions of DMMP exhibited different spectral envelopes for the three different clusters. For CuO clusters, only a P(2p) peak with a high binding energy was observed. This peak is typical for DMMP on metal oxide surface, and usually assigned to the hydrolysis products of DMMP on oxides, i.e. MMP. Therefore, a similar peak also appears for CuO_x at higher binding energy. In addition to the high binding energy peak, an additional peak appears at lower binding energy for CuO_x. According to the studies from Chen[8], this is assigned to the fully reduced phosphorus species, i.e. Cu-P. This low binding energy P(2p) peak is more dominant when DMMP reacts with pure copper clusters, highlighted by a major peak at the lower binding energy. It should be noted that Chen also observed this peak for DMMP on copper nanoparticles, however, at much high temperature(~700K). Given the copper clusters produced in this study is much smaller than the one from Chen (>1000 atoms), there is a much lower reaction barrier for producing atomic phosphorus for the as-prepared copper clusters in this size range.

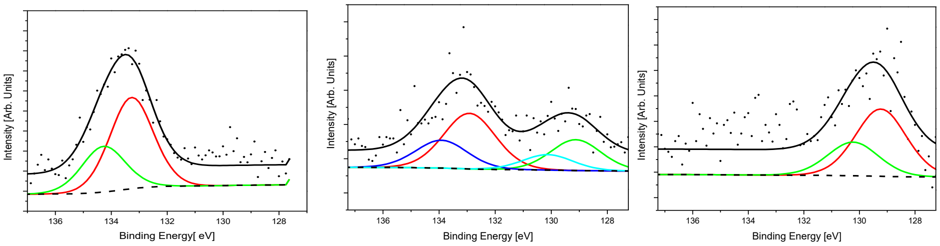

Figure 8.1 P(2p) Regions of DMMP on CuO, CuO_x, and Cu Clusters (from left to right)

8.3.2 TPD Results of DMMP on Cu and CuO

TPD is used to study the reaction products of DMMP on Cu and CuO clusters. Before TPD, for Cu clusters, the sample temperature was first raised to 50 ºC, while for CuO clusters, the sample temperature was first raised to 0 ºC due to the lower onset of DMMP desorption temperature.

It is suggested from XPS results that the reaction between DMMP and CuO clusters may lead to the formation of methoxides on the cluster surface. Similar methoxide intermediates are also suggested from the study from Chen on large copper nanoparticles. 6

For TPD study of DMMP on Cu and CuO, various products at different masses were monitored in order to determine the possible reaction pathways. For DMMP on both pure copper clusters and copper oxide clusters, the desorption of intact DMMP was observed. In addition to DMMP, the major reaction products observed are methane, methanol and formaldehyde.

Specifically, for DMMP on pure Cu clusters, methanol desorbed from the clusters around 190 ºC. Meanwhile, formaldehyde shows two different desorption peaks: the first one is at a similar temperature to that from methanol, and the second one is at significantly higher temperature, i.e. 278 ºC. In addition, methane desorbed from the clusters with a peak at 265 ºC.

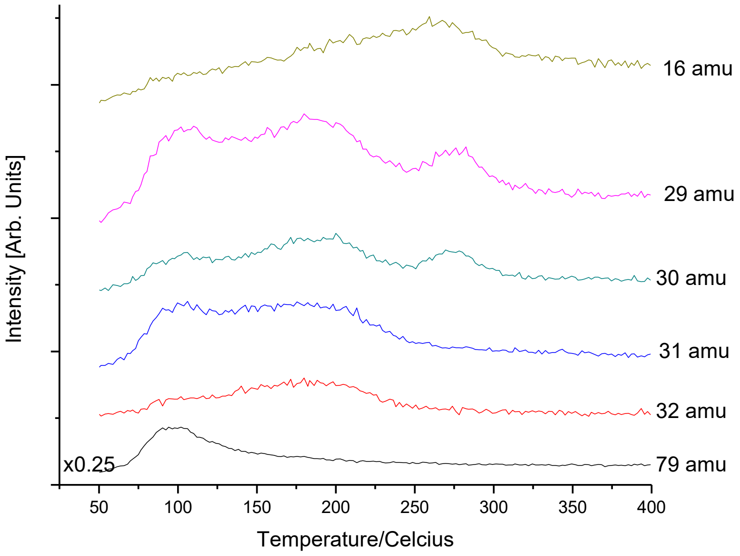

Figure 8.2 TPD Profiles of DMMP on Cu Clusters

For DMMP on CuO clusters, methane desorbed at the same temperature as it did from metal clusters. The desorption of methanol happens at higher temperature(241ºC) compared to that on Cu clusters. This shows a higher reaction barrier for producing methanol for DMMP on CuO compared to Cu clusters. Different from Cu clusters, there is one broad desorption peak of formaldehyde on CuO clusters. Part of the peak is overlapping with the desorption of methanol, similar to the case in Cu clusters. The higher shoulder of that peak position is identical to the position of the second desorption peak of formaldehyde on Cu clusters. Therefore this broad desorption peak of the formaldehyde is likely a convolution of two peaks: a low temperature desorption peak at the similar temperature of methanol desorption and a higher desorption temperature. Possibly, a similar reaction mechanism may exist for the methane production and the formaldehyde formation between two clusters.

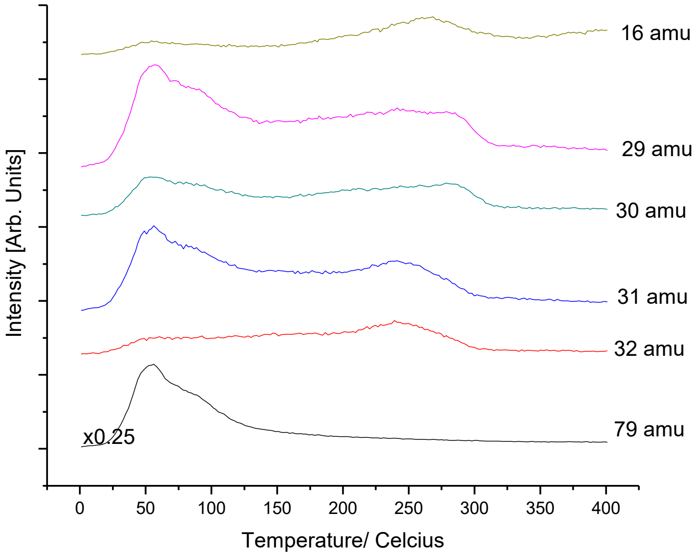

Figure 8.3 TPD Profiles of DMMP on CuO Clusters

8.4 Discussions

Both XPS and TPD highlighted the different decomposition behaviors of DMMP on copper-based clusters with different oxygen contents. As indicated in XPS studies, the more metallic copper there is, the more reduction of phosphorus is observed in the P(2p) regions. The extent of reduction of phosphorus has to do with the reducibility of metal center within the clusters. For metallic copper, more valance electrons can be used to reduce DMMP, and eventually fully decompose DMMP to form atomic phosphorus. For CuO, only a hydrolysis reaction can take place due to the limited availability of valence electrons provided.

TPD of DMMP on Cu, and CuO both revealed methanol, formaldehyde and methane as the desorption products. However, different desorption features were observed. Compared to DMMP on CuO, DMMP on copper has a lower desorption peak for both formaldehyde and methanol. Methoxides are usually considered as a reaction intermediate for both of production of methanol and formaldehyde.[5] Similar reaction intermediates are also proposed by Chen.[6] Since both methanol and formaldehyde are produced at lower temperature, copper clusters may have a lower reaction barrier for producing methoxide intermediates. This is not surprising given the XPS results indicated that the copper clusters are more reactive in the decomposition process of DMMP. It is also known that methoxides form upon the nucleophilic attack from the base group on surface.[5] Copper clusters are probably the better base compared to copper oxides due to its low valency, therefore, copper clusters are likely to promote this process. Despite of the above difference, the methane desorption and high temperature formaldehyde desorption happens at the same temperature on both copper and copper oxide clusters. This suggests a similar pathway for methane formation and high temperature formaldehyde formation at these two clusters. It is possible that P-CH_3 cleavage may lead to the formation of methane but further evidence is needed to support this.

8.5 Conclusions

Decompositions of DMMP were studied on Cu, CuO_x, CuO cluster surface. Different degree of oxidation of copper is found to significantly affect the reaction products, both on the surface and in the gas phase. XPS results shows that copper clusters can cause the full reduction of phosphorus while CuO clusters mostly induce the hydrolysis of DMMP. A lower reaction barrier to the formation of methoxide intermediates are also proposed for copper clusters.

Acknowledgment

This material is based upon work supported by the Defense Threat Reduction Agency (DTRA) under grant number HDTRA1-15-1-0005

References

(1) Yang, Y. C.; Baker, J. A.; Ward, J. R. Chemical Reviews 1992, 92, 1729.

(2) Templeton, M. K.; Weinberg, W. H. J Am Chem Soc 1985, 107, 97.

(3) Panayotov, D. A.; Morris, J. R. Langmuir 2009, 25, 3652.

(4) Chen, D. A.; Ratliff, J. S.; Hu, X.; Gordon, W. O.; Senanayake, S. D.; Mullins, D. R. Surf Sci 2010, 604, 574.

(5) Mitchell, M. B.; Sheinker, V. N.; Cox, W. W.; Gatimu, E. N.; Tesfamichael, A. B. The Journal of Physical Chemistry B 2004, 108, 1634.

(6) Ma, S.; Zhou, J.; Kang, Y. C.; Reddic, J. E.; Chen, D. A. Langmuir 2004, 20, 9686.

(7) Zhou, J.; Ma, S.; Kang, Y. C.; Chen, D. A. The Journal of Physical Chemistry B 2004, 108, 11633.

(8) Ma, S.; Zhou, J.; Kang, Y. C.; Reddic, J. E.; Chen, D. A. Langmuir 2004, 20, 9686.

9. Decomposition of DMMP on $(WO_3)_3$ and $(ZrO_2)_3$ clusters

9.1 Introduction

The surface chemistry of chemical warfare agent is of critical importance to the design of sensor to detect chemical warfare agents and sorbent to decontaminate them.[1] Organophosphorus compounds are commonly used as chemical warfare agents.[2] Therefore, the adsorption and decomposition behaviors of organic phosphate are widely studied by many research groups.[3-7] Of all the organic phosphates, dimethyl methylphosphate(DMMP) has attracted much attention since it has a similar structure to many nerve agents but much lower toxicity. Thus DMMP is used as structural simulants in many related studies.

By using DMMP as a model system, the reactivity of many metals and metal oxides have been studied.[8,9] As shown in those studies, DMMP undergoes step-wise loss of methoxy group due to nucleophilic attack from functional groups on oxide surface. Methanol is observed as common reaction products on many oxides.[10] In addition to the hydrolysis reaction observed, reduction processes are also observed when surface defects, i.e. oxygen vacancies are present[11,12]. Overall, both the acidity and reducibility of metal oxides are known to affect the decomposition pathway of DMMP.

In this study, we compared the decomposition pathway of DMMP on two different oxide clusters, $(WO_3)_3$ and $(ZrO_2)_3$. These two clusters are chosen because they have different acidity as well as different reducibility. Although the decomposition of DMMP on both bulk WO_3 [13,14]and ZrO_2 [15,16]have been studied, there is a lack of detailed understanding on the interaction between DMMP and small oxide clusters in a well-controlled fashion.

9.2 Experimental Methods

$(WO_3)_3$ and $(ZrO_2)_3$ were prepared as anions by a magnetron sputtering source in our cluster deposition apparatus described elsewhere. The metal oxide clusters were produced by reactive sputtering of tungsten and zirconium target with a mixture of argon, helium and oxygen gas. The as-produced clusters were then electrostatically extracted and then into magnetic sector mass spectrometer (25° sector magnet with resolution of $m/\Delta m = 20$). By tuning the magnetic field strength, the cluster anions were mass-selected and focused by ion optics before entering the deposition chamber, where they were soft-landed (<1eV) onto a freshly peeled HOPG surface. The resulting sample can be cooled to approximately -170ºC by liquid nitrogen (LN_2) or heated via resistive heating by passing current through the HOPG, with the temperature of the sample being monitored by a K-type thermocouple spring loaded to the back of the HOPG. A TPR set-up, consisting of a Hiden HAL/3F PIC quadrupole mass spectrometer (QMS) mounted on a linear translator and a glass shroud was used to characterize the activity of the as-deposited clusters. In addition, deposited samples could also be transferred *in situ* to an adjacent UHV chamber, where they were characterized by X-ray Photoelectron Spectroscopy (*in situ* XPS) with non-monochromatic Mg Kα-rays (1253.6 eV), with the ejected electron kinetic energy analyzed via a high energy hemispherical analyzer.

In the TPR experiment, 1 Langmuir of DMMP was pre-dosed onto clean-cleaved HOPG surface cooled at -173 ºC via leak valve to from a physisorbed layer of DMMP on HOPG surface. After that, 6×10^{12} oxide clusters were deposited into the physisorbed layers of DMMP. This sequence is used since the pre-formed DMMP matrix may help to stabilize the small clusters. After cluster deposition, the surface temperature is first raised to 50 ºC desorb the vast majority of physisorbed DMMP, and then ramped to 400 ºC with a ramping rate of 2 ºC/s. In the XPS studies, a higher pressure of DMMP (5×10^{-7} torr) was dosed during deposition in order to saturate the adsorption sites on the clusters surface at room temperature. Co-deposition of DMMP and the clusters resulted in enough signal intensity for P(2p) weak. In both cases the DMMP was purified by several freeze-pump-thaw cycles before being background dosed through a UHV compatible leak valve.

9.3 Experimental Results and Discussions

9.3.1 XPS results of DMMP on $(WO_3)_3$ and $(ZrO_2)_3$

The XPS spectra of P(2p) of DMMP on $(WO_3)_3$ and $(ZrO_2)_3$ are shown in the Figure 9.1 and Figure 9.2. One of the major difference between two oxide clusters is that P(2p) peak shift to lower binding energy for $(WO_3)_3$ while for $(ZrO_2)_3$ the P(2p) peak stays unchanged regardless the annealing temperature. This shift to lower binding energy of P(2p) indicated that phosphorus undergoes reduction on $(WO_3)_3$ clusters during heating.

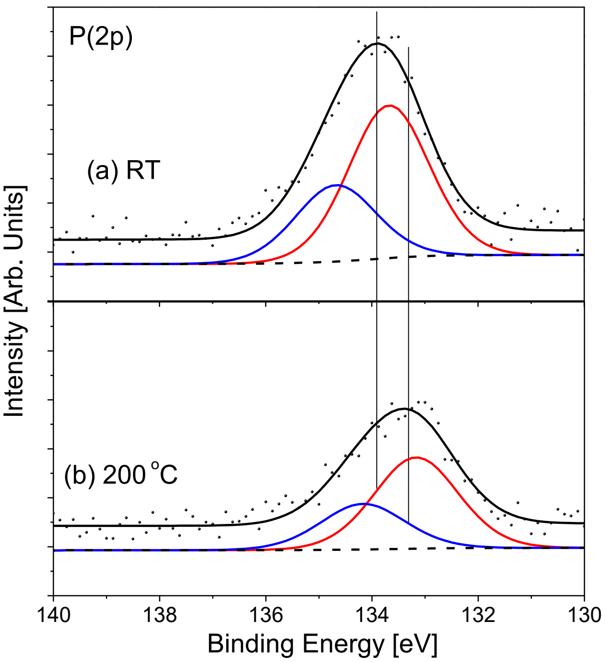

Figure 9.1 P(2p) Regions of DMMP on $(WO_3)_3$ Clusters: (a) RT (b)200 °C

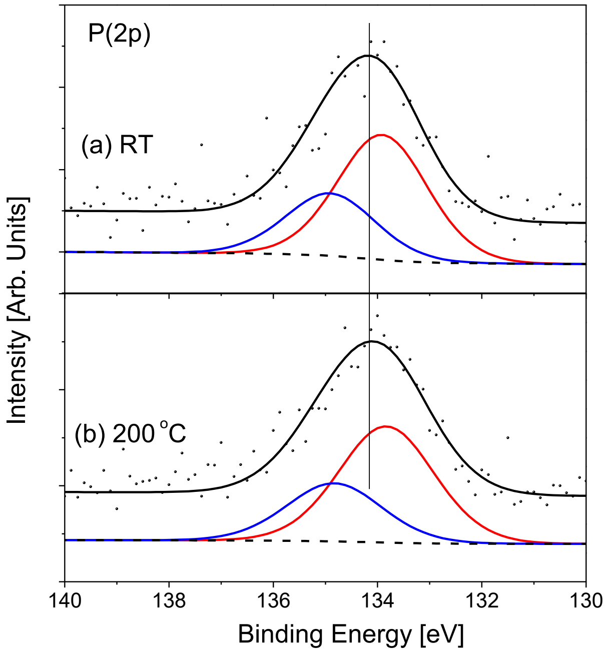

Figure 9.2 P(2p) Regions of DMMP on $(ZrO_2)_3$ Clusters: (a) RT (b)200 °C

Additionally, during heating, tungsten oxides were also reduced as indicated by the downshift of W(4f) peak while ZrO_2 stayed at the same oxidation states as evident from the Zr(3d) XPS spectra. It is known from previous studies on TiO_2, the annealing process will introduce the defects on metal oxide surfaces, which are essentially the active sites for reducing phosphorus.[4] It is likely to be the same case for $(WO_3)_3$ clusters since the reduction of phosphorus is synchronized with the reduction of tungsten. While for $(ZrO_2)_3$, neither the reduction of phosphorus nor the reduction of zirconium is observed upon heating.

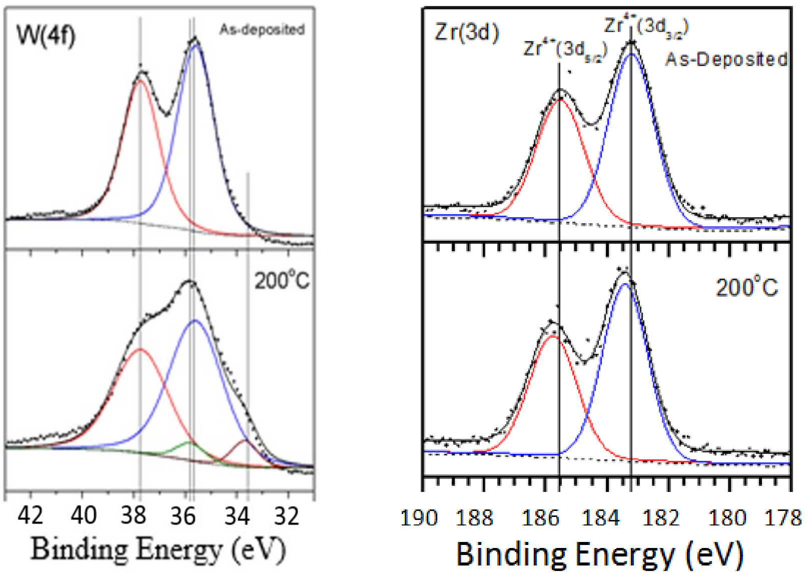
(a) W(4f)

(b) Zr(3d)

Figure 9.3 Annealing Effect on W(4f) and Zr(3d)

The loading of DMMP per metal atom as a function of annealing temperature was also calculated and displayed in the Figure 9.4. As shown in the plot, for DMMP on $(WO_3)_3$, upon heating, the vast majority of DMMP desorbed, while for $(ZrO_2)_2$, DMMP still binds to the clusters. It is known from theoretical calculations that DMMP strongly binds to

ZrO_2,[17] therefore the reaction products are extremely difficult to remove from the surface. The similar products may also exist in our case, resulting in a high loading of DMMP even at higher temperature.

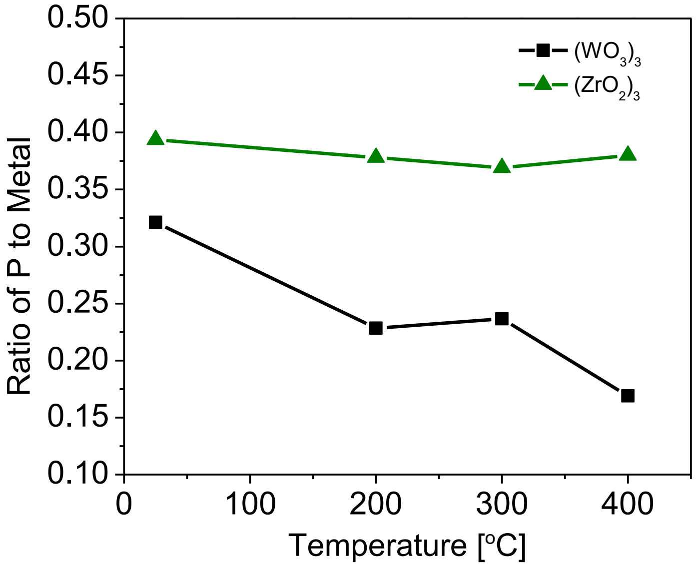

Figure 9.4 Ratio of P to Metal as a function of temperature

9.3.2 TPD of DMMP on $(WO_3)_3$

The TPD results of DMMP desorbed from $(WO_3)_3$ are shown in the Figure 5. The intact DMMP is observed to desorb at lower temperature. Meanwhile, methanol and ether were also observed as major reaction products at higher temperatures. It is suggested by many studies that methoxides are intermediates that lead to the formation of methanol.[18] The interaction between methoxide and surface hydroxyls will result in the desorption of methanol. Solid acid catalysts are known to facilitate the dehydration reaction of methanol to the formation of ether as shown in many studies.[19] Indeed, $(WO_3)_3$ is a strong Lewis acid.[20] This is consistent with the desorption of ether observed in our TPD study.

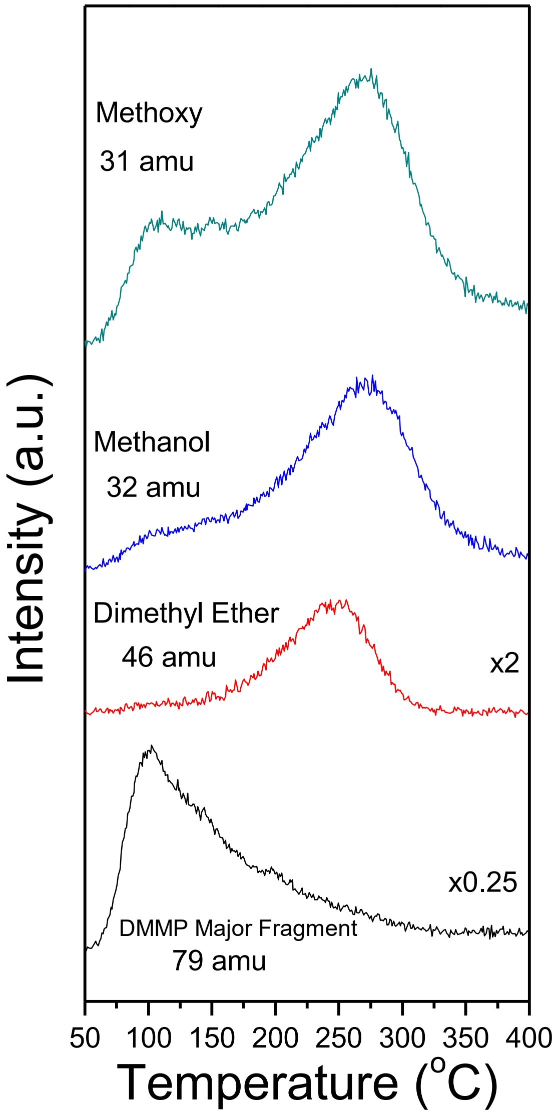

Figure 9.5 TPD Profiles of DMMP on $(WO_3)_3$

9.3.3 $(ZrO_2)_3$ vs. $(WO_3)_3$

Different reaction products of DMMP were observed on the two clusters. To an extent, the reaction properties of DMMP on the clusters are similar to that in the bulk. Both of the oxides can cause hydrolysis reactions of DMMP on oxide surface[21]. As shown in TPD, the

Lewis acidity of $(WO_3)_3$ leads to the formation of ether. In addition to that, $(WO_3)_3$ itself provides the reducibility within metal center. While it gets reduced, it can promote the redox reductions of DMMP presented as the shift of P(2p) peak to lower binding energy in the study. Last, different binding abilities were observed for two oxide clusters. A strongly bonded product was formed on $(ZrO_2)_3$ compared to $(WO_3)_3$. From a practical stand point of view, this is detrimental to use the oxides clusters as catalysts since the residual phosphorus species left on $(ZrO_2)_3$ can block the active sites for the adsorption and decomposition of DMMP.

9.4 Conclusions

Different decomposition pathways and products of DMMP were observed on two different metal oxide clusters. In addition to the hydrolysis reaction products, $(WO_3)_3$ can further reduce DMMP due to redox nature. Furthermore, the relatively weak binding of reaction products to $(WO_3)_3$ can provide a possibility of using $(WO_3)_3$ clusters as a catalyst to decompose DMMP or similar organophosphorus chemical agents.

Acknowledgment

This material is based upon work supported by the Defense Threat Reduction Agency (DTRA) under grant number HDTRA1-15-1-0005

References

(1) Yang, Y. C.; Baker, J. A.; Ward, J. R. Chemical Reviews 1992, 92, 1729.

(2) Korobeinichev, O. P.; Ilyin, S. B.; Bolshova, T. A.; Shvartsberg, V. M.; Chernov, A. A. Combust Flame 2000, 121, 593.

(3) Wilmsmeyer, A. R.; Uzarski, J.; Barrie, P. J.; Morris, J. R. Langmuir 2012, 28, 10962.

(4) Panayotov, D. A.; Morris, J. R. Langmuir 2009, 25, 3652.

(5) Ferguson-McPherson, M. K.; Low, E. R.; Esker, A. R.; Morris, J. R. J Phys Chem B 2005, 109, 18914.

(6) Ratliff, J. S.; Tenney, S. A.; Hu, X.; Conner, S. F.; Ma, S.; Chen, D. A. Langmuir 2009, 25, 216.

(7) Ma, S.; Zhou, J.; Kang, Y. C.; Reddic, J. E.; Chen, D. A. Langmuir 2004, 20, 9686.

(8) Mitchell, M. B.; Sheinker, V. N.; Mintz, E. A. The Journal of Physical Chemistry B 1997, 101, 11192.

(9) Rusu, C. N.; Yates, J. T. The Journal of Physical Chemistry B 2000, 104, 12292.

(10) Trubitsyn, D. A.; Vorontsov, A. V. J Phys Chem B 2005, 109, 21884.

(11) Gordon, W. O.; Tissue, B. M.; Morris, J. R. The Journal of Physical Chemistry C 2007, 111, 3233.

(12) Panayotov, D. A.; Morris, J. R. Langmuir 2009, 25, 3652.

(13) Kanan, S. M.; Lu, Z.; Tripp, C. P. The Journal of Physical Chemistry B 2002, 106, 9576.

(14) Lu, Z.; Kanan, S. M.; Tripp, C. P. J Mater Chem 2002, 12, 983.

(15) Mattsson, A.; Lejon, C.; Štengl, V.; Bakardjieva, S.; Opluštil, F.; Andersson, P. O.; Österlund, L. Applied Catalysis B: Environmental 2009, 92, 401.

(16) Verma, M.; Chandra, R.; Gupta, V. K. Journal of Environmental Chemical Engineering 2016, 4, 219.

(17) Siu, E., Arizona State University, 2011.

(18) Mitchell, M. B.; Sheinker, V. N.; Cox, W. W.; Gatimu, E. N.; Tesfamichael, A. B. The Journal of Physical Chemistry B 2004, 108, 1634.

(19) Yaripour, F.; Baghaei, F.; Schmidt, I.; Perregaard, J. Catalysis Communications 2005, 6, 147.

(20) Li, S.; Dixon, D. A. The Journal of Physical Chemistry A 2006, 110, 6231.

(21) López-Maya, E.; Montoro, C.; Rodríguez-Albelo, L. M.; Aznar Cervantes, S. D.; Lozano-Pérez, A. A.; Cenís, J. L.; Barea, E.; Navarro, J. A. R. Angewandte Chemie 2015, 127, 6894.

10. Reactivity of the Ligated Aluminum Clusters

10.1. $Li_2Al_3(PPh_2)_6$ toward Oxygen

10.1.1 Introduction

Ligated molecular aluminum clusters are of great interest for use in solid rocket propellants, due to their potential ability to lower the ignition threshold relative to pure aluminum nanoparticles.[1-5] On the surface of the ligated molecular aluminum cluster, there is a protective organic ligand layer which serves to kinetically stabilize the cluster.[5] The presence of the ligand layer replaces the oxide layer in aluminum metal nanoparticles, decreasing the diffusion barrier required for the fuel ignition.

However, there is a lack of understanding of how the ligated aluminum clusters react with oxygen. [5] Specifically, it's unknown if oxygen will react with the aluminum core or the surface ligand layer during combustion. It has been shown that monomeric aluminum (I) compounds in solution react with oxygen at the aluminum center at low temperatures.[6] Previous calculations by Hooper found that oxygen reacts preferentially with the aluminum core of $Al_{50}Cp^*_{20}$ rather than with its ligand overcoat.[5] This prediction was good news, since it implies that the initial combustion energy will not be wasted by burning the ligands. In addition, the predicted loss of surface ligand group will result in the exposure of the aluminum core to react with the incoming oxygen molecules.[5]

In the present work, we have conducted temperature programmed reaction (TPR) and x-ray photoelectron spectroscopic (XPS) studies of the thermal decomposition/reaction of a molecular aluminum cluster, providing the experimental evidence to support Hooper's predictions. $Li_2Al_3(PPh_2)_6$ was placed on a carbon tape surface and reacted with O_2 under ultra-high vacuum (UHV) conditions. When the gaseous products were analyzed by TPR none of the evolved ligand fragments showed evidence of oxidation, and when the residual solid film was analyzed by XPS, the observed aluminum had been oxidized.

10.1.2 Experimental Methods

The $Li_2Al_3(PPh_2)_6$ sample was synthesized by the Eichhorn Group, and the detail of the synthetic methods are described elsewhere[7]. A home-made vacuum suitcase was employed to introduce the air-sensitive sample to UHV environment. The suitcase has a special differential-pumped-double-sealed design, which ensured an oxygen-free environment during the transfer process and also enables rotational/ translational motion of the sample in vacuum. (A piece of fresh-cut sodium was added as a sacrificial oxygen trap during the transfer process.) The $Li_2Al_3(PPh_2)_6$ powder was loaded onto a tantalum sample plate (affixed to the plate with carbon tape) in a glove box and subsequently transferred to a UHV set-up by the aforementioned vacuum suitcase. Once the sample was in the UHV environment, a TPR set-up implemented with a Hiden HAL/3F PIC quadruple mass spectrometer (QMS) was used to characterize the reactivity of the sample. The sample was heated by a tungsten filament behind the sample and the temperature of the sample was monitored by a K-type thermocouple attached to the sample holder. A temperature ramping rate of 5 °C/min was adopted. The reaction products that desorbed from the surface were measured by QMS with a glass shroud in front of the ionizer. The post-reaction sample was then characterized by ex situ XPS to investigate the oxidation states of the products.

10.1.3 Results and Discussions

A. TPR on $Li_2Al_3(PPh_2)_6$

Figure 10.1 shows the solid state x-ray crystal structure of $Li_2Al_3(PPh_2)_6$. The cluster consisted of a three-atom-aluminum core surrounded by six PPh_2 ligands. The two lithium cations are on the opposite sides of the triangular plane of three aluminum atoms. The bulky PPh_2 ligands are connected to the metal atoms through their phosphorus binding sites.

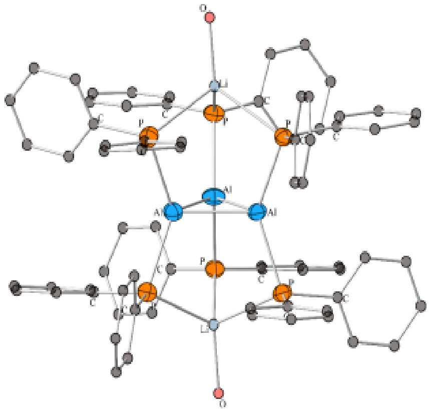

Figure 10.1 Solid state x-ray crystal structure of $Li_2Al_3(PPh_2)_6$.

Figure 10.2 presents the variable-temperature TPR spectra of $Li_2Al_3(PPh_2)_6$ generated upon exposure of the solid to an oxygen atmosphere of $1x10^{-5}$ torr from 27 °C to 97 °C with a ramping rate of 5 °C/min. The major product peaks are labeled and assigned referring to previous mass spectroscopic study on triphenylphosphine [8].

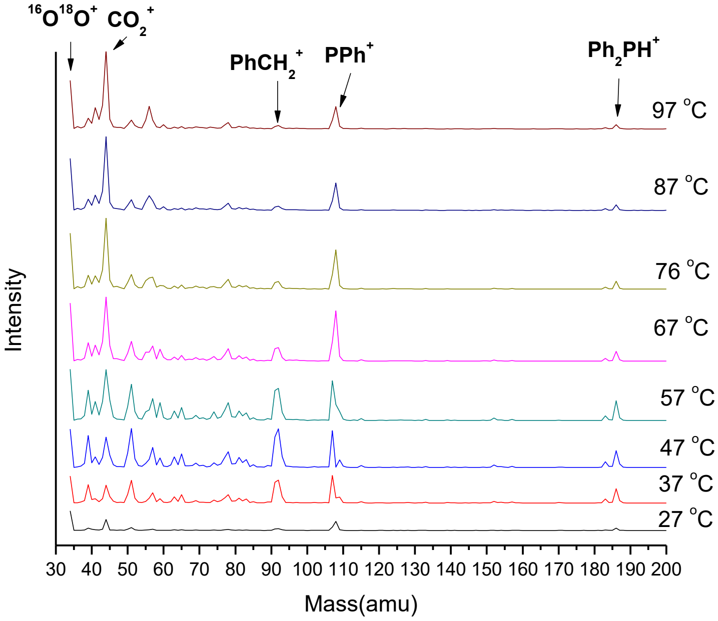

Figure 10.2 The variable-temperature TPR spectra of $Li_2Al_3(PPh_2)_6$ generated upon exposure of the solid to an oxygen atmosphere of $1x10^{-5}$ torr from 27 °C to 97 °C with a ramping rate of 5 °C/min.

In the low mass regime (34~50 amu), $^{16}O^{18}O^+$ (mass= 34 amu), CO_2^+ (mass= 44 amu) are the two major peaks in the mass spectra. The $^{16}O^{18}O$ came from oxygen dosing, while CO_2^+ mainly came from the degasing of the sample/sample plate. The mass scan skipped the mass of $^{16}O_2$ due to its extremely high intensity.

For the middle mass regime (51~150 amu), fragments from the ligands started to appear in the mass spectra: the peak at mass= 51 amu is assigned to $C_4H_3^+$; the peak at mass = 77 amu is assigned to $C_6H_5^+$; the peak at mass = 91 amu is assigned to $PhCH_2^+$; the peaks at mass = 107, 108 amu correspond to $(PPh\text{-}H)^+$ and PPh^+, respectively. There are no observed peaks resulting from the pure aluminum cluster fragments (Al_2^+, mass= 54 amu; Al_3^+, mass= 81 amu).

In the high mass regime (150~200 amu), fragments seen are from $C_{12}H_8^+$ (mass=152 amu),$[P(Ph)_2\text{-}2H]^+$(mass=183 amu), $[P(Ph)_2\text{+}H]^+$ (mass=186 amu). The peak at mass=157 amu is unknown, but is also observed as a strong peak in $P(Ph)_3$ mass spectra so it is likely formed as a result of ligand fragmentation.[8]

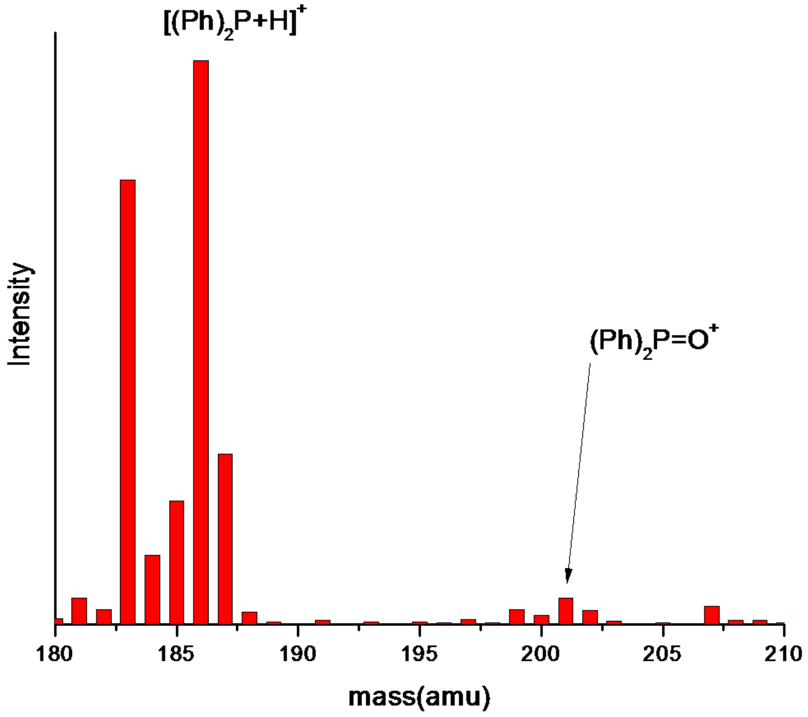

Figure 10.3 Mass scan of $Li_2Al_3(PPh_2)_6$ upon exposure to oxygen in the mass range of 180 amu to 210 amu.

From the mass spectral pattern distribution, it can be concluded that the vast majority of the products detected by our QMS are the fragments of ligands used in protecting the aluminum core. In addition, no aluminum-containing species were observed in the mass spectra. Most strikingly, most of the fragments detected by QMS do not contain oxygen. A separate check on mass=201 amu confirmed little presence of $O=P(Ph)_2$ presented upon oxygen exposure as shown in Figure 10.3. As the temperature increased initially, the intensity for all the fragments increased as well, probably due to the volatility of the $P(Ph)_2$ ligand which was employed in synthesizing the clusters. Further increase of the temperature resulted in decreased fragment peak intensity due to the consuming of the reactants. It should be noted in the control experiment no oxygen was dosed, the TPR spectra are mostly identical. This further confirmed that little oxidation of ligands took place during the reaction with oxygen.

B. Ex situ XPS on $Li_2Al_3(PPh_2)_6$ after Reaction

After the $Li_2Al_3(PPh_2)_6$ was reacted with oxygen, ex-situ XPS was used to identify the chemical compositions of the non-volatile products left on surface. Figure 10.4 shows the XPS spectra on the Al(2p) and P(2p) regions. The binding energy of Al(2p) is 75.8 eV, indicating that aluminum exists in a +3 oxidation state after the reaction, where the binding energy for P(2p) is shown to be 134.0 eV confirming the oxidation of phosphorus after exposed to oxygen. The ratio of aluminum to phosphorus was measured to be ~ 5.3: 1, which is much higher than the original ratio 1:2 in the unreacted sample. This indicates ~91% loss of the ligand during the reaction. The change of the Al to P ratio over the course of the reaction is consistent with our TPR results showing that the gaseous products desorbing during the reaction are mainly from the ligand.

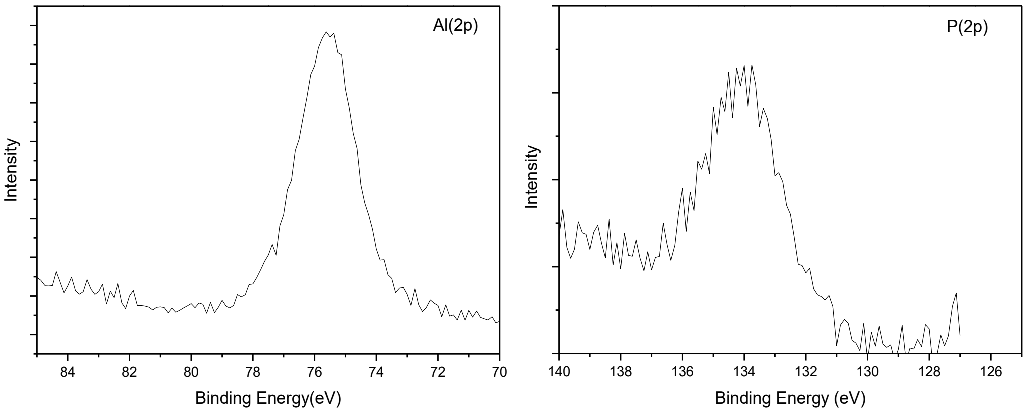

Figure 10.4 Ex-situ XPS spectra of $Li_2Al_3(PPh_2)_6$ after reacting with oxygen on the Al(2p) and P(2p) regions.

C. Discussion of Results

Previous calculations by Hooper along with the solution results presented by Merrill et al. predict that O_2 reacts preferentially with the aluminum atoms of reduced aluminum species rather than with their ligand layers. [5-6] This suggests that the combustion energy would not be wasted by burning the ligands. Our TPR and XPS experiments confirm Hooper's predictions by using the model molecular aluminum cluster $Li_2Al_3(PPh_2)_6$. The experimental results on $Li_2Al_3(PPh_2)_6$ are also consistent with our previous results on $[AlBrNEt_3]_4$.[9] During the TPR experiments on $Li_2Al_3(PPh_2)_6$, gaseous products analyzed by QMS demonstrate that none of the evolved ligand fragments show evidence of oxidation. Ex situ XPS results of the residual solid film shows aluminum was oxidized to a +3 oxidation states. The ratio of aluminum to phosphorus increased upon reaction with oxygen due to the loss of a phosphorus-containing ligand during the reaction. Thus, the reaction scheme can be concluded:

$$Li_2Al_3(PPh_2)_{6\,(s)} + O_{2(g)} \rightarrow Al_2O_{3(s)} + \text{non-oxidized volatile ligand fragments}_{(g)}$$

10.1.4 Conclusion

The reaction of the molecular aluminum clusters $Li_2Al_3(PPh_2)_6$ with oxygen was investigated by a combination of TPR and XPS. The experimental findings support the previous theory that O_2 reacts preferentially with the aluminum core of the cluster rather than with its ligand overcoat. This finding can be used as a guide for the design and application of ligated aluminum clusters.

Acknowledgement

This material is based in part on work supported by the DTRA under grant number, HDTRA11510031 (KHB).

10.2. $Al_4Cp^*_4$ toward Oxygen

The $Al_4Cp^*_4$ sample was synthesized by the Eichhorn Group. A home-made vacuum suitcase was employed to introduce the air-sensitive $Al_4Cp^*_4$ sample into UHV environment. The suitcase has a special differential-pumped-double-sealed design, which ensured an oxygen-free environment during the transfer process and also enables rotational/ translational motion of the sample in vacuum. A piece of fresh-cut sodium was added as a sacrificial oxygen trap during the transfer process. The $Al_4Cp^*_4$ powder was loaded onto a tantalum sample plate (affixed to the plate with carbon tape) in a glove box and subsequently transferred to a UHV set-up by the as-mentioned vacuum suitcase. Once the sample was in UHV environment, a TPR set-up implemented with a Hiden HAL/3F PIC quadruple mass spectrometer (QMS) was used to characterize the reactivity of the sample. The sample was heated up by a tungsten filament behind the sample and the temperature of the sample was monitored by a K-type thermocouple attached to the sample holder. A temperature ramping rate of 0.65 °C/s was adopted. The reaction products that desorbed from the surface were measured by QMS with a glass shroud in front of the ionizer. To characterize the reactivity of the $Al_4Cp^*_4$ with oxygen, 1×10^5 torr isotopically labelled oxygen ($^{18}O_2$) was dosed through a leak valve to react with $Al_4Cp^*_4$.

Figure 10.5 presents the TPR spectra of $Al_4Cp^*_4$ from 35 °C to 210 °C with a ramping rate of 0.65 °C/s. The major peaks of the desorption products are assigned by referring to a previous mass spectral study on pentamethylcyclopentadiene (Cp). The mass spectra displayed a parent peak of Cp at 136 amu , with the lower mass peaks corresponding to the major fragments of Cp and Cp^*, i.e. 121 amu, 105 amu, 93 amu, 79 amu. In addition to the fragments from Cp and Cp^*, a mass peak at 162 amu was detected as the sample temperature was raised. We assigned this peak to AlCp*, which was predicted as one of the major decomposition products of the aluminum–cyclopentadienyl clusters by previous calculations. The production of AlCp* is supportive of the bonding nature between Al atoms and Cp* ligands.

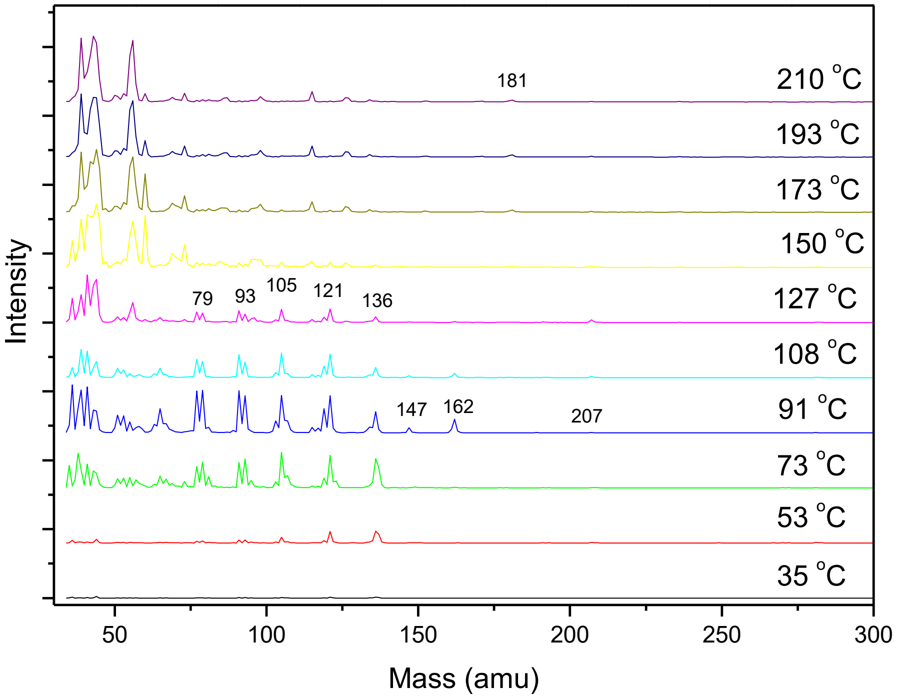

Figure 10.5 TPR spectra of $Al_4Cp^*_4$ from 35 °C to 210 °C with a ramping rate of 0.65 °C/s

Figure 10.6 presents the TPR spectra of $Al_4Cp^*_4$ generated upon exposure of the solid to $1x10^{-5}$ torr $^{18}O_2$ from 36 °C to 213 °C with a ramping rate of 0.65 °C/s. In addition to the fragments of Cp* and the AlCp* unit, a higher mass peak at 207 amu was also observed when the sample temperature increased. We attributed this peak at 207 amu to $Al_2{}^{18}OCp^*$, formed from the oxidation of $Al_4Cp^*_4$.

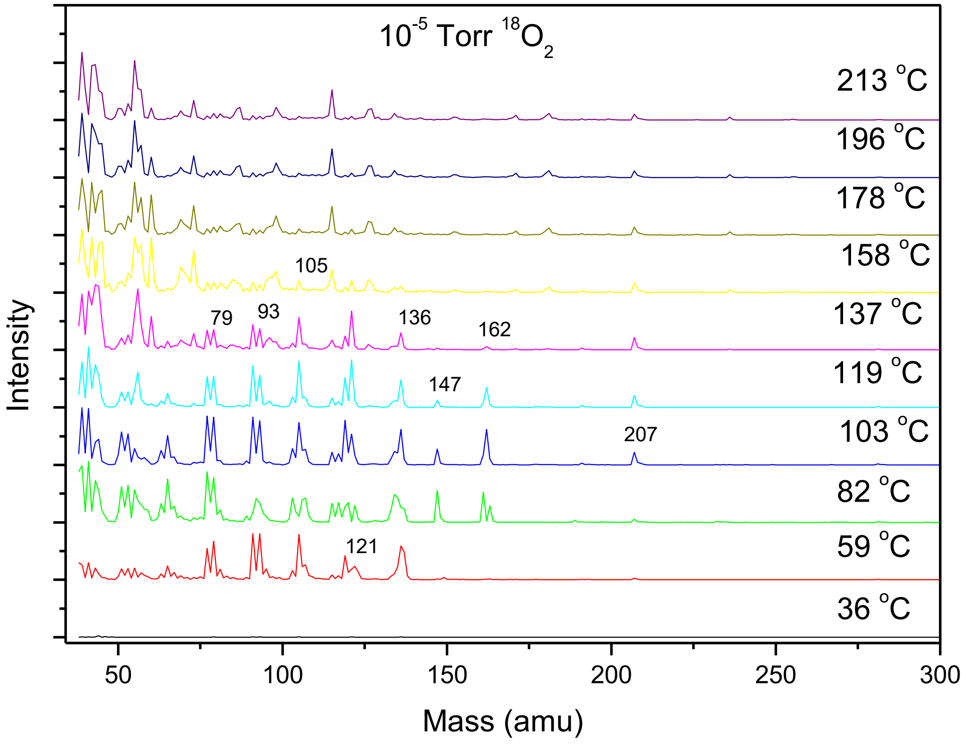

Figure 10.6 TPR spectra of $Al_4Cp^*_4$ in $1x10^{-5}$ torr $^{18}O_2$ from 35 °C to 210 °C with a ramping rate of 0.65 °C/s

Acknowledgement

This material is based in part on work supported by the AFOSR under grant number, FA9550-15-1-0259 (KHB).

10.3. $[AlBrNEt_3]_4$ toward Oxygen and Water

TPR experiments of crystalline yellow $[AlBrNEt_3]_4$ were first studied by heating the sample in vacuum from 25 to 110 °C with a ramp rate of 10 °C/min. Analysis of the evolved gases by mass spectroscopy (Hiden HAL/3F PIC quadruple mass spectrometer) shows that the tetramer begins to decompose at ~50°C to give NEt_3(101 amu), and its fragments (58, 86 amu) as the major products. A similar experiment was conducted in which crystalline $[AlBrNEt_3]_4$ was dosed with 1×10^{-5} Torr isotopically labeled $^{18}O_2$ gas while heating by the same schedule described above. The resulting gases (Figure 10.7, left) are virtually identical to the in-vacuo control TPR experiment showing only NEt_3 and its decomposition fragments. XPS analysis of the resulting white residue showed the presence of Br and Al (III), presumably Al_2O_3. The TPR of the tetramer was repeated a third time, dosing instead with 1.0 x 10^{-4} Torr D_2O prior to heating to investigate possible reactions induced by the presence of water in the droplets. The resultant spectra show that the major product is still the labile NEt_3 consistent with the previous two experiments(Figure 10.8, left)., but closer examination of 75-84 amu mass spectrum region reveals the production of $D^{79}Br$ and $D^{81}Br$ at ~50°C (Figure 10.8, right). The higher intensity of $D^{79}Br$ and $D^{81}Br$ from the D_2O exposed sample compared to the non-exposed sample indicates $[AlBrNEt_3]_4$ undergos a hydrolysis process to generate gaseous DBr.

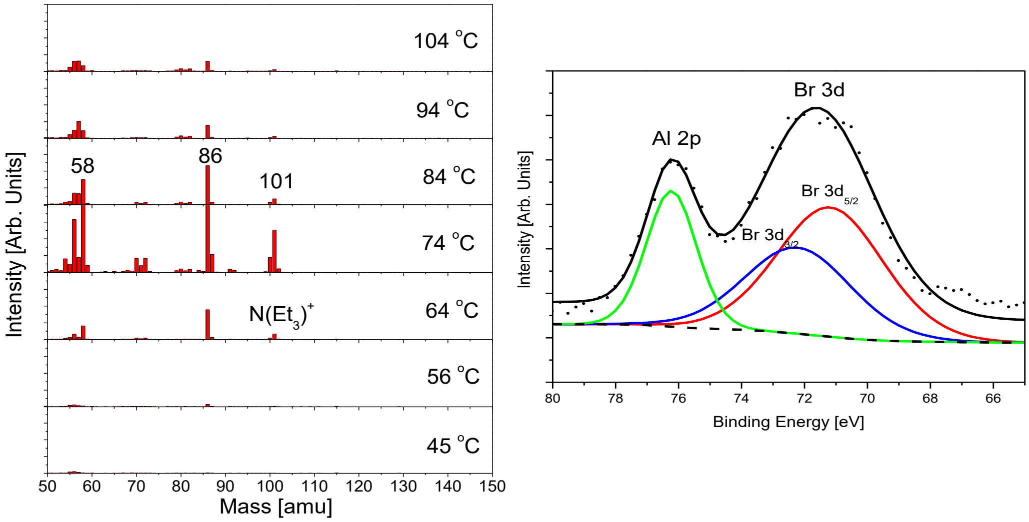

Figure 10.7: LEFT: TPR spectra of reaction of $[AlBrNEt_3]_4$ with $^{18}O_2$ @ 1 x 10^{-5} Torr. peaks match NEt_3 and its known fragmentation pattern (Note: The intensity of 58, 86 amu

at 74 °C are out of scale) **RIGHT:** XPS Spectra of sample after the reaction showing Al and Br remaining.

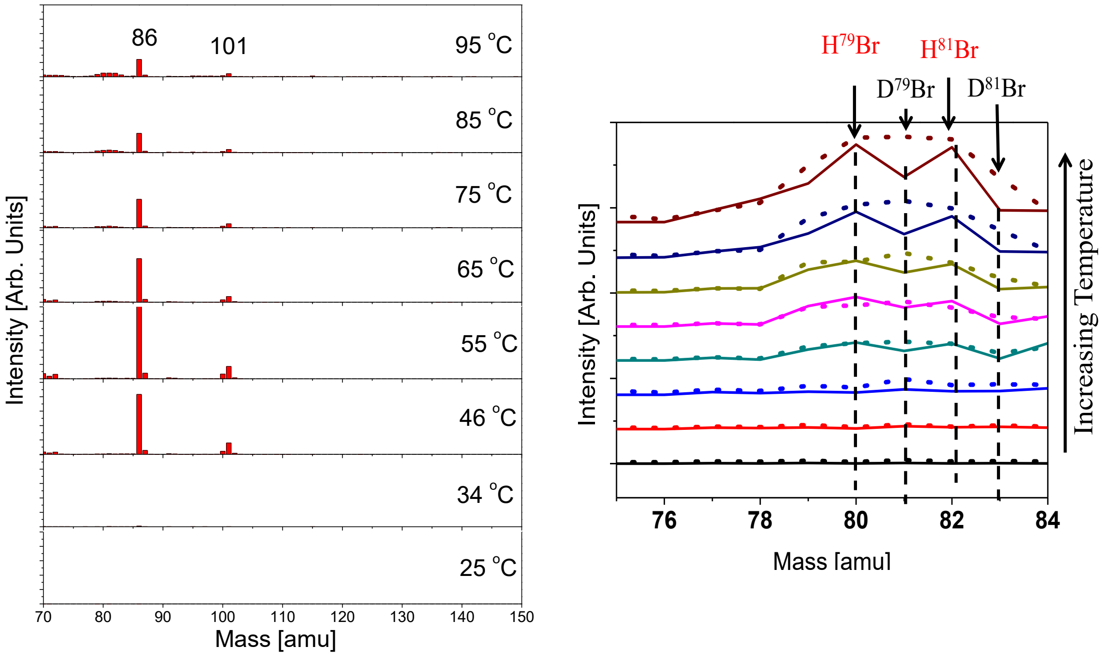

Figure 10.8 LEFT: Temperature Programmed Reaction Spectra of $[AlBrNEt_3]_4$ exposed to D_2O at 1.0 x 10^{-4} Torr for 1 hour. The chamber was the evacuated to 1 x 10^{-7} Torr and the TPR was subsequently taken. **RIGHT:** Comparison of TPR Spectra of $[AlBrNEt_3]_4$ exposed to D_2O (dotted line) and not exposed to D_2O (solid line)in the mass 75-84 amu region. This comparison demonstrates that exposure to D_2O does generate some $D^{79}Br$ and $D^{81}Br$

References

(1) R.J. Jouet, A.D. Warren, D.M. Rosenberg, V.J. Bellitto, K. Park, M.R. Zachariah, Chem. Mater. 2005, 17, 2987-96.

(2) S.W. Chung, E.A. Guliants, C.E. Bunker, D.W. Hammerstroem, Y. Deng, M.A. Burgers, P.A. Jelliss, S.W. Buckner, Langmuir 2009,25, 8883-87.

(3) M.J. Meziani, C.E. Bunker, F. Lu, H. Li, W. Wang, E.A. Guliants, R.A. Quinn, Y.-P. Sun, ACS Appl. Mater. Interfaces 2009,1, 703-09.

(4) J. Vollet, J.R. Hartig, H. Schnockel, Angew. Chem. Int. Ed. 2004, 43,3186-89.

(5) K.S. Williams, J.P. Hooper, J. Phys. Chem. A 2011,115 ,14100-09.

(6) H. Zhu, J. Chai, V. Jancik, H.W. Roesky, W.A. Merrill, P.P. Power, J. Am. Chem. Soc. 2005, 127,10170-71.

(7) D.H. Mayo: Synthesis and Characterization of Low-Valent Aluminum and Gallium Compounds from Aluminum (I) and Gallium (I) Precursors, University of Maryland (College Park, Md.), 2011.

(8) D.H. Williams, R.S. Ward, R.G. Cooks, J. Am. Chem. Soc. 1968, 90,966-72.

(9) P. M. Guerieri, S. DeCarlo, B. Eichhorn, T Connell, R. A. Yetter, X. Tang, Z. Hicks, K. H. Bowen, and M. R. Zachariah, J. Phys. Chem. A, 2015,119,11084–11093

Appendix A

The coupling reactions of small organic molecules on metal surfaced have been extensively studied, and one of them is Ullmann reaction, which is the coupling reaction between two aryl halides catalyzed by copper. For example, as shown by Gellman[1], the reaction between iodobenzene on the Cu(111) surface leads to the coupling products as bi-phenyl, evident by the results from temperature programmed desorption. Further high resolution STM results[2] from Sykes Group suggested that, Ullmann coupling of bromobenzene proceeded via a Ph-Cu-Ph intermediates on Cu(111) surface. This interesting finding brought in several new aspects of this classical system: Is this catalytic process a single-atom catalyzed process? Is there any size dependency? Is this ligated single atom complex a universal intermediate for many metal organic reactions? Motivated by this, we started to look into this system by studying the Ullmann reaction on mass-selected copper clusters. Initially Cu_{100} clusters were deposited onto HOPG surface and bromobenzene was dosed via a leak valve onto the surface, as a proof of principles. The coupling product biphenyl was observed by TPD. Two desorption peaks for biphenyl were

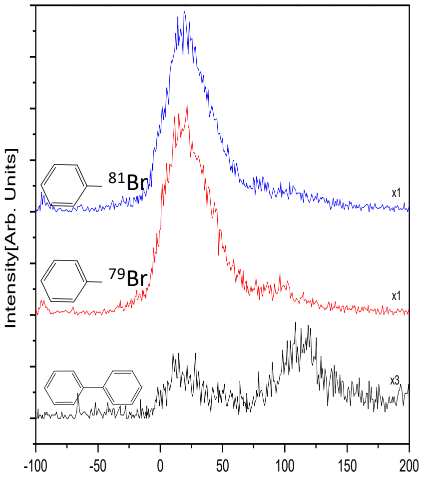

Figure A.1 TPD of Bromobenzene on Cu_{100}

seen in Figure 11.1. It is likely there are two possible mechanisms involved. Previous studies that high temperature desorption peak is due to the migration of the phenyl group, while the low temperature desorption peak has to do with the reaction between two adjacent phenyl groups .[3] It should also be noted that the low temperature desorption peak of biphenyl is at a similar position as that from bromobenze. Although the clusters studied are relatively large, they are still active toward Ullmann reaction. It will be of most interest to look at the Cu_n with size n<10.

References

(1) Meyers, J. M.; Gellman, A. J. Surface Science 1995, 337, 40.

(2) Lewis, E. A.; Murphy, C. J.; Liriano, M. L.; Sykes, E. C. H. Chemical Communications 2014, 50, 1006.

(3) Xi, M.; Bent, B. E. J Am Chem Soc 1993, 115, 7426.

CIRRICULUM VITA

Xin Tang

Nov 2016

EDUCATION

- Doctor of Philosophy in Chemistry, Johns Hopkins University, Baltimore, Oct 2016 (expected)
- Bachelor of Science in Material Chemistry, Peking University, Beijing, July 2009
- Visiting Student in Prof. Ueli Heiz's Group, Visiting Student in Prof. Ueli Heiz's Group, July 2012 - Aug. 2012

RESEARCH EXPERIENCE

- Research Assistant – Kit H. Bowen Group, Department of Chemistry, Johns Hopkins University 2010 - Present
  - Surface studies of soft-landed mass-selected metal/ metal oxide cluster catalysts by TPD/XPS
  - Gas phase photoelectron spectroscopy of small organic anions
  - STM studies of assembling behaviors of mass selected lead sulfides based quantum dot clusters
  - Surface morphologies of ligand-free mass selected metal and metal oxide clusters studied by AFM and STM

  - Catalytic decomposition of chemical warfare agent Simulants by clusters catalysts

- Research Associate – Prof. Hongfei Wang and Yuan Guo’s Group, ICCAS, China 2009 –2010
  - Design of a thin layer flow injected spectroelectrochemical cells
  - Sum frequency vibrational spectroscopy of acetonitriles at electrochemical interfaces
- Research Assistant in Prof. Kai Wu’s Group, Peking University, China 2006 – 2009
  - Epitaxial growth of gold thin films on mica substrate
  - Fabrication of titania-based functional nano-materials and their application in dye-sensitized solar cells

TEACHING EXPERIENCE

- Teaching Assistant, Johns Hopkins University, MD, United States 2010 - 2012
  - *General Chemistry*
  - *Physical Chemistry Lab* (Organized a lab including AFM/STM/SEM for undergraduate Students)
  - *Experimental Methods in Physical Chemistry* (Teach Solidworks for JHU Graduate Students)

PUBLICATIONS

1. P. M. Guerieri, S. DeCarlo, B. W. Eichhorn, T. Connell, R.A. Yetter, **X. Tang**, Z. Hicks, K. H. Bowen, Jr., and M. R. Zachariah, Molecular Aluminum Additive for Burn Enhancement of Hydrocarbon Fuels, *J. Phys. Chem. A,* **,119**, 11084−11093 (2015).

2. A. Dollinger, C. H. Strobel, H. Bleuel, A. Marsteller, G. Gantefoer, D. H. Fairbrother, **X. Tang,** K. H. Bowen and Y. D. Kim, Growth Modes of Thin Films of Ligand-free Metal Clusters, *J Appl Phys* **117**, 195302 (2015).
3. **X. Tang**, D. Bumueller, A. Lim, J. Schneider, U. Heiz, G. Ganteför, D. H. Fairbrother, and K. H. Bowen, Catalytic Dehydration of 2-Propanol by Size-Selected $(WO_3)_n$ and $(MoO_3)_n$ Metal Oxide Clusters, *J. Phys. Chem. C*, 118, 29278–29286(2014)
4. X. Li, K. Wepasnick, **X. Tang**, D. H. Fairbrother, K. H. Bowen, A. Dollinger, C. H. Strobel, J. Huber, T. Mangler, Y. Luo, S. Proch and G. Gantefoer, A New Nano Material Synthesized from Size-selected, Ligand-free Metal Clusters, *J. Appl. Phys.* , 115, 104304 (2014)
5. **X. Tang**, J. Schneider, A. Dollinger, Y. Luo, A. S. Wörz, K. Judai, S. Abbet, Y. D. Kim, G. F. Ganteför, D. H. Fairbrother, U. Heiz, K. H. Bowen and S. Proch , Very Small “Window of Opportunity” for Generating CO Oxidation-active Au_n on TiO_2 , *Phys. Chem. Chem. Phys.* , 16, 6735-6742 (2014)
6. X. Zhang, **X. Tang**, D. H. Mayo, S. DeCarlo, B. Eichhorn, K. H. Bowen, Photoelectron Spectroscopic Study of the Diphenylphosphide Anion and Its Oxide, *Chem. Phys. Lett.* ,597, 110 −113 (2014)
7. F. Calvo , K. H. Bowen, and **X. Tang**, Modeling the Aggregation of MgO Clusters on Highly Oriented Graphite , *J. Phys. Chem. C* 118, 1306 (2014)
8. X. Zhang, **X. Tang**, K.H. Bowen, Photoelectron Spectroscopic Study of the Ethyl Cyanoacrylate Anion, *Chem. Phys. Lett.* 582, 21(2013)
9. **X. Tang**, X. Li, Y. Wang, K. Wepasnick, A. Lim, D. H. Fairbrother, K. H. Bowen, T. Mangler, S. Noessner, C. Wolke, M. Grossmann, A. Koop, G. Gantefoer, B. Kiran and A. K. Kandalam , Size Selected Clusters on Surfaces , *J. Phys.: Conf. Ser.* , 438 0120 (2013)

10. X. Li, K.A. Wepasnick, **X. Tang**,Y. Wang, K.H. Bowen, D.H. Fairbrother,and G. Gantefoer, Ion Induced Modification of Size-selected MoO_3 and WO_3 Clusters Deposited on HOPG, *J. Vac. Sci. Technol.* B, 30, 031806 (2012)
11. B. Kiran, A.K. Kandalam, R. Rallabandi, P. Koirala, X. Li, **X. Tang**, Y. Wang, H. Fairbrother, G. Gantefoer, and K.H. Bowen, $(PbS)_{32}$: A Baby Crystal, *J. Chem. Phys.,* 136, 024317 (2012)
12. J. Yu, D. Wang, Y. Huang, X. Fan, **X. Tang**, C. Gao, J. Li, D. Zou, and K. Wu, A Cylindrical Core-shell-like TiO_2 Nanotube Array Anode for Flexible Fiber-type Dye-sensitized Solar Cells, *Nanoscale Research Letters,* 6, 94 (2011).
13. Z. Huang, **X. Tang**, G. Deng, E. Zhou, H. Wang, Y. Guo, The Flip-Flop Behavior of Acetonitrile at Au Electrode Surface Investigated by Sum Frequency Generation Vibrational Spectroscopy, *Chinese Journal of Electrochemistry*, 17, 134 -138 (2011)
14. X. Jin, Z. Li, **X. Tang**, B. Yan, New Ideas on Hypervalent Compound and Octet Rules, *University Chemistry*, 22, 61-68(2007)

PRESENTATIONS

1. The 75th Physical Electronics Conference, New Brunswick, NJ, June 18, 2015
2. AVS 61st International Symposium, Baltimore, MD. Nov. 10, 2014
3. Cluster Surface Interaction (CSI) Symposium, Lyon, France, Sep. 11, 2012
4. ACS Colloids and Surfaces 2012 Symposium, Baltimore, MD, June 11, 2012

PROFESSIONAL HONORS, AWARDS, AND SOCIETIES

- Sarah and Adolph Roseman Achievement Award, Johns Hopkins University,2016

- Physical Electronics Conference 2015 Nottingham Prize Finalist, 2015
- Alexander Kossiakoff Fellowship, Johns Hopkins University,2014
- The first prize (Rank 1st) in the Chemistry Olympiad Competition of Jiangsu province, 2004